

Radiation Hard Environmental Monitoring Sensors Inside the PANDA Calorimeter

Bachelor thesis
by Yannik Bettner
Submission date: 30.09.2019

Justus Liebig University Giessen
II. Institute of Physics

First reviser: Prof. Dr. Kai-Thomas Brinkmann
Second reviser: PD Dr. Sören Lange AR
Technical supervisor: Dr. Markus Moritz and Dr. Hans-Georg Zaunick AR

Abstract

In the scope of this thesis, environmental sensors (SHT21 and BME280) were investigated concerning their radiation hardness. These are to be used in the PANDA electromagnetic calorimeter at the future FAIR facility at the GSI in Darmstadt to monitor the front-end electronics to avoid water or even ice formation.

Three of each sensor type were irradiated with gamma-rays up to an accumulated dose of 2000 Gy. They were tested in a climate test chamber under different temperature and humidity conditions before and after irradiation. As a reference sensor, an additional, non-irradiated sensor of each type was placed inside the climate chamber.

In order to decide at which temperatures or humidities the sensors show a change by irradiation, it was checked initially how well the set values were achieved and how reproducible they are.

The temperature was achieved in a good approximation and is reproducible, whereas the relative humidity does not show such a good behavior. However, within the accuracies of the sensors with respect to the relative humidity, the absolute difference is small enough to evaluate this range.

During these measurements, it was observed that one BME280 has failed completely and outages with respect to pressure- and humidity measurements were observed in relation to the other BME280 at a temperature of 0 °C.

Only from an accumulated dose of 500 Gy and above, the SHT21 shows a reaction to irradiation with respect to its temperature measurement. With regard to the measurement of relative humidity, this value is 2000 Gy. The BME280 shows a slightly worse behavior as the SHT21 in relation to the temperature, whereas for the relative humidity, it shows no detectable reaction even after an accumulated dose of 2000 Gy.

The dose at which the sensors show a significant deviation is far below the dose they would get within a lifetime in PANDA. Thus, it is necessary to investigate the radiation hardness of the sensors further, also with respect to charged particles.

Contents

1	Introduction	2
2	The PANDA Experiment	3
2.1	Electromagnetic Calorimeter	5
2.1.1	Sensors	8
3	Radiation	9
3.1	Interaction of Radiation with Matter	9
3.2	Radiation Damage	10
3.3	Thermal Annealing	12
4	Environmental Sensors	13
4.0.1	Temperature	13
4.0.2	Pressure	14
4.0.3	Relative Humidity	15
4.1	I ² C - Interface	15
5	Setup and Procedure	17
5.1	Carrier Board	17
5.2	Climate Test Chamber	21
5.3	Procedure	22
5.4	Irradiation	24
6	Analysis	26
6.1	Temperature Measurement Verification	26
6.2	Repeatability Tests	33
6.3	Outages of the BME280	40
6.4	Radiation Hardness	42
6.4.1	Temperature - Radiation Hardness	43
6.4.2	Relative Humidity - Radiation Hardness	48
7	Conclusion and Outlook	54
8	Appendix	56

1. Introduction

Even ancient Greek philosophers such as Democritus (400 B.C.) were already looking for the structure of matter from the smallest particles. He assumed that matter consists of the smallest indivisible (ancient Greek: *átomos*) building blocks.

At the end of the 19th century it was discovered that the atom consists of even smaller components, the atomic nucleus and the atomic shell. But even these are more divisible. In the course of time it was possible to gain an ever deeper insight into the atom and its smallest particles.

In order to obtain new scientific insights in particle physics, higher energies and higher precision are inevitable to look increasingly deeper into the matter, to understand the strong interaction and what matter consists of for example. Therefore fixed target or collider experiments are utilized in which a lot of particles are produced. A lot of electronics is used for the reconstruction of those particles, which is exposed to radiation with high energy. Part of the electronics are environmental sensors for environmental monitoring to obtain stable operating conditions. The radiation tolerance of the chosen sensors have been investigated within this Bachelor thesis.

A short overview over the PANDA (AntiProton ANnihilation at DArmstadt) physics is given at the beginning followed by some basics about the measurement of non-electric physical quantities, like temperature, moisture and pressure. Since gamma-rays were used for the investigation of the radiation hardness, the main interactions of gamma-rays with matter are explained. Afterwards, the measuring procedure will be explained and the results of this thesis will be presented. The thesis is concluded by a summary with respect to the suitability of the sensors for the planned project.

2. The $\bar{\text{P}}\text{ANDA}$ Experiment

The $\bar{\text{P}}\text{ANDA}$ experiment is one of the key experiments at the future FAIR facility (Facility for Antiproton and Ion Research), which is currently under construction at the area of the GSI Helmholtzzentrum für Schwerionenforschung in Darmstadt. An overview of FAIR is given in figure 2.1.

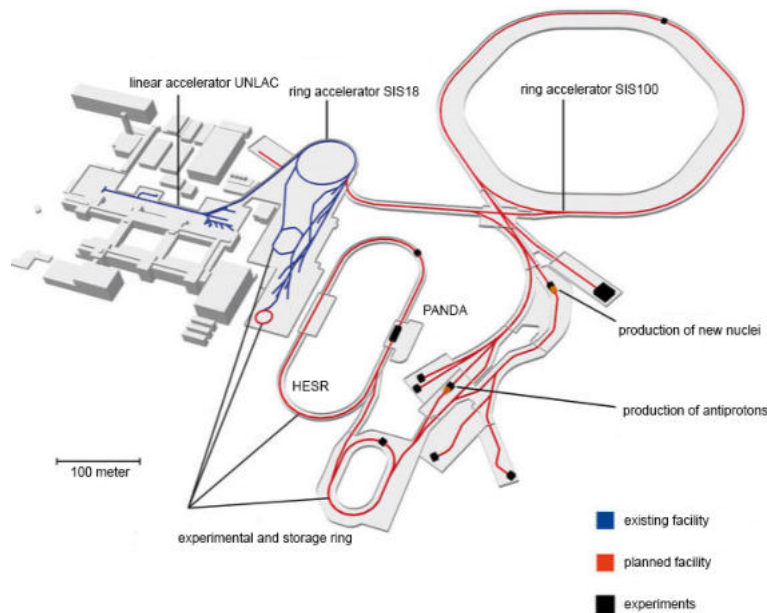


Figure 2.1: Overview of FAIR - The existing parts are highlighted in blue and the planned in red.

Various research areas are covered. These include atomic and plasma physics (APPA), nuclear matter and astrophysics (NUSTAR), compressed baryonic matter (CBM) and physics with high-energetic antiprotons ($\bar{\text{P}}\text{ANDA}$). The already existing accelerators, the **UN**iversal **L**inear **AC**celerator (UNILAC) and the **S**chwer**I**onen**S**ynchrotron (SIS18) will be used as pre-accelerators for the ring SIS100. Additionally, there are three storage rings. One is the **H**igh **E**nergy **S**torage **R**ing (HESR). The HESR-synchrotron has a racetrack geometry, where $\bar{\text{P}}\text{ANDA}$ will be located at one of the two straight sections. Antiprotons in the momentum range from $1.5 \text{ GeV } c_0^{-1}$ up to $15 \text{ GeV } c_0^{-1}$ can be injected for the experiments. The $p\bar{p}$ -collision rate is up to 20 million at a target luminosity of $2 \times 10^{32} \text{ cm}^{-2} \text{ s}^{-1}$. The antiprotons are produced off a primary proton beam and filled into the HESR, where they collide with a fixed proton- or a nucleus target inside the $\bar{\text{P}}\text{ANDA}$ detector. The aim of the $\bar{\text{P}}\text{ANDA}$ experiment is to obtain new insights into the **Q**uantum **C**hromo**D**ynamics (QCD). These include the following

topics:

- **Hadron spectroscopy:** Search for exotic particles and precise identification of different hadrons. This includes the investigation of gluonic excitations, charmonium-, D-Meson- and Baryon spectroscopy.
- **Hadrons in matter:** Study the change of properties of hadrons when they are surrounded by hadronic matter. This aims to understand the origin of hadron mass in context of the spontaneous chiral symmetry breaking and its partial reconstruction in a hadronic environment.
- **Hypernuclei:** It is possible to replace an up or a down quark with a strange or heavier quark in a nucleus, which leads to a hypernucleus. Hypernuclei are an excellent tool to study nuclear structure.
- **Nucleon structure:** Especially generalized parton distributions and time-life form factors can be investigated.

To access these information, the experiment requires a versatile detector. The detector is capable of precise reconstruction of particle tracks, vertex determination, momentum and energy measurements and particle identification. Furthermore, it has a full solid angle coverage.

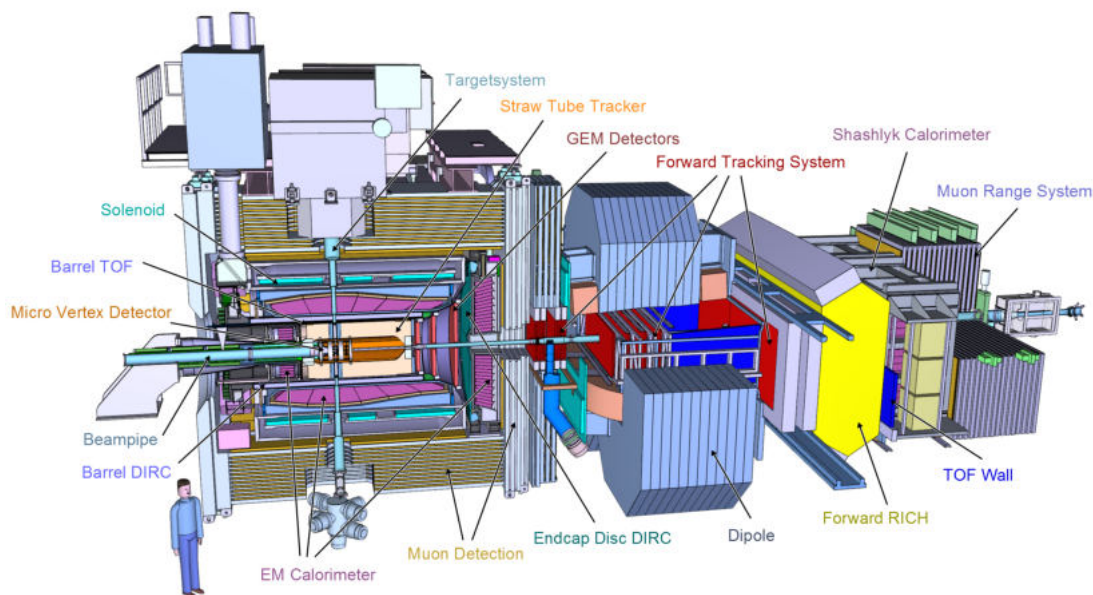


Figure 2.2: Overview of the PANDA detector.

The detector is divided into the target spectrometer (TS) and the forward spectrometer (FS). This is necessary since most of the produced particles will move in beam direction. The target spectrometer is placed around the interaction region and is designed as a shell-shaped structure to cover a major range of solid angle. The forward spectrometer will analyze the forward-going particles which cannot be detected with the target spectrometer. The structure of the whole detector is shown in figure 2.2.

The inner most **Micro Vertex Detector (MVD)** is placed in the TS around the interaction vertex and is followed by the **Straw Tube Tracker (STT)**. The MVD is able

to detect charged particles. Particularly it is utilized to identify particles with a very short lifetime which only can be identified by its decay products. The STT detects the trajectory of longer-lived charged particles. Then, the forward GEM detector is placed, which acts as a forward tracking detector for particles which are emitted below the angle of 22° . The next layer consists of the **D**etection of **I**nternally **R**elected **C**herenkov light (DIRC), the main task is to identify charged particles and to separate pions from kaons. It is followed by the **E**lectro**M**agnetic **C**alorimeter (EMC) which will be explained in more detail in section 2.1. At the end of the TS, there is a magnet system and a muon detector. The magnetic field creates bended tracks of charged particles to determine with the tracking system their momentum. In the FS the detectors are situated in beam direction. At first there is a drift chamber, which can be used for the reconstruction of trajectories. It is followed by **R**ing **I**maging **C**herenkov detector (RICH) and a shashlyk calorimeter. The next detector is a **T**ime-**O**f-**F**light detector. It is used for particle identification. As the target spectrometer, the FS concludes with a magnet system and a muon detector.

2.1 Electromagnetic Calorimeter

The electromagnetic calorimeter will be utilized the purpose of determining the energy for particles, which interact via the electromagnetic interaction. These include in particular electrons, positrons and photons. These particles produce electromagnetic showers by interaction with the crystal. Thereby electrons and positrons generate a photon by bremsstrahlung which is able to produce a new electron-positron pair. If the energy of the electrons and positrons rolls over the critical energy¹, the process of ionization dominates and no more high-energy photons are produced.

The direction of motion and the energy of the incoming particle can be reconstructed from the position of the crystal and the energy, which is deposited by the shower. Moreover, it is possible to distinguish between photons and electrons or positrons because photons are not detected in the MVD or STT. Hadrons also deposit energy in the calorimeter and can be distinguished from each other by the ratio of the momentum, which was detected in the tracker and the deposited energy in the calorimeter. The reason for this is that hadrons do not deposit all their energy in the EMC.

In general, the EMC is composed of three parts, the barrel, the forward- and the backward endcap. A cylindrical design is planned, so that almost the entire solid angle is covered. It is a homogeneous calorimeter with 15744 crystals of lead tungstate **PbWO₄**, which has a high density and a good energy resolution. The barrel (11360 crystals) and the backward endcap (524 crystals) will be read out by two avalanche photodiodes (APDs) per crystal. The EMC without the backward endcap can be seen in figure 2.3.

¹The critical energy is the energy at which energy loss due to ionization and bremsstrahlung are equal. Beyond the critical energy, bremsstrahlung dominates.

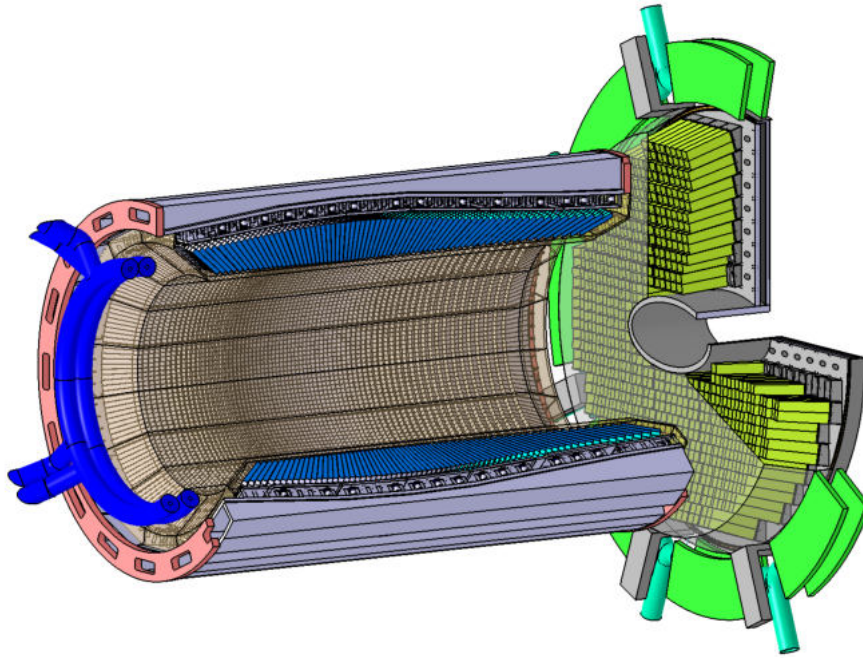


Figure 2.3: Schematic of the EMC without the backward endcap.

The innermost part (768 crystals) of the forward endcap will be read out with vacuum phototetrode from Hamamatsu.

The barrel EMC consists of 16 slices with 710 crystals each. Its structure can be seen in figure 2.4.

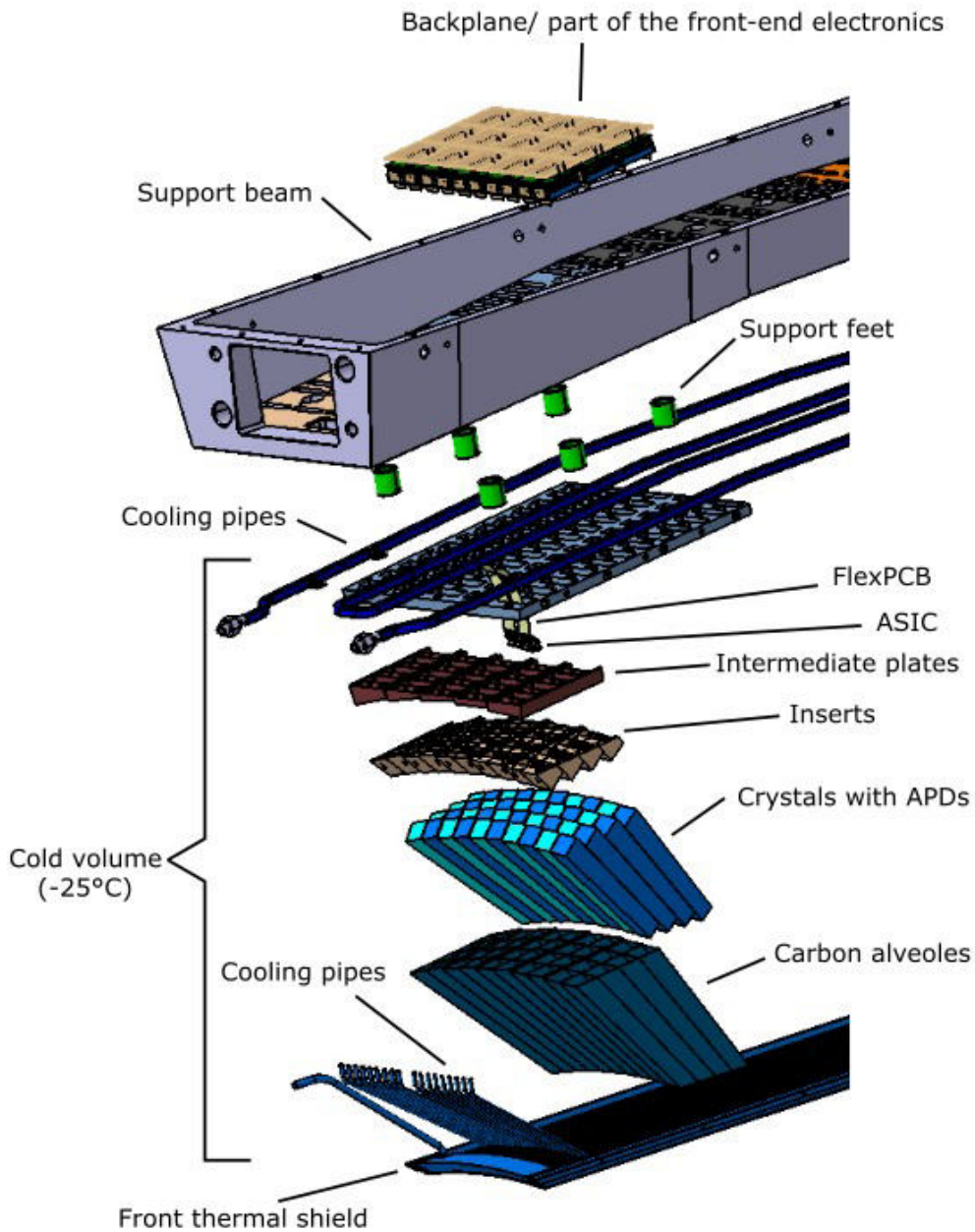


Figure 2.4: Exploded drawing of one barrel EMC slice.

The support beam is screwed to the super module back plate. In between there is a thermal insulation (which is not shown). The underside of the super module back plate is connected to the intermediate plates. The inserts, which are glued into the alveolus, are attached to it. In each alveole is one crystal. The operation temperature of the crystals will be -25°C . Thus, the light yield increases about a factor of almost four compared to room temperature and therefore the energy resolution especially for low energies.

The backplanes, part of the front-end electronics, which are necessary for operating and

adjustment of the detectors, are placed in the support beam. This adjoins to the cold volume -25°C , thus it is necessary to monitor this area with respect to temperature, relative humidity and pressure sensors. Since the sensors are exposed to radiation from the experiment, they have to be investigated for their radiation tolerance. For this, the sensors have been irradiated with a ^{60}Co -source.

2.1.1 Sensors

The SHT21 (Sensirion) consists of a band-gap temperature sensor and a capacitive humidity sensor element for the measurement of the relative humidity. Both sensors are seamlessly coupled to a 14-bit analog-to-digital converter (ADC) that can transmit digital data over the I²C protocol to a microcontroller or a processor respectively. These are located together with the ADC on a single CMOS silicon chip. CMOS (Complementary-symmetry **M**etal-**O**xide-**S**emiconductor) uses complementary and symmetrical pairs of p-type and n-type MOSFETs (**M**etal-**O**xide-**S**emiconductor **F**ield-**E**ffect **T**ransistor) for logic functions. Detailed information about the MOSFET can be found in section 3.2. The BME280 (Bosch Sensortec) is used in many mobile applications. In addition to the temperature and humidity measurement, it is equipped with an absolute barometric pressure sensor. However, the functionality of the sensor is not known, due to business secret.

The specifications of the sensors can be seen in table 2.1.

	SHT21	BME280
temperature range [$^{\circ}\text{C}$]	[-40; +125]	[-40; +85]
relative humidity range [%]	[0; 100]	[0; 100]
pressure range [hPa]	-	[0; 20000]
temperature resolution [$^{\circ}\text{C}$]	0.01	0.01
relative humidity - abs. resolution [%]	0.04	0.008
pressure - resolution [hPa]	-	0.18

Table 2.1: Specifications of the SHT21 and the BME280 [1][2].

Detailed information can be found in the datasheet [1][2].

3. Radiation

3.1 Interaction of Radiation with Matter

Every type of high-energy radiation, e.g. neutrons, electrons, protons, ions and gamma quanta interacts with matter. Depending on the particles, different interactions with matter can be observed.

Heavy (compared to the electron mass m_e), charged particles lose energy by travelling through matter due to inelastic scattering with electrons. The transmitted energy results in excitation and ionization of the atoms. The energy loss depends on the velocity of the travelling particles and the target material (proton number) itself.

It can be described with the Bethe-Bloch formula which consists of five different terms of energy loss:

- Collisions with electrons
- Bremsstrahlung
- Cherenkov radiation
- Elastic scattering on nuclei
- Nuclear reactions

Photons interact mainly via three different effects:

- Photoelectric effect: In the photoelectric process, the photon transfers its complete energy to a shell electron. This is used to release the electron which leads to an ionized atom. The energy excess is transferred to the electron in form of kinetic energy.
- Compton scattering: The Compton scattering describes a quasi-elastic impact of a photon with a shell electron. The photon is scattered off the electron and transfers part of its energy, which lies between zero and a maximum value, thereby increasing its wavelength. The maximum energy transfer is also known as the Compton-edge. The electron absorbs the transmitted energy and the atom is ionized by the removal of the electron.
- Pair production: If the energy of the photon is greater than twice the rest mass of an electron ($\approx 1 \text{ MeV}$), pair production becomes possible in the Coulomb field of atomic nucleus. The energy of the photon transferred almost completely into the masses of the resulting particles (electron and positron) and their kinetic energy. Additionally, the atomic nucleus serves as a recoil partner.

The released electrons which were mentioned in the previously described effects can undergo bremsstrahlung or ionization. Bremsstrahlung is an electromagnetic radiation caused by the deceleration of charged particles in an electric field. The absorption coefficients for the mentioned effects of the gamma radiation are shown in figure 3.1.

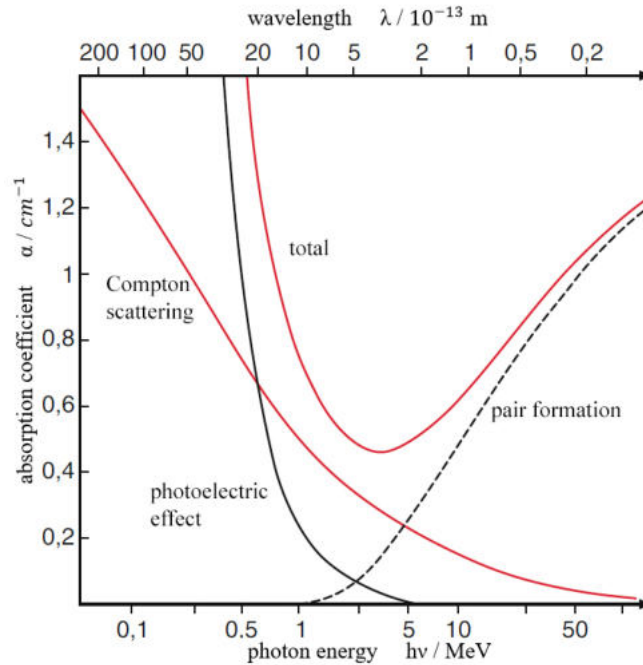


Figure 3.1: Contribution of photoelectric effect, Compton scattering and pair production of the interaction of gammas with matter (The absorption coefficient refers to lead as a function of the photon energy.) [3].

3.2 Radiation Damage

With respect to radiation damage, a distinction must be made between **ionizing** and **non-ionizing radiation**.

Non-ionizing radiation mainly causes substrate damages which means lattice defects. The incoming particles transfer their energy and momentum to the atoms, thus single atoms can be knocked-out of the lattice. An atom knocked out of its lattice site is called **Primary Knocked-on Atom (PKA)**. Thus an interruption of regular pattern (point defect) results where the knocked-out atom is placed in the lattice. Furthermore, an interstitial atom may be generated. If further dislocations occur, it is named a cluster defect.

For example these defects create new levels of energy in the band-gap of a solid-state. Three resulting effects can be observed in this respect:

- Change in effective doping concentration
- Increase of the dark current
- Increase of trapping centers

Gamma quanta can only damage the lattice to a limited extent. In general, they only produce point defects and not cluster defects such as hadrons. Gamma rays belong to

ionizing radiation and are able to damage amorphous oxides. The reason for this is that it does not have a distant configuration, thus displacement is easier.

This is especially important for the SHT21 which is based on a CMOS chip. A CMOS uses complementary pairs of p-type and n-type MOSFETs. MOSFETs are voltage regulated resistors and have three different connections, Gate, Source and Drain. The schematic of a typical n-type MOSFET can be seen in figure 3.2.

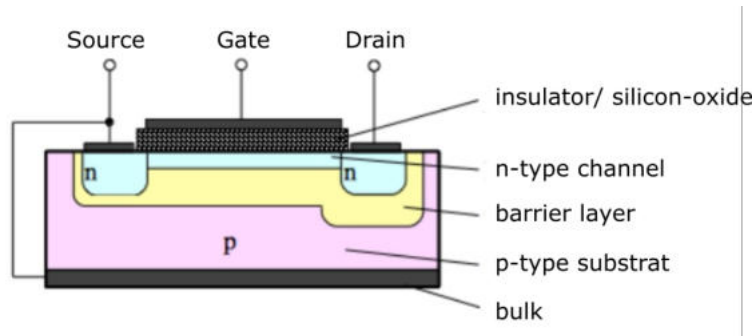


Figure 3.2: Structure of a MOSFET [4].

Gamma quanta create defects in a MOSFET by creation of electron-hole pairs in the oxide layer (3.3 B). The electrons can drift out of the oxide (3.3 C). The remaining holes, the so-called "fixed oxide charges", are accumulating at the silicon-substrate. Due to this, the oxide charges up positively and builds a barrier layer (3.3 D). This blocks the electrical current, thus the gate-voltage has to be readjusted.

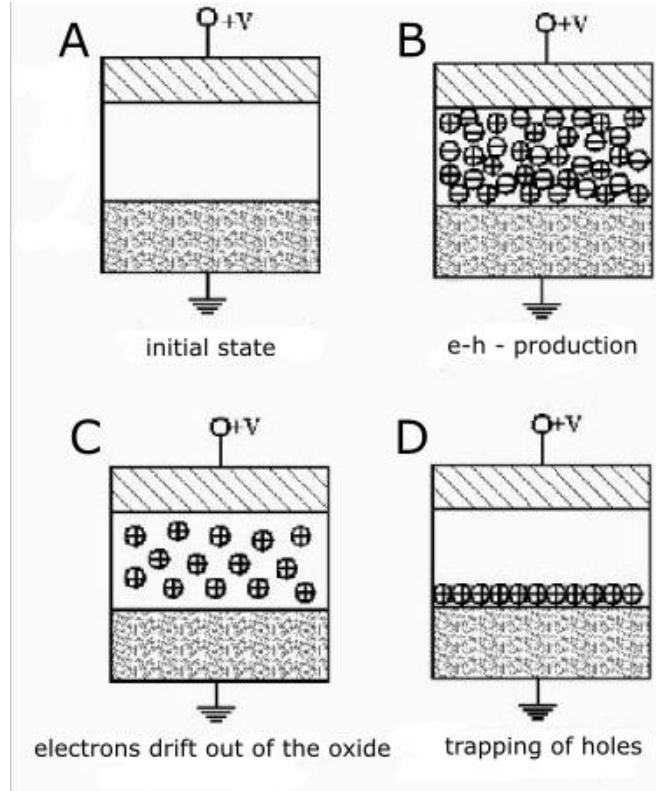


Figure 3.3: Formation of fixed oxide charges [5].

The required voltage for readjustment is given by the formula of the Flat Band Voltage.

$$V_{FB} = \Phi_{MS} - \frac{Q}{C} - \frac{1}{\epsilon} \int_0^d \rho(x) x dx \quad (3.1)$$

With: Φ_{MS} - contact potential difference in MOS structure, Q - electric charge at the interface, C - capacitance of the oxide, ϵ - vacuum permittivity, d - oxide thickness, $\rho(x)$ - charge density at the interface.

The formula indicates that higher voltages are required for greater charging of the oxide. Furthermore, it has to be noted that fixed oxide charges can cause parasitic currents between the electronic components.

3.3 Thermal Annealing

With respect to a damaged semiconductor, it can be observed that the damage decreases with time. This process is linked to the temperature. It is caused by the disappearance of the defects in the crystal. In general, a distinction between beneficial annealing, reverse annealing and not incurable defects can be made. Beneficial annealing describes a decrease of doping change within a few weeks (at room temperature). It can be explained as the recombination between the point defects and the free lattice atoms. It is assumed that the point defects decay with their own characteristic times. During the measurement of the effective doping as a function of time, it was observed that after the decrease of doping change it up again. This counteracts beneficial annealing and the annealing in general. It can be explained as the recombination between free lattice atoms, which form a bond among themselves. This effect is called "reverse annealing". It can only be observed after a few months at room temperature. To accelerate this procedure, temperature can be increased.

4. Environmental Sensors

In order to measure non-electrical quantities, these must be converted into an electrical signal. An amplifier stage follows the sensor which enhances the signal and allows a calibration and the determination of the sensitivity. As a last stage a digitization unit is needed, which registers the signal.

The SHT21 is equipped with a band-gap temperature- and a capacitive moisture sensor. How the measurement of temperature, moisture and pressure of the BME280 actually work is undisclosed by the manufacturer.

In the following, it will be described how temperature, relative humidity and pressure can be measured in general.

4.0.1 Temperature

One of the easiest ways to measure the temperature is through resistance measurement. It is based on the temperature dependence of an electric conductor. For example, the resistance of pure metals has a linear proportional behavior to the temperature. In order to measure the resistance, the conductor must be current-carrying. Furthermore, it is necessary to reduce the internal heat. For this purpose, the current is kept small, so it does not influence the measurement. A more precise means to measure resistance is given by the Wheatstone bridge, shown in figure 4.1.

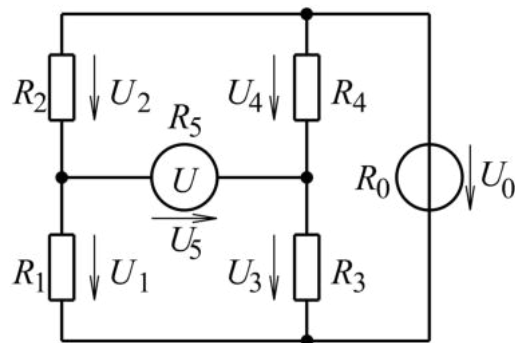


Figure 4.1: Wheatstone bridge [6].

The bridge consists by four resistors which are arranged in a closed loop. Moreover, there is a voltage source U_0 and a voltage measurement U_5 . If temperature changes, the resistors change their resistance and the measured bridge excitation voltage changes. This change which relates to an initial value is detected and is proportional to the temperature. Equation 4.1 applies to a symmetrical bridge, meaning that every resistor has the same resistance R , whereby it is most sensitive. Due to this, one of four resistors must have a strongly temperature dependency with respect to its resistance. The other

ones have to remain as unchanged as possible when the temperature changes.

$$\frac{U_5}{U_0} = \frac{1}{4} \frac{\Delta R_1}{R} \quad (4.1)$$

Another possibility to measure the temperature is a band-gap temperature sensor. This is how the SHT21 measures the temperature. It is exploited that transistors show a highly temperature-dependent behavior in relation to the leakage current. The measurement is based on the difference between the base-emitter voltages of two bipolar transistors operated at different current densities. This can be implemented by two transistors with different emitter surface areas. The electric circuit is shown in figure 4.2.

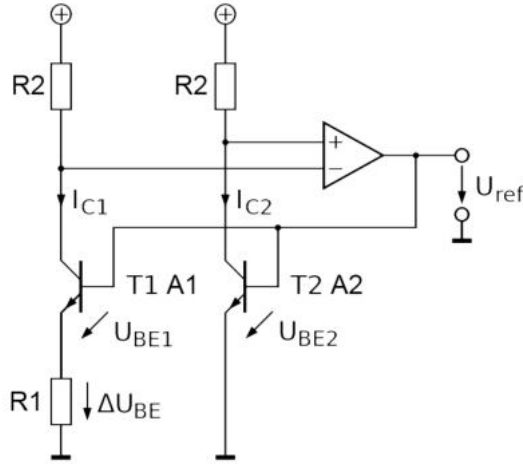


Figure 4.2: Bandgap voltage reference for measurement of temperature [7].

The op-amp ensures that the collector currents are identical. Due to the larger area of one of the transistors, its collector current increases stronger than for the transistor with the smaller area. Later it gets a flatter behavior because of current feedback loops. This difference increases with increasing temperature. It can be calculated with the characteristic transfer functions of the transistors to:

$$\Delta U_5 = \frac{k_B T}{e} \ln(n) \quad (4.2)$$

U_{BE} describes the basis-emitter voltage, k_B is the Boltzmann constant, T is the absolute temperature in [K], e is the elementary charge and n is the fraction of the area of the other transistor. The difference is directly proportional to the absolute temperature and can be used as a measurement of temperature.

4.0.2 Pressure

The measurement of pressure resembles the measurement of temperature. It can be measured with the Wheatstone bridge, too. It is based on a membrane, which is able to react to pressure by changing its shape. The resistor is a strain gauge, which changes its resistance with the distortion indicated by the pressure. The reason for this is the piezoresistive effect which occurs on bending, pressure or traction. Thus the bridge excitation voltage changes as a result of the ambient pressure.

4.0.3 Relative Humidity

At first, a distinction is made between the different types of moisture. The absolute humidity states the amount of water in a specified volume of air. The saturation humidity indicates the maximum amount of water that can be bound in the air. This value strongly depends on the temperature. The SHT21 and the BME280 return the relative humidity. It consists of the ratio between the absolute humidity to the saturation humidity. The simplest idea of measuring it, is to measure the ambient temperature and determining the dew point. But this requires energy for cooling. Most sensors are composed of a capacitor with a capacitance which is determined by the capacitor surfaces A , the distance D between them and a dielectric ϵ_r .

$$C = \epsilon_0 \epsilon_r \frac{A}{D} \quad (4.3)$$

Since the surface and the distance are constant, the proportion of water can be determined by the change of permittivity. Therefore a material is used which dielectric constant depends on humidity, thus, the capacitance C changes with changing humidity. For example aluminum oxide is used as a dielectric. The electrodes are water vapor permeable. The capacitance can be measured by applying an alternating voltage U to the capacitor and measuring the resulting current I which depends on the capacitance.

$$C = \frac{I \Delta t}{\Delta U} \quad (4.4)$$

4.1 I²C - Interface

I²C is an acronym for Inter-Integrated Circuit and was developed by Philips. It is a serial data-bus which connects a microcontroller or a processor, respectively with one or more integrated circuit(s) (IC). In this case the processor is a Raspberry Pi 3B and the ICs are the environmental sensors. It is designed as a master-slave-bus system, where the Raspberry Pi represents the master and the sensors represent the slaves. An example of the schematic is shown in figure 4.3.

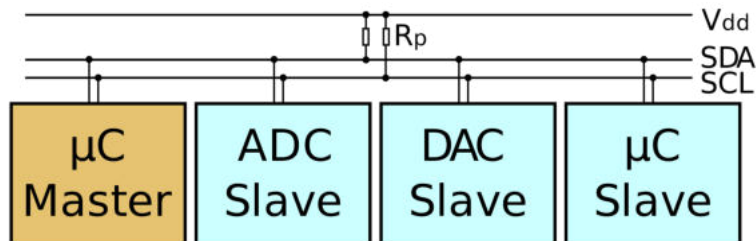


Figure 4.3: Schematic of I²C bus communication with one master and three slaves (an ADC, a DAC and a microcontroller) and the pull-up resistors for SDA and SCL [8].

The master initiates a data transfer. This is done by addressing the slave on its specific address. Afterwards the slave reacts to it. Moreover it is possible to use more than one master. This is called Multi-Master-communication.

As it can be seen, the serial data-bus uses two bidirectional (excluded ground and power supply), open drain lines. The first line is called "serial data line" (SDA) and the second one is called "serial clock line" (SCL). The SDA line is responsible for the transfer of

data, whereas SCL is used to synchronize all data transfer over the bus. Both lines have a logical level, high or low. Furthermore it can be seen that the SDA and SCL lines are connected with pull-up resistors. These ensure that a well-defined logic level can be established. In this case the master entirely controls the SCL line and initiates connections, the sensors are only responding to it.

5. Setup and Procedure

5.1 Carrier Board

To investigate both sensors concerning their radiation hardness, a circuit board composed of two layers was designed with EasyEDA. EasyEDA is a web-based tool to design, simulate, share publicly and privately and discuss schematics, simulations and printed circuit boards. The PCB was designed such that the sensors can be monitored and irradiated independently of each other. Consequently, the entire board does not need to be irradiated.

The main carrier board provides four slots for both sensor types, the SHT21 and the BME280 and thus offers the advantage that more sensors of each type can be examined simultaneously with respect to their radiation hardness. Every sensor has its own address which cannot be changed. This is the reason why a multiplexer was used which is placed in the middle of the board (TCA9546A, Texas Instruments). With its wide operating temperature range between -40°C to $+85^{\circ}\text{C}$, it should not influence the measurements of the sensors. The multiplexer divides the serial data-bus in four separate buses. Each bus/channel includes one SHT21 and one BME280. The development of the carrier board from the schematic to the milled and soldered board is shown in the following figures [5.1-5.3].

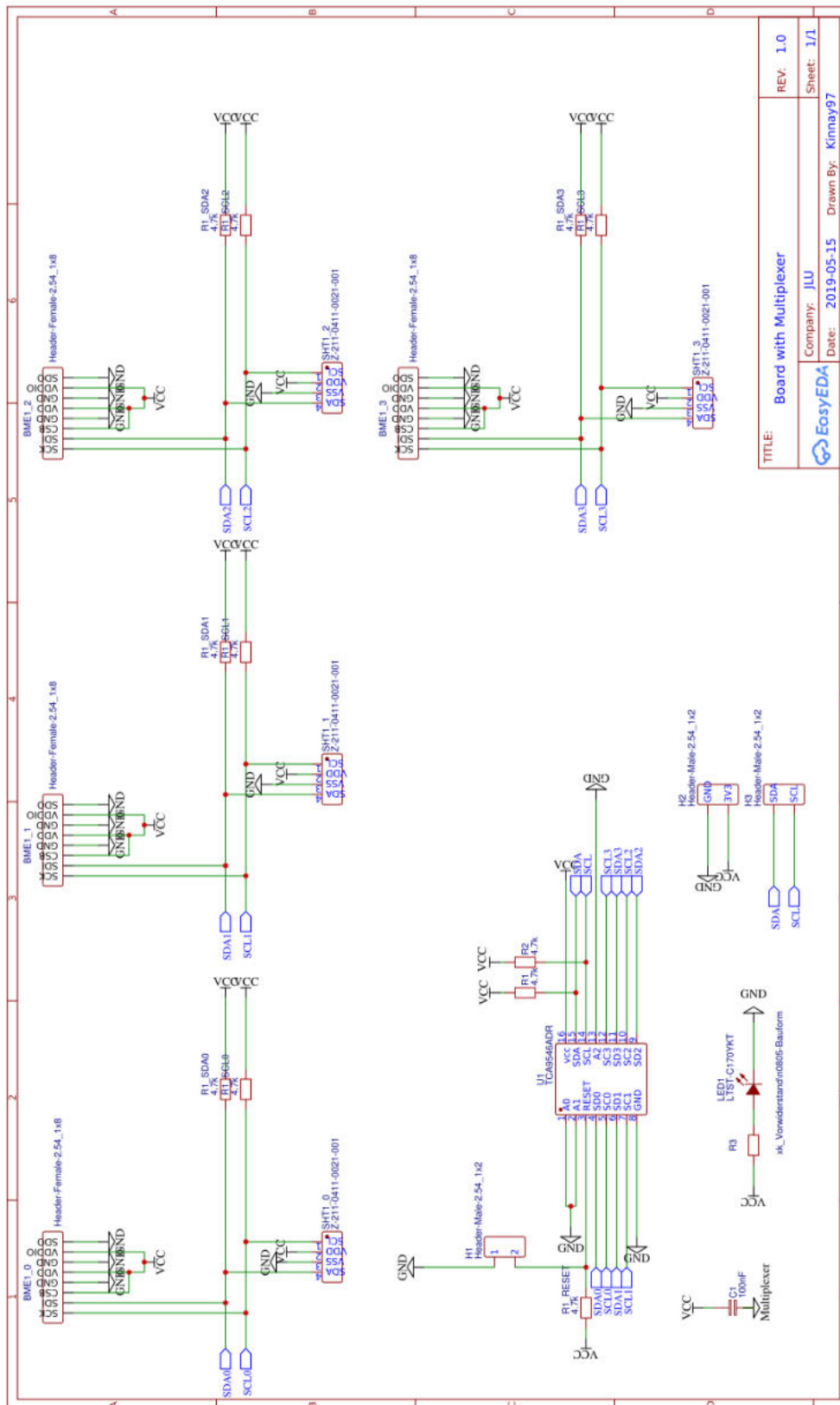


Figure 5.1: Schematic of the circuit board.

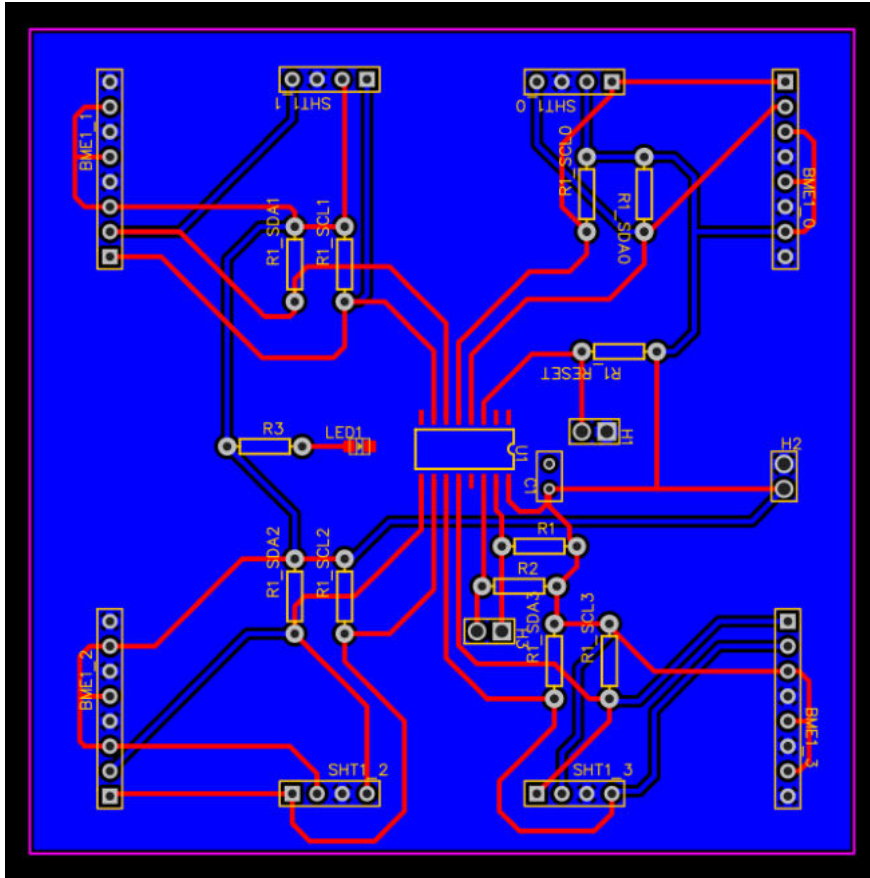


Figure 5.2: PCB of the circuit board, which was constructed with EasyEDA.

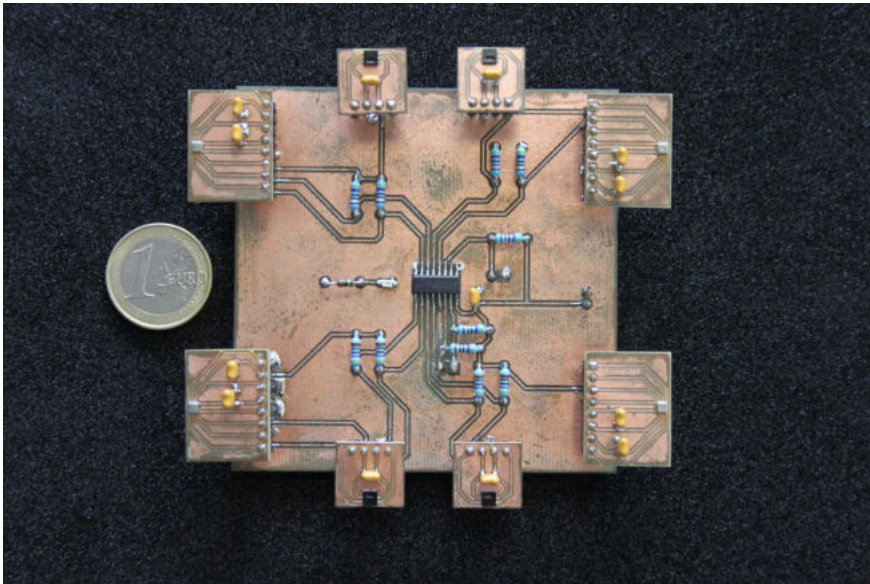


Figure 5.3: Milled version of circuit board with 1€ coin for size comparison.

The circuit board is shown in figure 5.3. The eight independent sensors are attached on their own individual PCBs and can be plugged on the carrier board. For measurements it was placed in a climate test chamber type WK3-340/40 (WEISS) which is shown in

figure 3.4. In there, one can control temperature and humidity. It is explained in more detail in section 5.2.

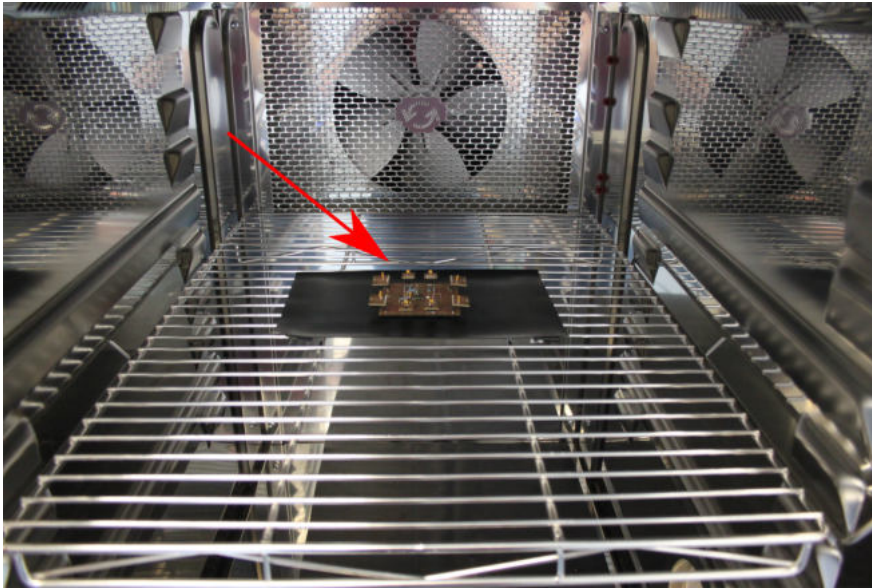


Figure 5.4: Circuit board in climatic chamber without communication cables.

The sensors respectively the multiplexer communicate with a Raspberry Pi 3B via I2C interface. For better accessibility only the carrier PCB and the sensors were placed inside the chamber, while the Raspberry Pi was placed outside, because it is not verified how reliable the Raspberry Pi works at different temperatures and humidities. The connection between the Raspberry Pi and the board is shown in figure 5.5.

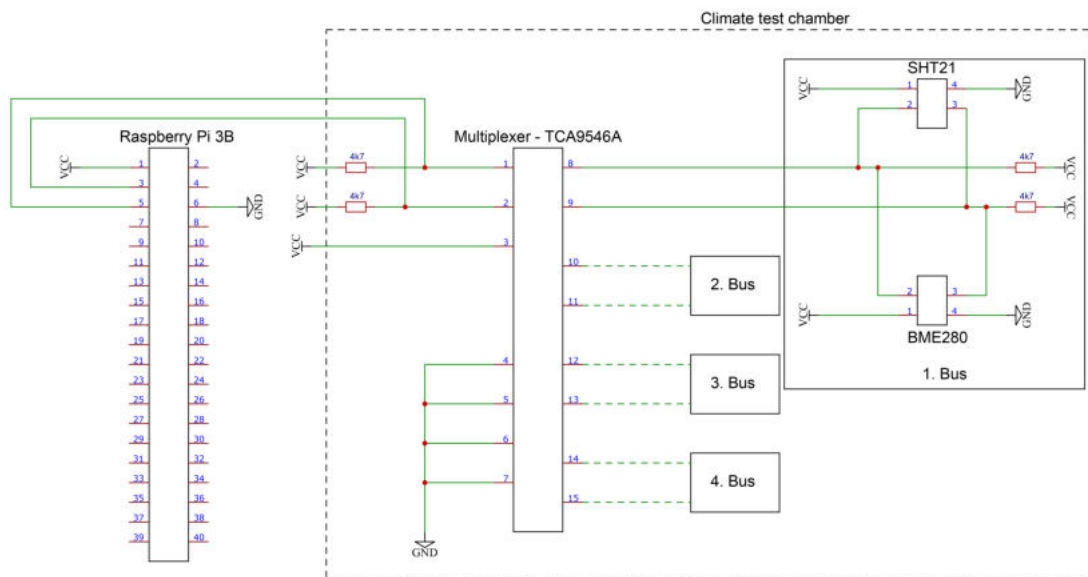


Figure 5.5: Schematic of the setup. One of the split buses is drawn exemplary.

Detailed pin-outs are shown in the appendix 8.1 to 8.3.

As previously explained, it can be seen that the multiplexer switches the master-bus through to four independent slave-buses. The buffer capacitors were omitted from the drawing. They have a capacitance of $C = 100\text{ nF}$ and the pull-up resistors have a resistance of $R = 4.7\text{ k}\Omega$. For the investigation of the sensors it was necessary to have a reference sensor for each type of sensor, which was not irradiated and is also placed in the climate chamber. All eight sensors were examined for different relative humidities from 10% to 50% and different temperatures in a range of $-30\text{ }^{\circ}\text{C}$ to $+30\text{ }^{\circ}\text{C}$. They were read out within one second. Each SHT21 returns a temperature- and a relative humidity value. The BME280 also returns the pressure, which was included in the data, but was not evaluated.

5.2 Climate Test Chamber

The test chamber has a volume of approx. 335l and can control the temperature and relative humidity in the ranges of $-42\text{ }^{\circ}\text{C}$ to $+180\text{ }^{\circ}\text{C}$ and $+10\text{ }\%$ to $+98\text{ }\%$, respectively. The control of moisture is enabled within the temperature range from $+10\text{ }^{\circ}\text{C}$ to $+95\text{ }^{\circ}\text{C}$. A single measurement refers to a constant relative humidity, generated by the chamber.

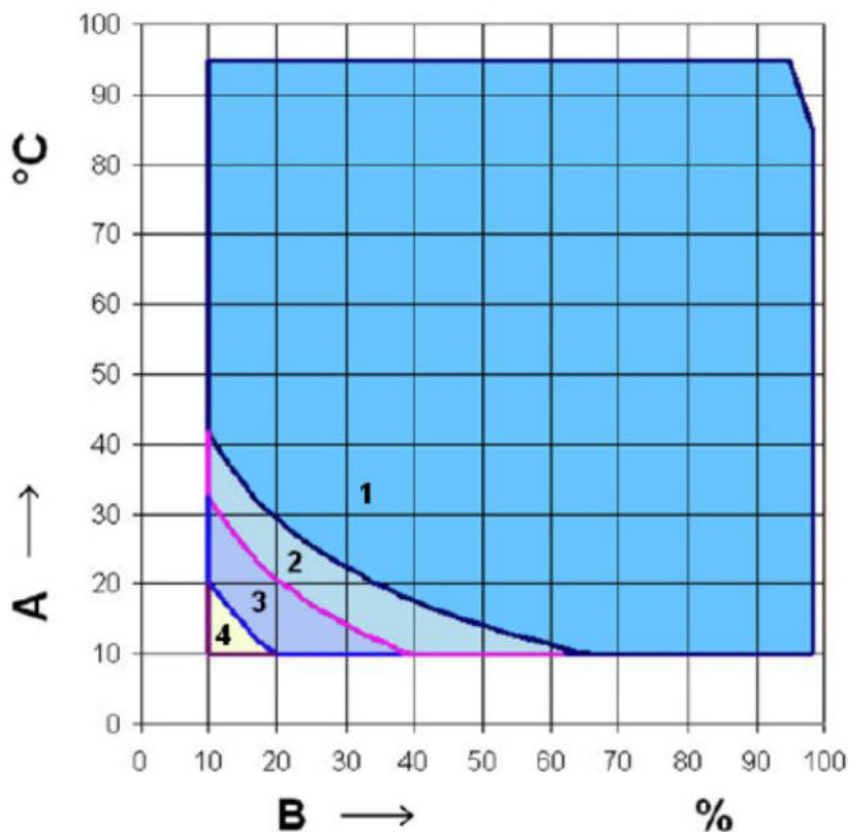


Figure 5.6: Climate state diagram of climate test chamber - relative humidity B versus temperature A[9].

The climate test chamber specification is divided into four different areas which are shown in figure 5.6:

The x-axis shows the relative humidity in [%] and the y-axis shows the temperature

in [°C]. The first area should be reached with the existing default configuration. To reach the second and third area, the compressed air must be connected to the cabinet in the laboratory. Furthermore, reaching of both areas depends on the quality of the compressed air, especially on its dew point. The required dew point for the second and third area amounts -12 °C. A compressed air quality test was carried out. As a result the dew point was measured to be 3 °C. The climate test chamber neither comprises a compressed air dryer nor was an external one available at this time, thus the second and third area should not be accessible. Nevertheless, the cabinet was programmed to cover the second and third area. It was examined with respect to the achievement of the adjusted values and the reproducibility. This is explained in more detail in section 6.2. The fourth range cannot be reached either, since a capacitive moisture measuring system is required for this, which is not installed in the used version of the chamber.

5.3 Procedure

Four identical sensors of each type (SHT21 and BME280) were examined. One reference sensor was defined for each sensor type. These were not irradiated. The other ones were irradiated with a ⁶⁰Co-source and then characterized for different radiation doses. The characterization is carried out at different temperature and humidity curves.

Two different types of programs (A and B) exist for the investigation of the sensors.

Program type A				
relative humidity [%]	temperature range [°C]	step size [°C]	rs	ts
50	[-30; 30]	5	not irr.	not irr.
45	[-30; 30]	5	not irr.	not irr.
40	[-30; 30]	5	not irr.	not irr.
35	[-30; 30]	5	not irr.	not irr.
30	[-30; 30]	5	not irr.	not irr.
25	[-30; 30]	5	not irr.	not irr.
20	[-30; 30]	5	not irr.	not irr.
15	[-30; 30]	5	not irr.	not irr.
10	[-30; 30]	5	not irr.	not irr.

Table 5.1: Run parameters of program A (rs: reference sensors, ts: test sensors). Each row represents one measurement procedure. The humidity was set constant and the temperature was ramped between -30 °C and +30 °C.

Program type B				
relative humidity range [%]	temperature range [°C]	step size [°C]	rs	ts
[10; 50]	[-30; +30]	5	not irr.	irr.

Table 5.2: Run parameters of program B (rs: reference sensors, ts: test sensors). Program type B combined all measurement procedures of program type A.

Program type A includes nine different procedures. Each differ in a constant relative humidity, but covers a temperature range from -30 °C to +30 °C with a step size of $\Delta T = 5$ °C.

Program A was used to investigate the achievement of the set values of the climate chamber with respect to the climate state diagram 5.6. Furthermore, to characterize a

set of sensors before irradiation.

Program A for a relative humidity of $H = 50\%$ is shown in figure 5.7.

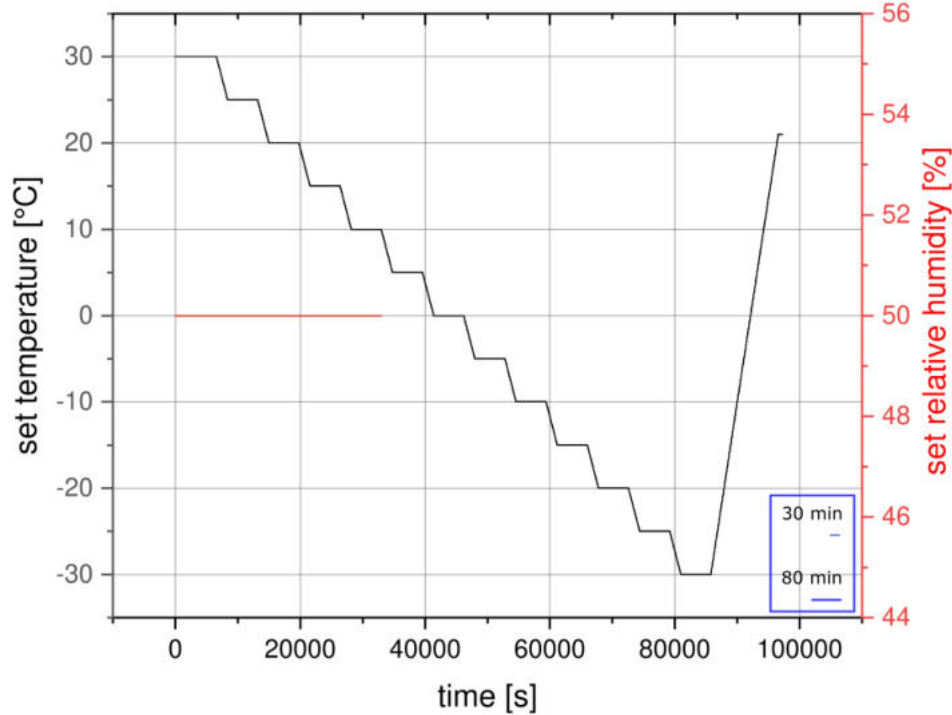


Figure 5.7: Procedure for a relative humidity of $H = 50\%$ of program A.

The time in [s] is plotted on the x-axis, the target temperature in [°C] is plotted on the left y-axis and the target relative humidity in [%] is plotted on the right y-axis.

The graph shows that the temperature was held at a constant value over a time of 80 min¹ and decreased in steps of $\Delta T = 5^\circ\text{C}$ within 30 min. The relative humidity was held constant until the temperature falls below a value of 10 °C². The climate test chamber is not able to regulate the relative humidity below 10 °C.

At a time of 85 500s, it can be seen that the temperature increases within 180 min³ to room temperature, in this case $T = 21^\circ\text{C}$. This is the shutdown procedure of the climate test chamber.

An overview over the programs of type A (with different relative humidities) is shown in the appendix 8.1.

In order to save measuring time, the already existing procedures (for different relative humidities from 10 % to 45 %) of program A were combined to program B. It is divided into different measurement cycles, whereby every cycle covers a temperature range of +10 °C to +30 °C with different relative humidities. For each cycle the humidities were kept constant. It was used to examine the sensors with respect to their radiation

¹For the first three measurements at rel. hum. 50 %, 45 % and 40 %, the holding time was set to 60 min.

²For relative humidities of 15 % and 10 %, the break off temperatures were 15 °C and 20 °C, respectively, see fig. 5.6.

³After the first three measurements (50 %, 45 % and 40 %), the time for the shutdown process was 30 min.

hardness. In this context, the test sensors were examined after each irradiation iteration with program B. Each test sensor received the same dose of radiation per irradiation iteration. Since Program B only covers a temperature range greater than 10 °C, the type A program with a relative humidity of 50% is still used for this investigation of radiation hardness. Program B can be seen in figure 5.8.

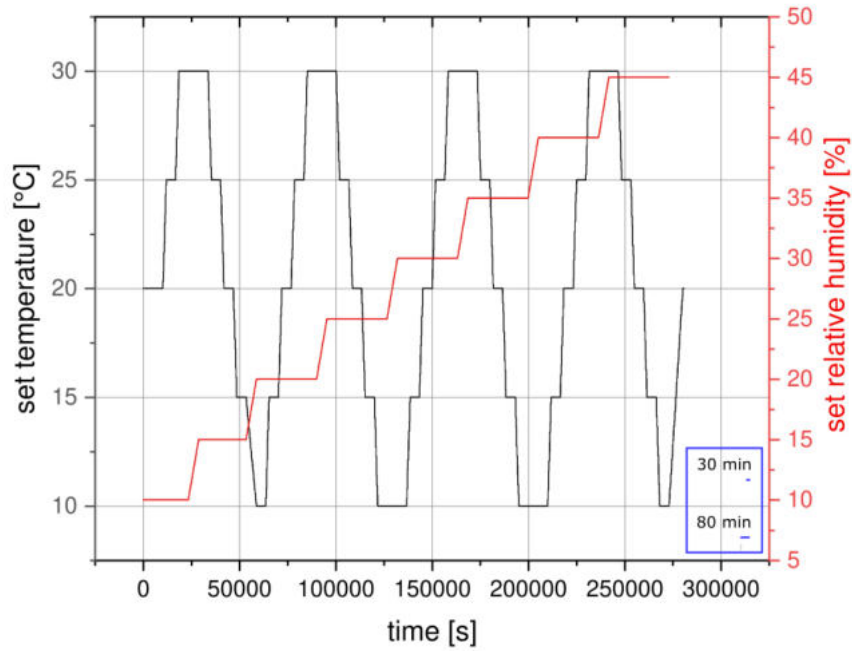


Figure 5.8: Program B for the investigation of radiation hardness.

The transition time between two measurement cycles was 90 min. During this the relative humidity was changed in steps of five percent points. The step size of the temperature is the same as before. Depending on the relative humidity, the break off temperature is varying. After the duration of 273 000 s the procedure for the shutdown can be seen.

5.4 Irradiation

To investigate the sensors with respect to their radiation hardness a ^{60}Co source was used. This was done at the Giessener Strahlencentrum in the so-called Ringschieber. Cobalt-60 decays by β^- -decay into an excited state of ^{60}Ni , which decays into the ground state by emission of a gamma quantum. The associated scheme can be seen in figure 5.9.

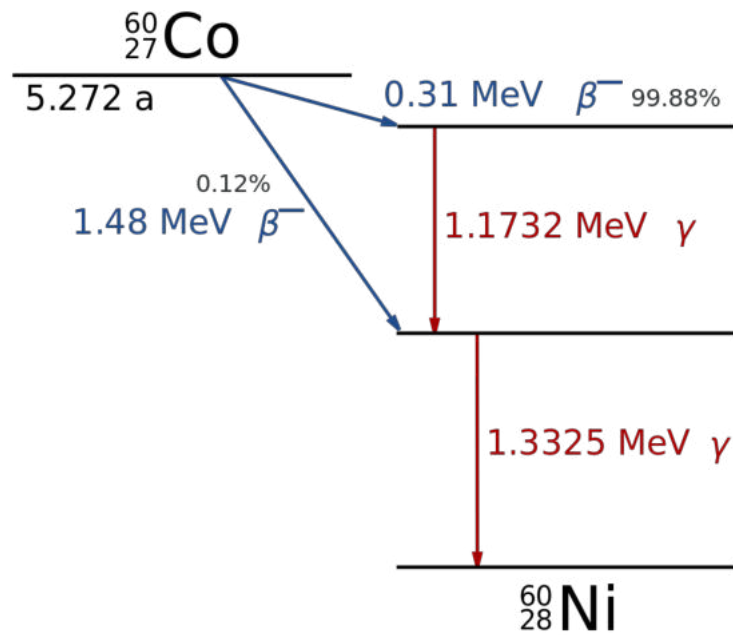


Figure 5.9: ${}^{60}\text{Co}$ decay scheme [10].

The electrons resulting from the beta-decay do not have enough energy to reach the sensors. Effectively the sensors are only exposed to gamma-rays.

The incremental irradiation plan which was carried out can be seen in table 5.3.

#irradiation	single dose [Gy]	accumulated dose [Gy]
1	50	50
2	50	100
3	100	200
4	300	500
5	1500	2000

Table 5.3: Irradiation plan for the sensors, as applied in this thesis.

6. Analysis

As it was mentioned previously (see sec. 5.3), it was determined how well the set temperature or humidity corresponds to the real value. This was always checked in connection with the reference sensors of each sensor type for program type A.

In connection with the irradiation, its effect on the measured temperature and relative humidity of the sensors was investigated. Program type B was carried out five times whereby the climate chamber was analyzed with respect to the reproducibility of the specified values, in particular for the second and third areas in the climate state diagram 5.6 which should not be reached.

It is important to note that one of the sensors of type BME280 seems to have some sort of defect. It falls into a state of not responding to any command from the Raspberry Pi, especially not to the reset command. At first, the only solution was to switch off the power supply. After an operation time of more than 500 hours, the sensor no longer reacts at all. Therefore, only two sensors of type BME280 are tested with respect to their radiation tolerance.

6.1 Temperature Measurement Verification

In order to verify how well the set and measured quantities correspond to each other, the differences between the target and measured values are calculated. The measured values were averaged over a period of approx. 3800 measurements. One measurement corresponds to approx. one second.

The differences originate from the accuracy of holding the set values of the chamber and the sensor itself, but only the standard deviation of the averaged values was used for the evaluation. This can be justified by the fact that the deviation of the climate chamber with regard to the relative humidity in the second and third areas in the climate state diagram is not known due to the absence of the required dew point of the compressed air. Another reason is that there is no specification over the full measurement range given. The temperature difference regarding the SHT21 and BME280 can be seen in figure 6.1 and 6.2, respectively.

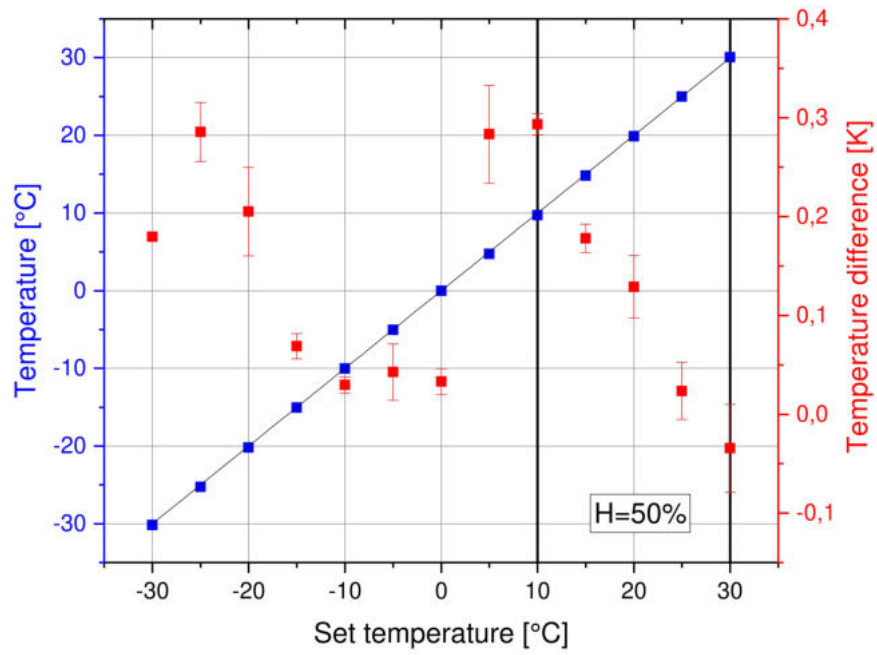


Figure 6.1: SHT21 measured (blue) against set temperature (vertical lines indicate the region of controlled relative humidity.) at $H = 50\%$ and difference of set and measured temperature (red).

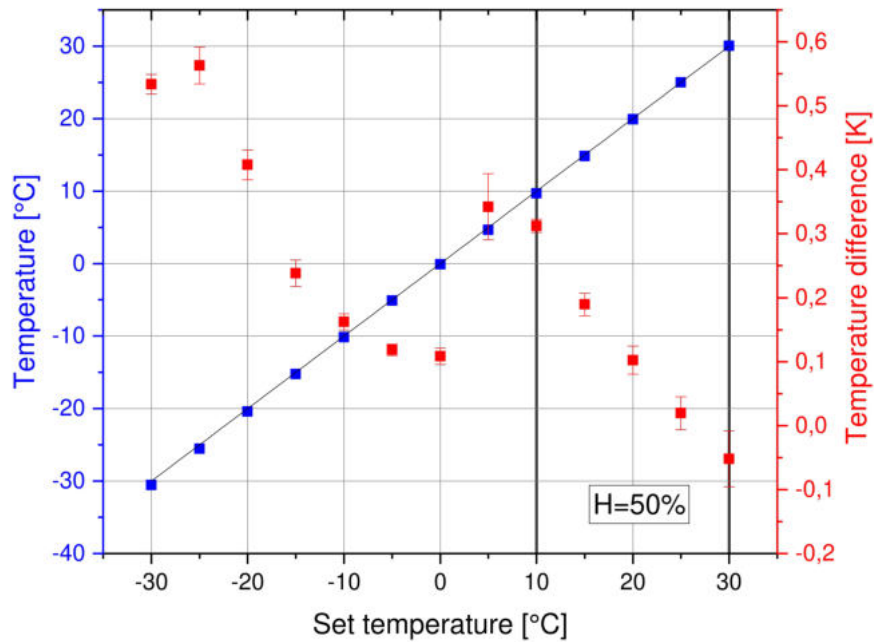


Figure 6.2: BME280 measured (blue) against set temperature (vertical lines indicate the region of controlled relative humidity.) at $H = 50\%$ and difference of set and measured temperature (red).

The target temperature in [°C] is plotted on the x-axis, the measured temperature in [°C] on the left y-axis and the difference of temperature in [K] on the right y-axis. The graphs refer to a relative humidity of $H = 50\%$. The area between vertical lines highlights the temperature range in which the relative humidity is controlled by the climate chamber (see climate state diagram 5.6). In addition, a straight line with a slope of 1 was placed in both graphs which corresponds to the target values. The error bars of the difference correspond to the standard deviation of the measured values.

The graphs show a similar behavior, showing a wave-like character of the temperature difference. Regardless, the temperature difference is in the same order of magnitude and the nominal value is achieved in a good approximation within the specification limits for both sensor types. Therefore, the SHT21 and the BME280 do not differ with regard to temperature measurement.

The following graphs in fig. 6.3 and 6.4 give an overview over the temperature differences at different relative humidities for the examined reference sensors.

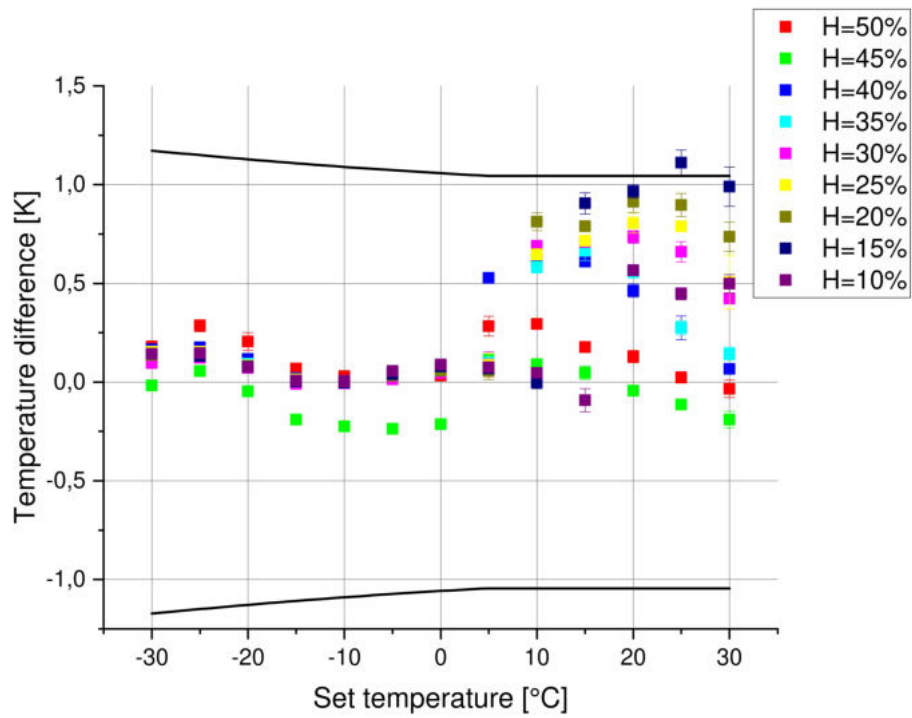


Figure 6.3: Difference of target to measured temperature at different relative humidities for SHT21. Black curve: bound of temperature uncertainty due to climate chamber and sensor. Temperature deviation of the climate chamber (according to the manual [9]) $\Delta T = 1$ K. See datasheet [1] for the temperature accuracy of the SHT21.

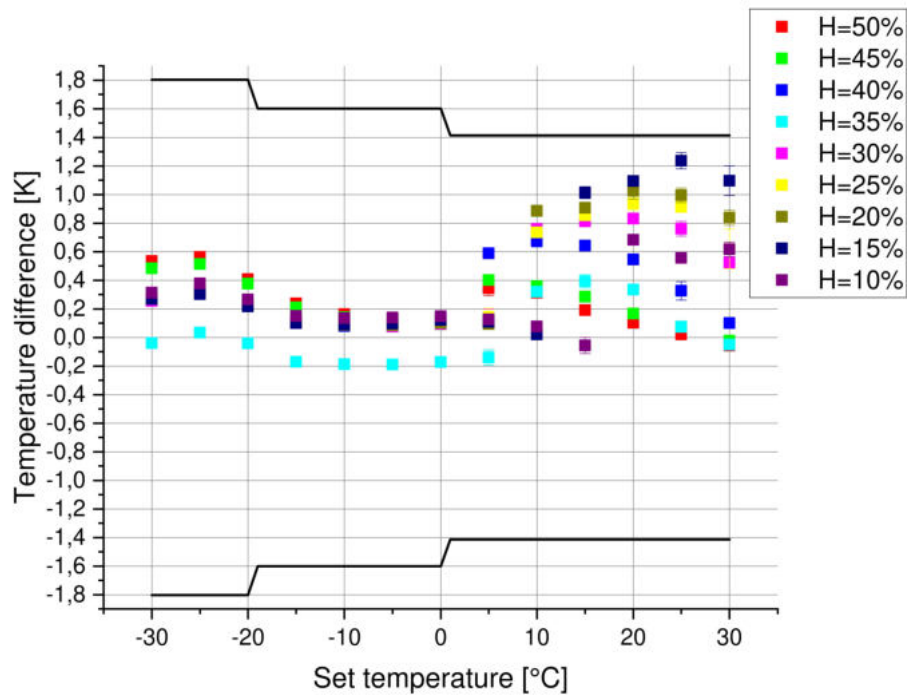


Figure 6.4: Difference of target to measured temperature at different relative humidities for BME280. Black curve: bound of temperature uncertainty due to climate chamber and sensor. Temperature deviation of the climate chamber (according to the manual [9]) $\Delta T = 1$ K. See datasheet [2] for the temperature accuracy of the BME280.

The target temperature in [$^{\circ}\text{C}$] is plotted on the x-axis and the calculated temperature difference in [K] is plotted on the y-axis. Both graphs exhibit the previously described wave character (see fig. 6.1 and 6.2) of the temperature with respect to several relative humidities.

As can be seen, the temperature discrepancy tends to increase with target temperatures above 5°C and decreasing relative humidity.

If the temperature falls below the value of $T = 10^{\circ}\text{C}$, one notices that the difference becomes smaller and from a temperature of $T = 0^{\circ}\text{C}$ on almost all values lie very close to each other.

The inherent temperature uncertainties of the climate chamber and the used sensors amounts to the bound which is shown in figs. 6.3 and 6.4 as black curves. The graphs can thus be used to conclude that the set temperatures were reached in a good approximation, given the technical limitations.

In addition, the relative humidity was also examined. The according graphs can be seen in figure 6.5 and 6.6.

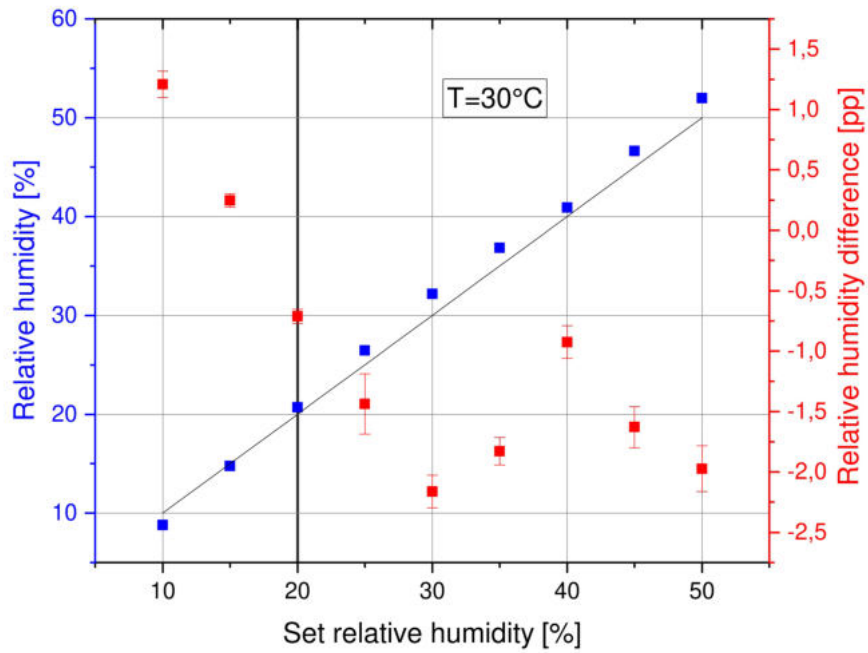


Figure 6.5: Difference of target and measured relative humidity of SHT21 at $T = 30^{\circ}\text{C}$ (vertical line: edge of area 2 in the climate state diagram 5.6).

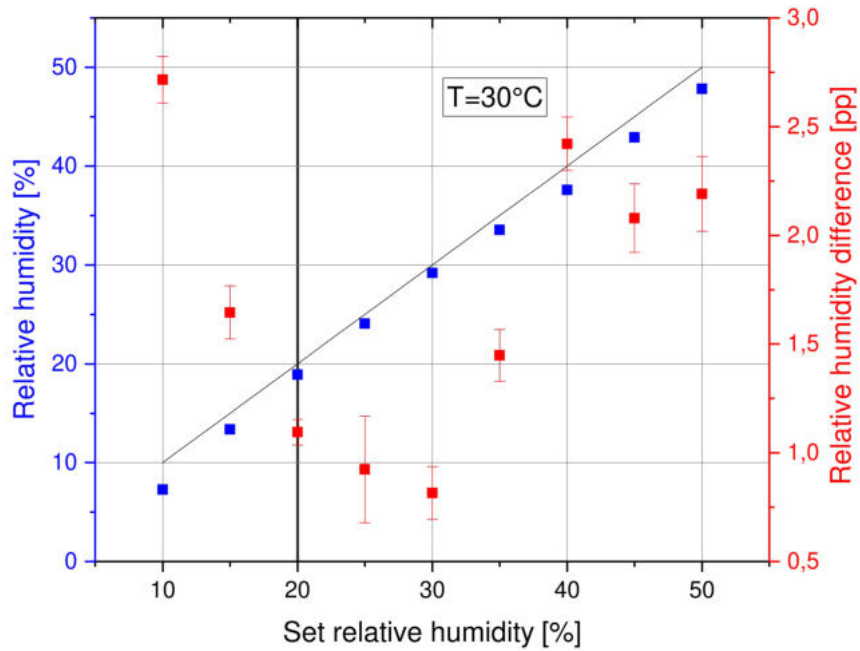


Figure 6.6: Difference of target and measured relative humidity of BME280 at $T = 30^{\circ}\text{C}$ (vertical line: edge of area 2 in the climate state diagram 5.6).

In figure 6.5 and 6.6 the difference of relative humidity is shown (right y-axis) for the SHT21 and BME280 with the actually measured relative humidity (with the reference sensor) on the left y-axis.

The difference was calculated the same way as for the temperature by subtracting the measured averaged relative humidity from the target value. The averaged values of the relative humidity consist of several measurement programs of type A. This is caused by the fact that only one relative humidity has been set for each program/measurement. The second area (with respect to the climate state diagram 5.6) begins below a relative humidity of $H = 20\%$ which is highlighted.

The SHT21 shows a tendency that the differences of relative humidity increase with decreasing moisture. This behavior is observed for relative humidities which are smaller than 30% . The BME280 shows a similar behavior with the addition of an increase towards increasing humidities. Both graphs show characteristic behavior at a relative humidity of 40% . The surrounding differences are lower. However, there is no explanation for this.

In contrast to the SHT21, it can be observed that the moisture differences for the BME280 are positive for all set humidities. Consequently, the SHT21 measures a slightly higher humidity than the BME280.

The following graphs in figure 6.7 and 6.8 give an overview over the differences of relative humidity at different temperatures.

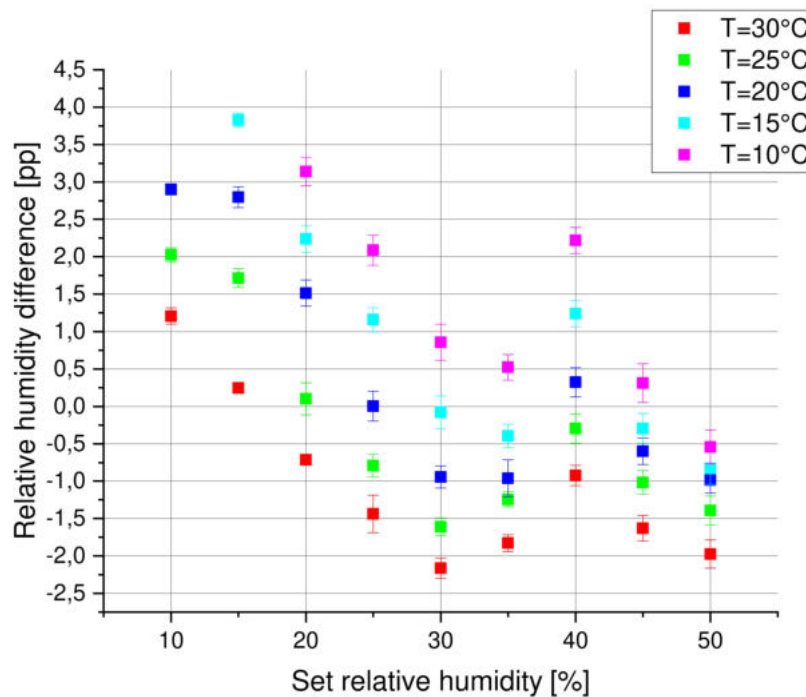


Figure 6.7: Difference of target and measured relative humidities at different temperatures for SHT21.

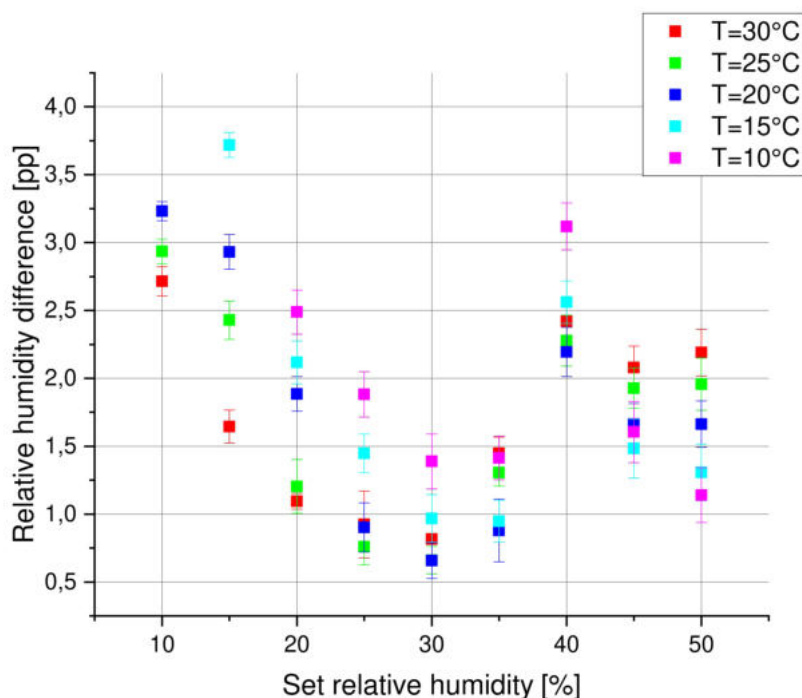


Figure 6.8: Difference of target and measured relative humidities at different temperatures for BME280.

The difference of the relative humidity in [pp] (y-axis) in dependence of the set relative humidity (x-axis) is shown in figs. 6.7 and 6.8.

In general, the overviews confirm the described behavior with respect to fig. 6.5 and 6.6. The same characteristic behavior at $H = 40^\circ\text{C}$ is observed.

Furthermore, the differences for a fixed temperature increase with decreasing relative humidity. This behavior can be seen for relative humidities which are lower than $H = 30\%$ and is shown by the SHT21 and the BME280.

With respect to the SHT21, it can be noted that for maintained relative humidity, the difference increases with decreasing temperature, a behavior not shown by the BME280. As can be seen in the graph, its distribution of differences is arbitrary for fixed relative humidity.

The accuracies of the relative humidity concerning the climate chamber are not known due to the fact that the required dew point is not available for the second and third area in the climate state diagram (see fig. 5.6). Moreover, the systematic deviations of the moisture measurement with respect to the BME280 are not completely known. Therefore, it is impossible to make a statement how well the set humidities were reached. Despite the fact that no statement can be made, the full temperature and humidity ranges were evaluated. For the radiation damage, the repeatability (relative to the reference sensor) is of interest.

6.2 Repeatability Tests

The main focus with respect to program B (see 5.8) was on the reproducibility of the set values concerning the climate chamber. It was checked whether the calculated

differences between target and measured (averaged over approx. 3800 measurements) quantity are reproducible. For this, it was exploited that program B was carried out five times as part of the radiation hardness study.

For several iterations of the same program B, the temperature difference, measured by the SHT21 is shown in figure 6.9.

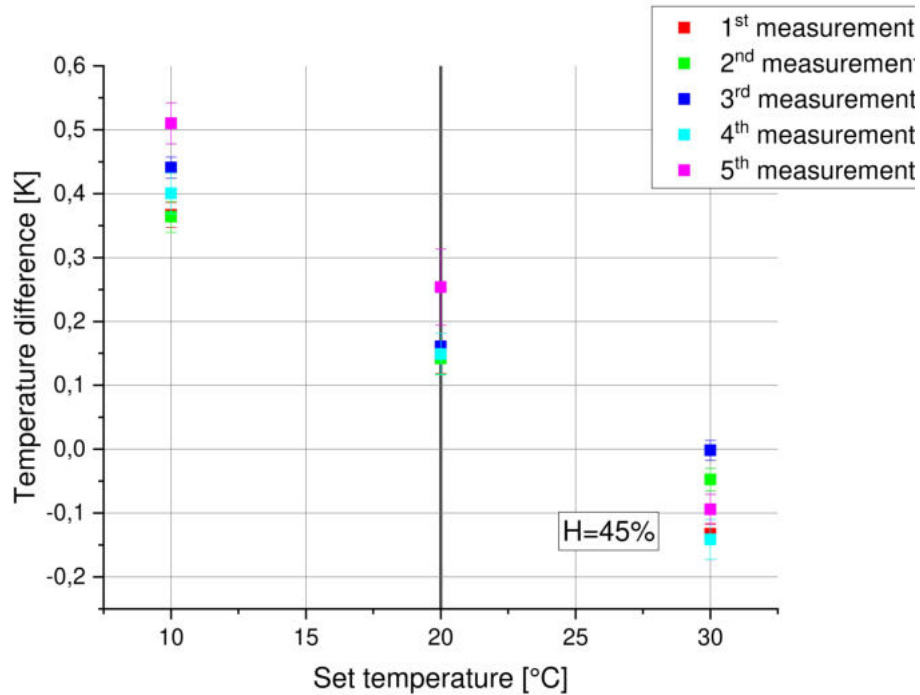


Figure 6.9: Temperature difference at $H = 45\%$ for SHT21. Vertical line: edge of area 2 in the climate state diagram 5.6.

The temperature difference in [K] (y-axis) versus the target temperature in [°C] is plotted.

Below a temperature value of $T = 20\text{ }^{\circ}\text{C}$, which is highlighted with a thick line, the climate chamber reaches the second area in the climate state diagram 5.6.

The graph presents an increasing of the absolute temperature difference for decreasing temperature from $30\text{ }^{\circ}\text{C}$ to $10\text{ }^{\circ}\text{C}$. As can be seen in the appendix [8.2-8.16], this behavior is not verified for different humidity levels, as shown with respect to program A.

Furthermore, it can be observed that the temperature differences of different iterations at a fixed temperature vary slightly from each other.

The deviations of temperature differences at a maintained temperature increase very slowly for lower humidities. Even for $H = 10\%$ one does not observe a big difference in fluctuation. This can be seen in figure 6.10.

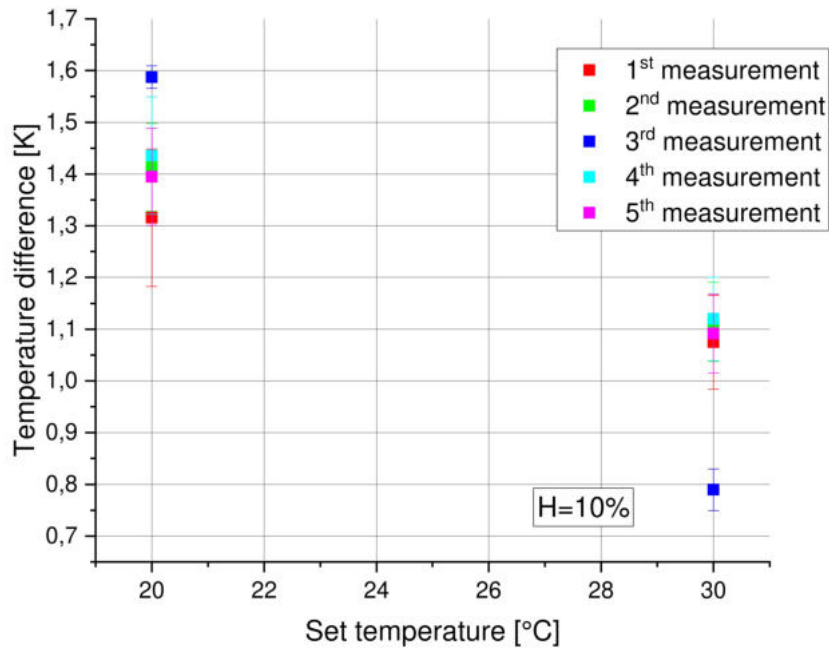


Figure 6.10: Temperature difference versus the set temperature. The temperature difference is given by the difference between measured temperature at $H = 10\%$ and the set temperature for SHT21.

Only two set temperatures were examined for relative humidities below a value of $H = 20\%$. Lower temperatures were not taken into account since these values belong to the fourth area in the climate state diagram (see fig. 5.6) and it was assumed that the chamber is not able to reach this area.

The max. deviation in temperature with respect to several iterations of the same program amounts to 0.33 K.

In order to ensure the determination of damage caused by irradiation, this fluctuation has to be taken into account. Further graphs can be found in the appendix [8.2-8.16]. Afterwards the BME280 was also tested in relation to the deviations of temperature difference.

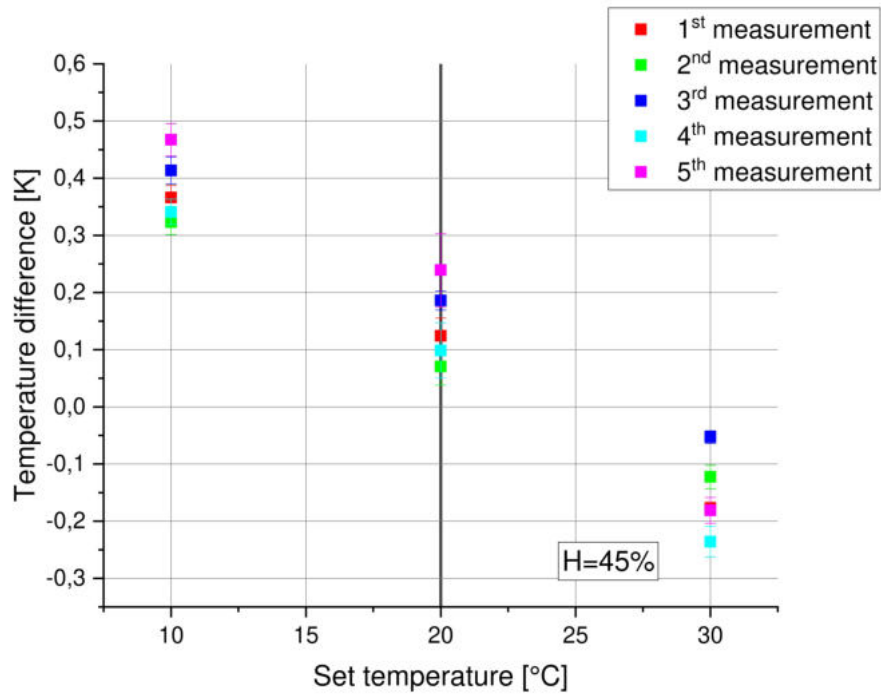


Figure 6.11: Temperature difference versus the set temperature at $H = 45\%$ for BME280. Vertical line: edge of area 2 in the climate state diagram 5.6.

Figure 6.11 and the appendix [8.2-8.16] present a similar behavior with regard to the SHT21, but the max. fluctuation is higher as for the SHT21. It amounts to 0.56 K. In the next step, the relative humidity was examined. The plots [6.12-6.14] give an overview over the difference of relative humidity with respect to the SHT21.

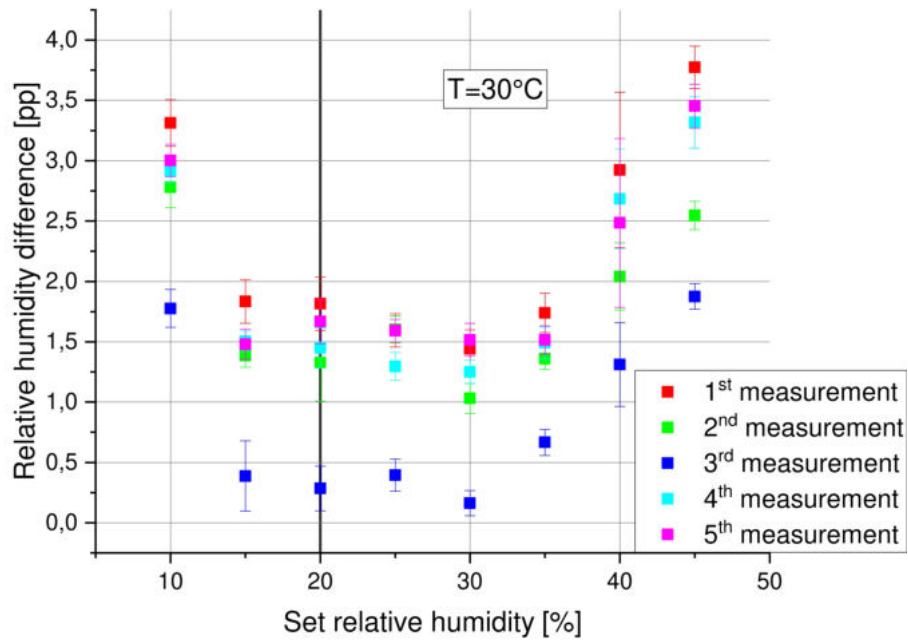


Figure 6.12: Relative humidity difference versus the set relative humidity with respect to the SHT21. Vertical line: edge of area 2 in the climate state diagram 5.6.

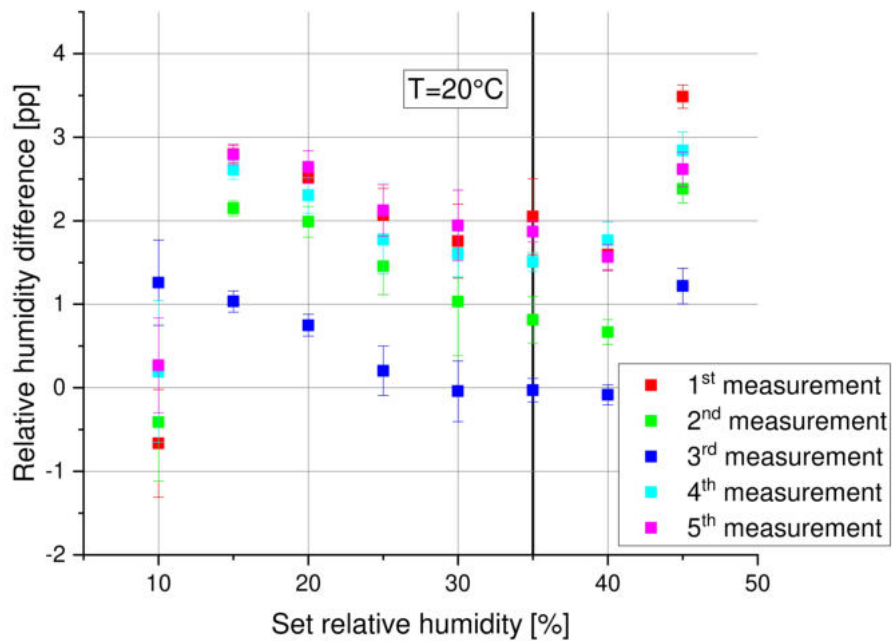


Figure 6.13: Relative humidity difference versus the set relative humidity with respect to the SHT21. Vertical line: edge of area 2 in the climate state diagram 5.6.

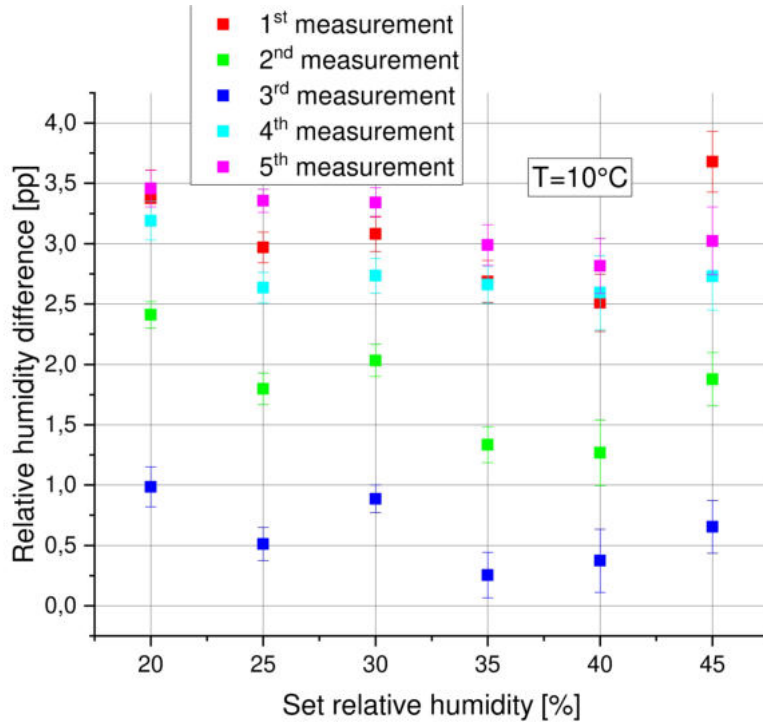


Figure 6.14: Relative humidity difference versus the set relative humidity with respect to the SHT21. Vertical line: edge of area 2 in the climate state diagram 5.6.

The difference of relative humidity (y-axis) in [pp] is given by the difference between the measured relative humidity at 30 °C, 20 °C and 10 °C and the set relative humidity (x-axis in [%]).

It can be seen that the difference tends to increase for decreasing moisture at a constant temperature. With decreasing temperature, an increase of the humidity difference and a broadening of the distribution can be observed. The distributions do not vary significantly for different relative humidities at equal temperatures. An overview over the maximum deviations at different temperatures is given in table 6.1.

set temperature [°C]	max. deviation of moisture [pp]
30	1.92
20	2.37
10	3.27

Table 6.1: Maximum deviations of relative humidities at different temperatures for the SHT21.

Moreover, it can be noted in figs. 6.12, 6.13 and 6.14 that the differences which stemming from the third iteration have the largest variance to the other ones. This can be seen in each of the three graphs. In addition, it can be observed that the differences at $H = 10\%$ deviates from the other ones at temperature of 20 °C.

The moisture measurement of the BME280 yields only marginally different results as for the SHT21. The difference of relative humidity can be seen in figs. [6.15-6.17].

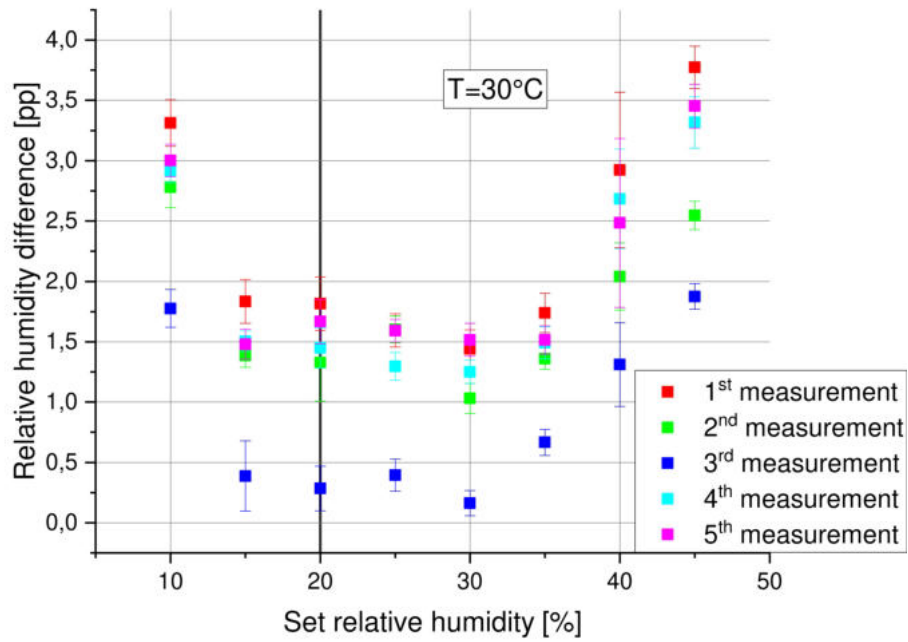


Figure 6.15: Relative humidity difference versus the set relative humidity with respect to the BME280. Vertical line: edge of area 2 in the climate state diagram 5.6.

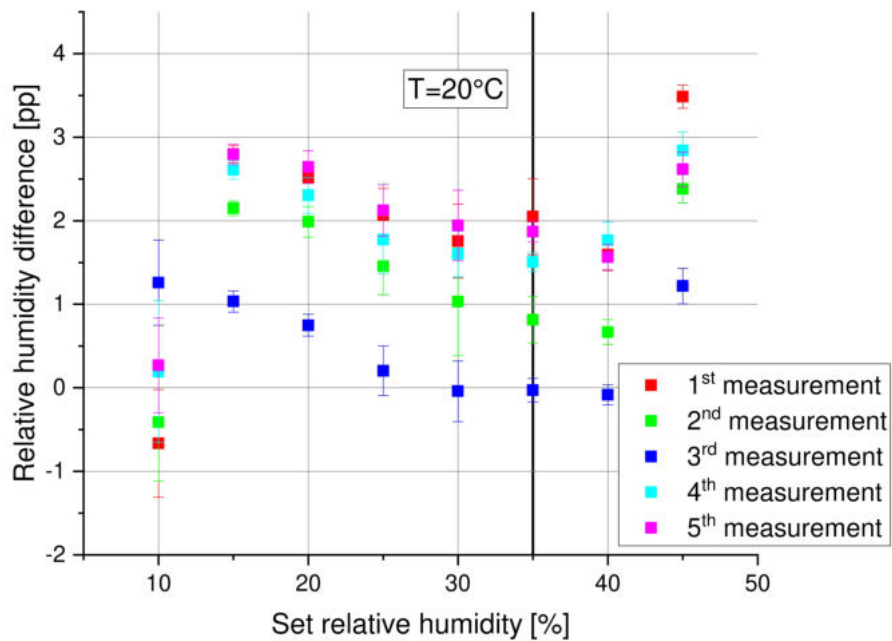


Figure 6.16: Relative humidity difference versus the set relative humidity with respect to the BME280. Vertical line: edge of area 2 in the climate state diagram 5.6.

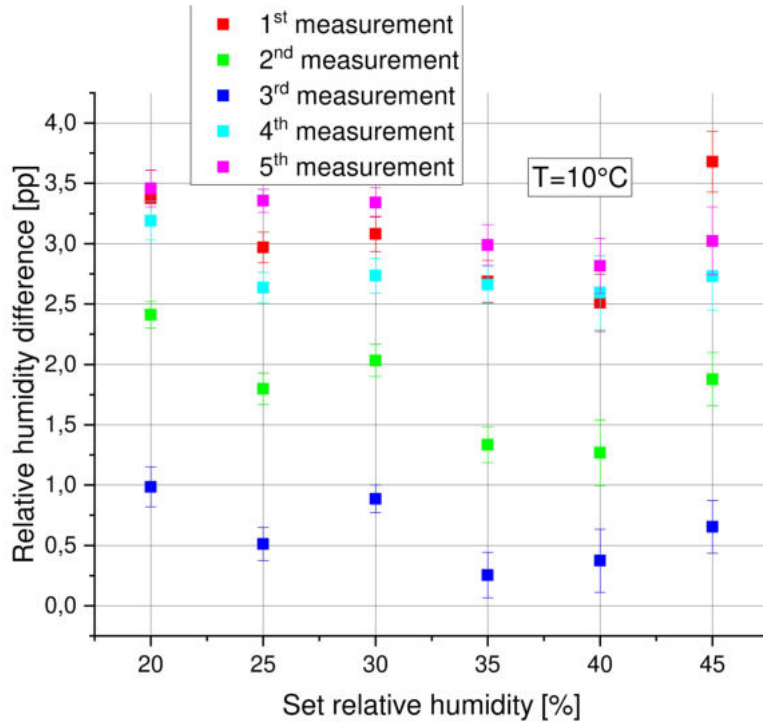


Figure 6.17: Relative humidity difference versus the set relative humidity with respect to the BME280. Vertical line: edge of area 2 in the climate state diagram 5.6.

In contrast to the SHT21, the difference does not increase systematically with decreasing moisture. Otherwise its behavior is similar to the SHT21. An overview over the maximum deviations at different temperatures is given in table 6.2.

set temperature [°C]	max. deviation of moisture [pp]
30	1.90
20	2.27
10	3.03

Table 6.2: Maximum deviations of relative humidities at different temperatures with respect to the BME280.

In general, it can be concluded that for both sensors the reproducibility gets worse with decreasing temperature. The maximum deviations with respect to the relative humidity in tables 6.1, 6.2 have to be taken into account for the radiation hardness investigation of the sensors.

6.3 Outages of the BME280

Within the previous measurements, it was observed that each used BME280 had temporary failures in the measurement of relative humidity and pressure. The temperature measurement of the respective sensor delivers a temperature of exactly 0°C. The SHT21 was used to verify the measured temperature, which means that the temperature measurement is largely intact during the failure.

In general, these failures only happen at a temperature of 0°C . This leads to the phase transition and the water freezes.

It has to be noted that a temperature measurement of 0°C does not imply a failure of the measurement quantities mentioned.

An overview of the registered failures of the type BME280 sensors used is shown in figure 6.18.

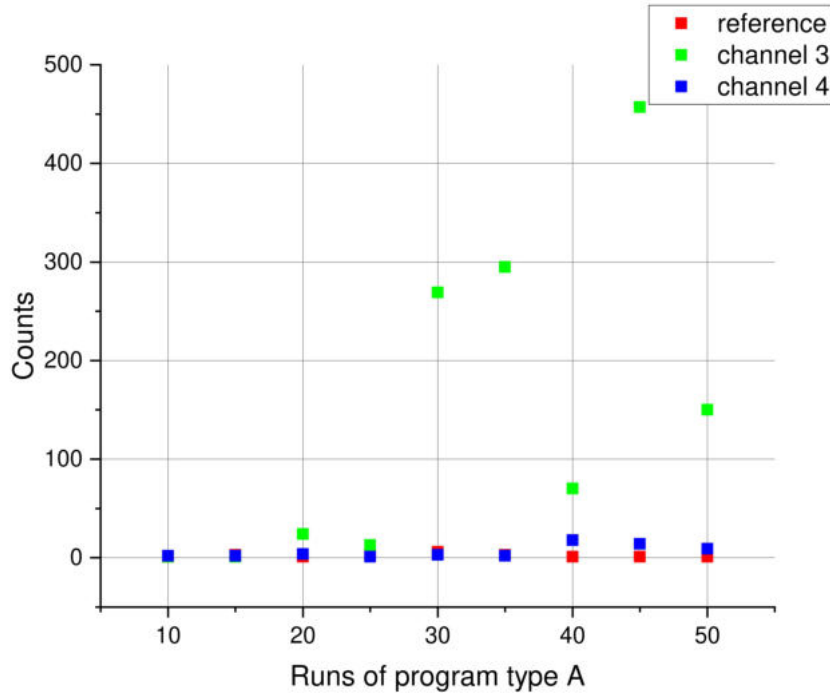


Figure 6.18: Outages of different sensors of the same type (BME280) for different moistures at $T = 0^{\circ}\text{C}$.

Different procedures of program type A (see 5.1) were carried out and are plotted on the x-axis. The number of outages are shown on the y-axis. All sensors were non-irradiated for this measurement.

The legend shows which channel or bus of the multiplexer the sensor was connected to, whereby "reference" means the reference sensor.

As can be seen from the graph, the outages do not show a systematic behavior. It seems like one of the BME280 which is connected with channel 3 tends to fail more often. The maximum of it is approx. at 450 counts. This corresponds to approx. seven and half minutes of dead time due to outages of a total of approx. 27 hours. Each outage lasts only for a short time of a few seconds. However, this time varies slightly.

In the context of the fact that program B was carried out five times, the reproducibility of this fault was checked which can be seen in figure 6.19.

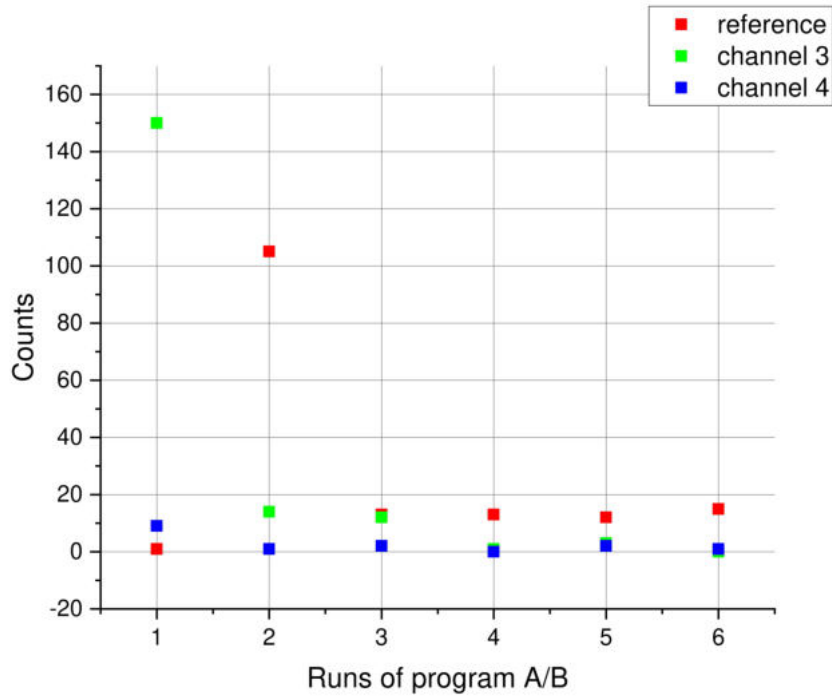


Figure 6.19: Outages of different sensors of the same type (BME280) for a relative humidity of $H = 50\%$ at $T = 0^\circ\text{C}$.

The x-axis shows the sequences of acquisition runs and the number of counted failures is given on the y-axis.

Two out of three sensors were irradiated.

It can be seen that the number of outages is not necessarily related to a special sensor. They are very arbitrary, thus it can be concluded that the irradiation does not influence the outages.

6.4 Radiation Hardness

In order to determine the influence of radiation, the change of the measured quantities before and after irradiation has to be compared. Therefore, the difference between the reference sensor and the test sensor (irradiated) was calculated with respect to the temperature and the relative humidity. To ensure an adequate comparison, the difference was determined before the test sensors were irradiated. This can be seen in figure 6.20 with respect to the settings in program A (with a set relative humidity of 50 %, see table 5.1).

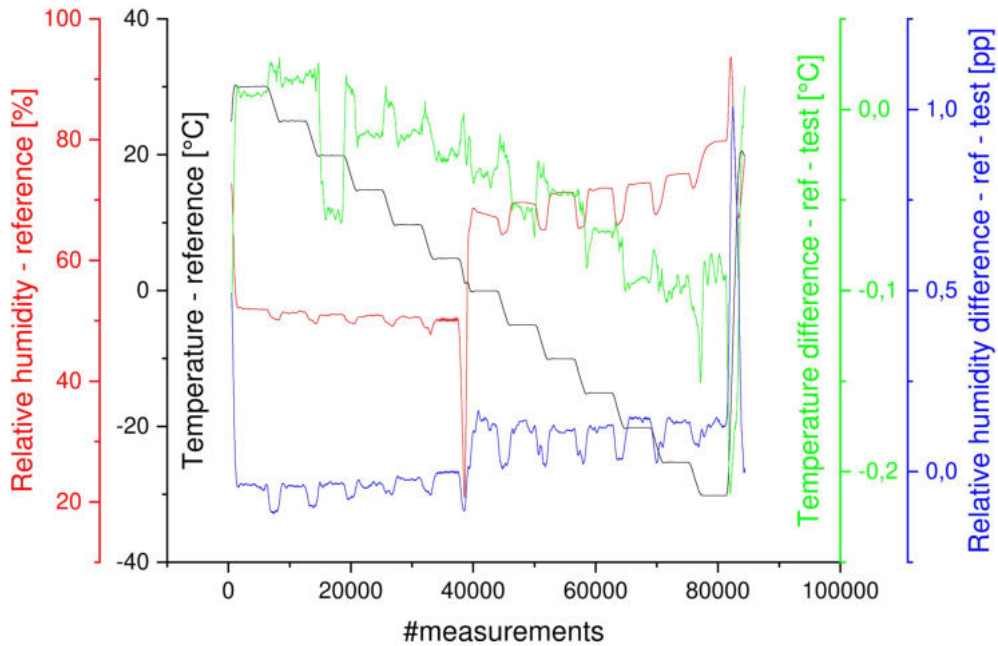


Figure 6.20: Difference of temperature and relative humidity for $H = 50\%$ with respect to the SHT21.

The number of measurements which corresponds to a measuring time is plotted on the x-axis. The black y-axis shows the measured temperature in $[\text{°C}]$, the red y-axis shows the measured relative humidity in $[\%]$, the green y-axis shows the temperature difference in $[\text{K}]$ and the blue y-axis shows the relative humidity difference in $[\text{pp}]$. The values were smoothed using a moving average fit. The relative humidity and the temperature were measured by the reference sensor of the SHT21.

Step flanks can be registered with respect to every entered curve. These are caused by the changing of temperature or relative humidity. They are particularly large at the beginning and the end of the measurement, since the change in temperature and relative humidity is greatest.

Furthermore, the graph shows a decrease of relative humidity within the change of temperature from 5°C to 0°C . The reason for this is that the freezing point of water is reached and thus the residual moisture in the cabinet freezes.

The comparison of these plots (before and after irradiation) is very difficult which is why the evaluation in relation to the temperature and relative humidity was changed to the graphs in figure 6.21.

6.4.1 Temperature - Radiation Hardness

The temperature difference (y-axis) in $[\text{K}]$ in dependence of the target temperature (x-axis) in $[\text{°C}]$ with respect to different radiation doses up to 2000 Gy for the SHT21 is shown in fig. 6.21.

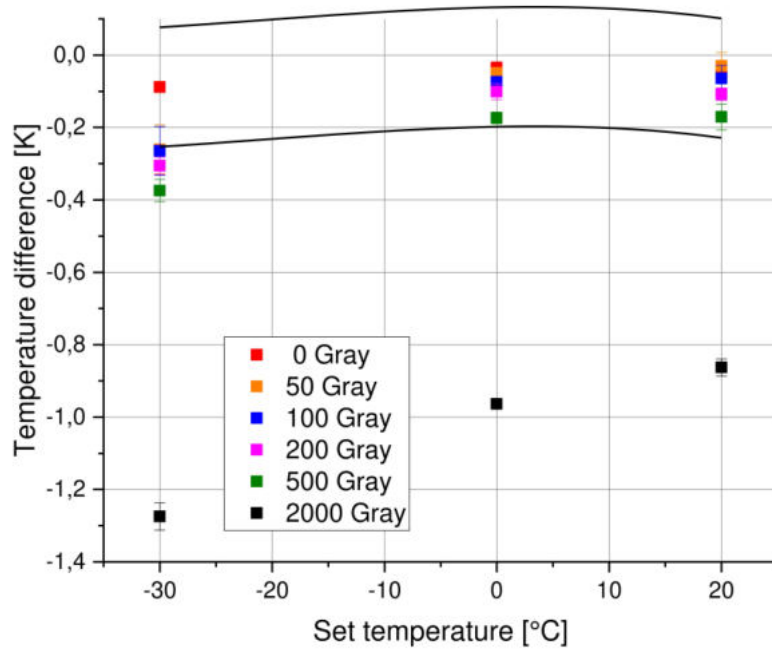


Figure 6.21: Temperature difference between reference sensor and test sensor (SHT21, channel 2) for $H = 50\%$; full irradiation plan (see table 5.3); marked tube: represents the fluctuations of the entire system.

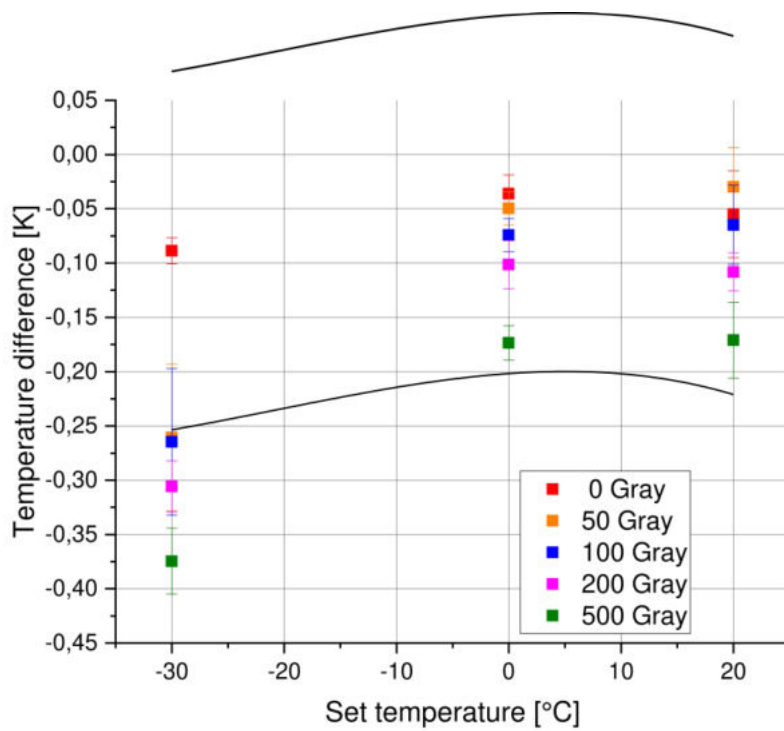


Figure 6.22: Zoom of figure 6.21.

Three different temperatures ($T = -30\text{ }^{\circ}\text{C}$, $T = 0\text{ }^{\circ}\text{C}$ and $T = 20\text{ }^{\circ}\text{C}$) were examined at a set relative humidity of $H = 50\%$ (except for $-30\text{ }^{\circ}\text{C}$). For other relative humidities the temperatures $T = 10\text{ }^{\circ}\text{C}$, $T = 20\text{ }^{\circ}\text{C}$ and $T = 30\text{ }^{\circ}\text{C}$ were examined. This is caused by program B which does not cover the temperature below $10\text{ }^{\circ}\text{C}$.

The temperature difference was calculated from the averaged measured value of the reference sensor and the averaged value of the test sensor. The error bars were calculated with the following equation.

$$\sigma_{res} = \sqrt{\sigma_{ref}^2 + \sigma_{test}^2} \quad (6.1)$$

With: standard deviation of reference and test sensor σ_{ref} and σ_{test} .

The marked tube is the area representing the statistical fluctuations and the fluctuations caused by reproducibility of one measurement (0 Gy). If there is a temperature difference outside the tube, this is probably due to radiation damage.

As can be seen in the graph, the absolute temperature difference tends to increase with increasing dose. The differences are only out of the band after an accumulated dose of 2000 Gy with respect to the temperatures of $0\text{ }^{\circ}\text{C}$ and $20\text{ }^{\circ}\text{C}$.

For the temperature of $-30\text{ }^{\circ}\text{C}$, the difference which belongs to an accumulated dose of 200 Gy is well outside the band.

The other test sensors have to be taken into account, too. The corresponding graphs can be seen in figure 6.23 and 6.24.

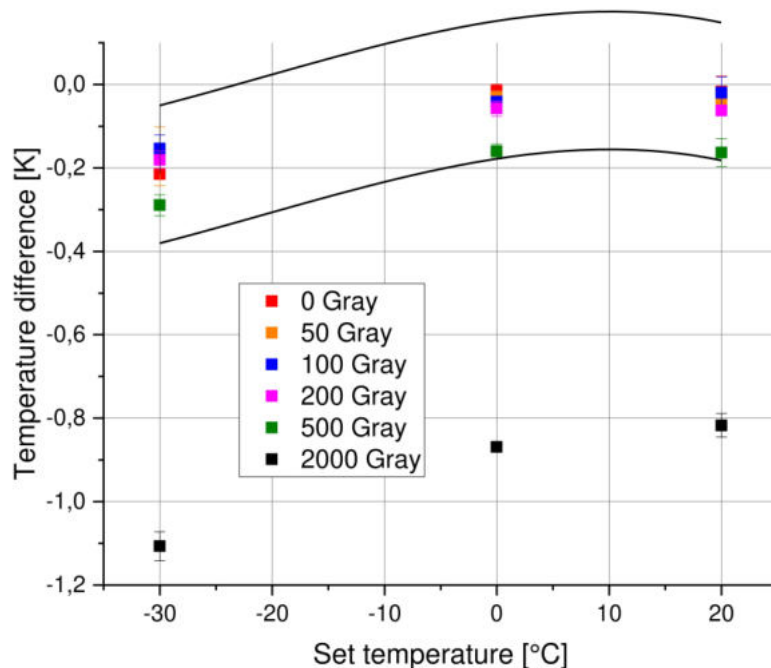


Figure 6.23: Temperature difference between reference sensor (SHT21, channel 3) for $H = 50\%$; full irradiation plan (see table 5.3).

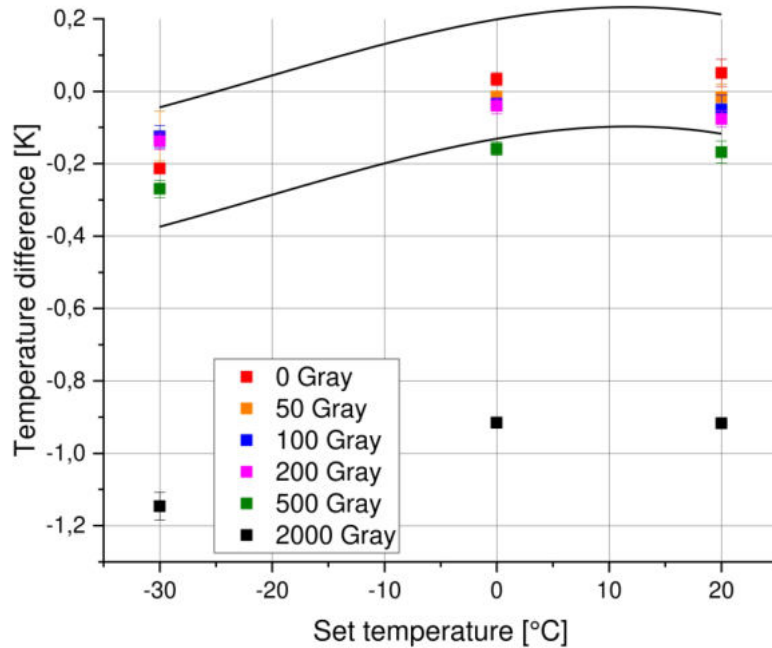


Figure 6.24: Temperature difference between reference sensor and test sensor (SHT21, channel 4) for $H = 50\%$, full irradiation plan (see table 5.3).

Both graphs (figs. 6.23 and 6.24) show the tendency that the absolute temperature differences increase with increasing dose for the SHT21. In figure 6.23 it can be seen that all differences that occur underneath an accumulated dose of 2000 Gy are located within the boundary. The test sensor which belongs to the fourth channel already shows a reaction from 500 Gy with respect to 0°C and 20°C .

A comparison of the different test sensors shows that the change in absolute temperature is in the same order of magnitude. It can be recognized that the test sensor (channel 2) reacts much earlier with respect to -30°C to the irradiation. Thus, it can be assumed that the SHT21 sensors acts different according to radiation hardness (related to the temperature) for -30°C . Further measurements for lower temperatures than 0°C have to be done.

The slight differences between the different sensors of the same type (figs. 6.21, 6.23 and 6.24) can be ascribed to the accuracy of the sensors. Otherwise, the sensors show a similar behavior among themselves.

Further graphs can be seen in the appendix [8.17-8.31].

The next step was to examine the BME280 with respect to the temperature. The related graphs can be seen in figure 6.25 and 6.26.

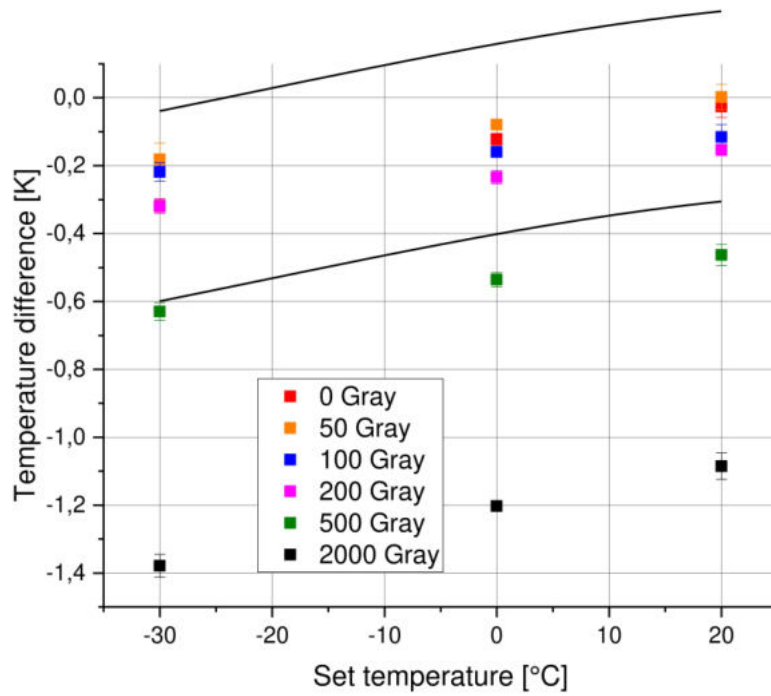


Figure 6.25: Temperature difference between reference sensor and test sensor (BME280, channel 3) for $H = 50\%$; full irradiation plan (see table 5.3).

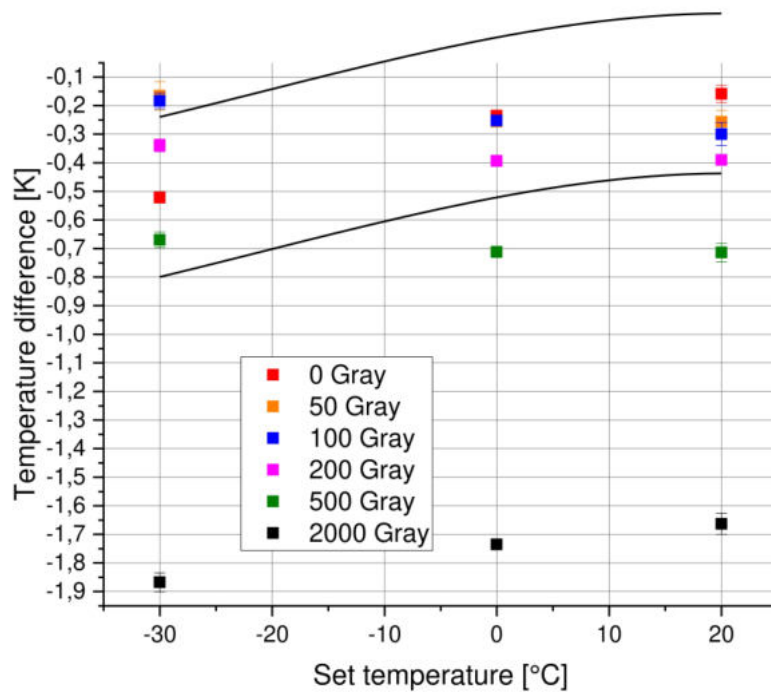


Figure 6.26: Temperature difference between reference sensor and test sensor (BME280, channel 4) for $H = 50\%$; full irradiation plan (see table 5.3).

It can be seen in figure 6.25 that from 500 Gy onwards, the differences are located outside of the boundary. The difference at -30°C which belongs to an accumulated dose of 500 Gy with respect to the test sensor at channel 4 is located inside the boundary. It appears that the SHT21 shows a slightly better behavior in radiation hardness for target temperatures of 0°C and 20°C .

6.4.2 Relative Humidity - Radiation Hardness

Subsequently, the SHT21 was investigated with respect to the change of relative humidity. For this purpose, the differences of relative humidity for different doses are shown in figure 6.27.

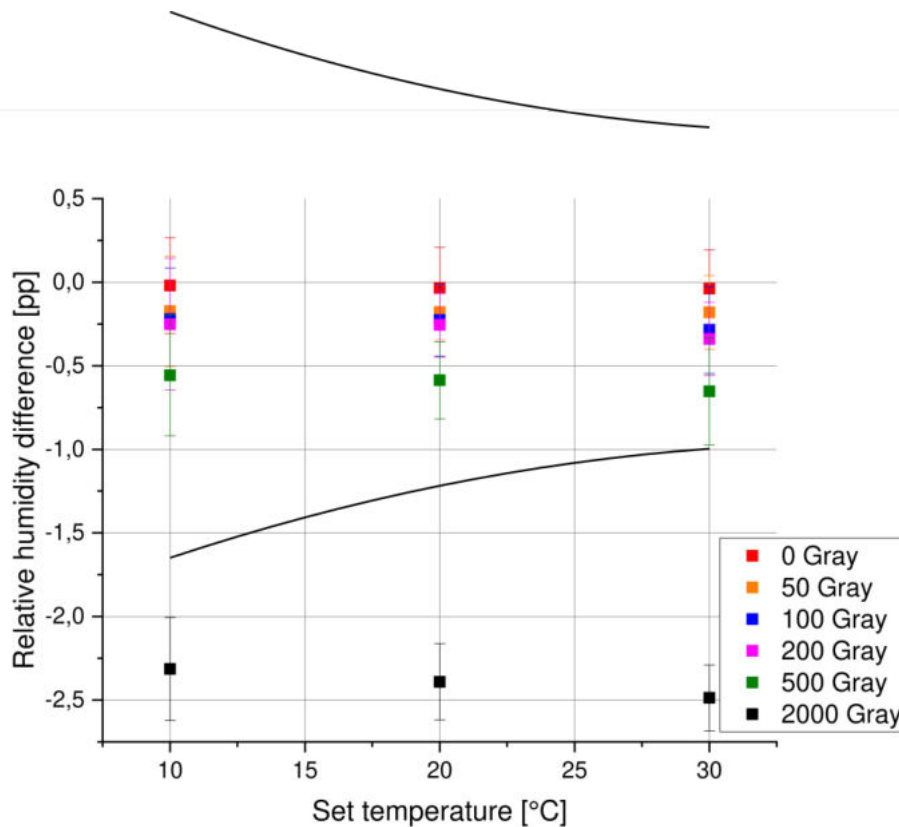


Figure 6.27: Relative humidity difference between reference sensor and test sensor (SHT21, channel 2) for $H = 50\%$; full irradiation plan (see table 5.3).

The difference of relative humidity (y-axis) in [pp] versus the set temperature (x-axis) in $^{\circ}\text{C}$ is plotted in figure 6.27. The difference of relative humidity was examined for three different temperatures. The error bars were calculated using the same formula 6.1 as for the temperature difference.

Even for small irradiation doses, a tendency can be recognized that the absolute differences increase with increasing dose. Due to the relatively large fluctuations of the entire system, it is not possible to make statement about whether this behavior is caused by irradiation.

For an accumulated dose of 2000 Gy, the differences of relative humidity are outside the limits. In addition, it can be seen that the absolute difference of relative humidity increase with increasing temperature at a fixed dose.

In the following the concerning graphs to the other test sensors can be seen in 6.28 and 6.29.

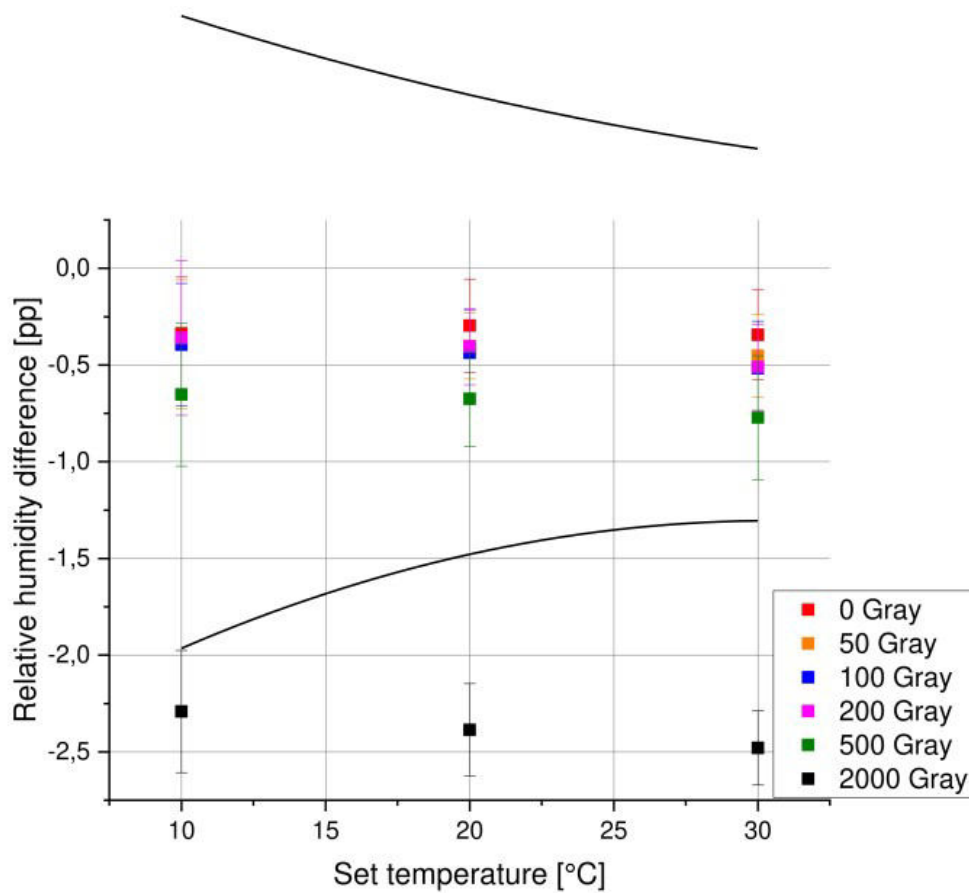


Figure 6.28: Relative humidity difference between reference sensor and test sensor (SHT21, channel 3) for $H = 50\%$; full irradiation plan (see table 5.3).

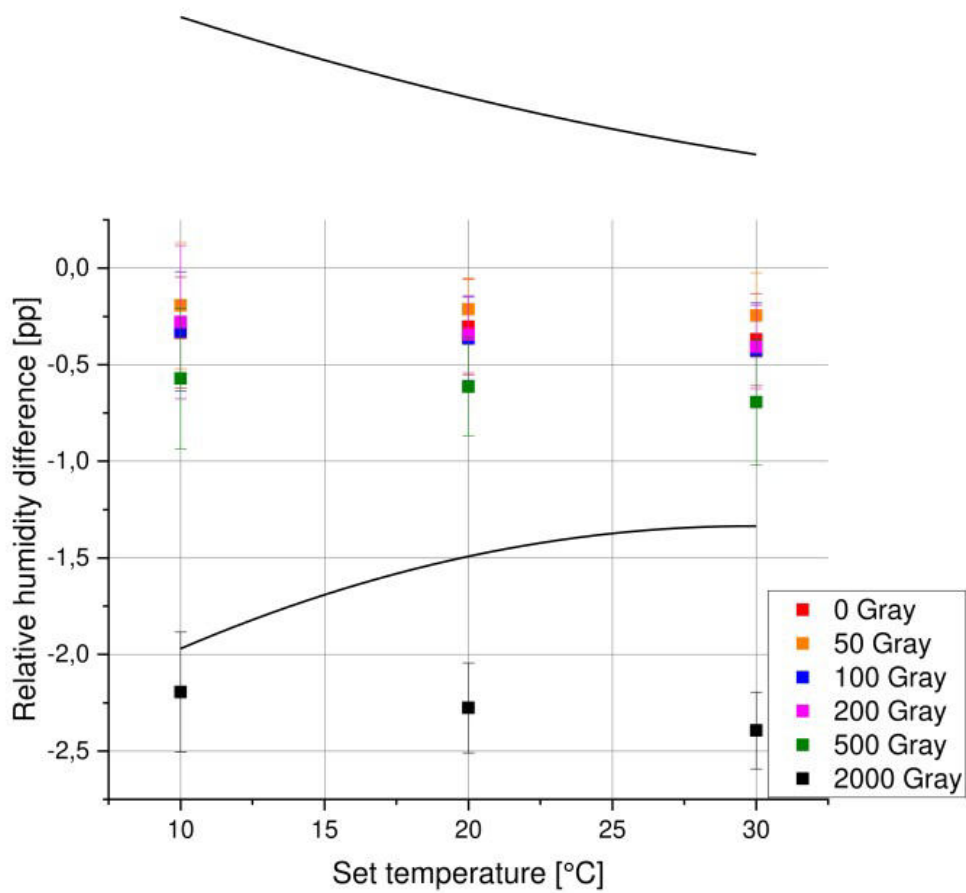


Figure 6.29: Relative humidity difference between reference sensor and test sensor (SHT21, channel 4) for $H = 50\%$; full irradiation plan (see table 5.3).

It can be seen that figs. 6.28 and 6.29 show a similar behavior as fig. 6.27, thus the different test sensor verify the described behavior to figure 6.27. However, this behavior differs for other target relative humidities. An example is shown for $H = 40\%$ in figure 6.30.

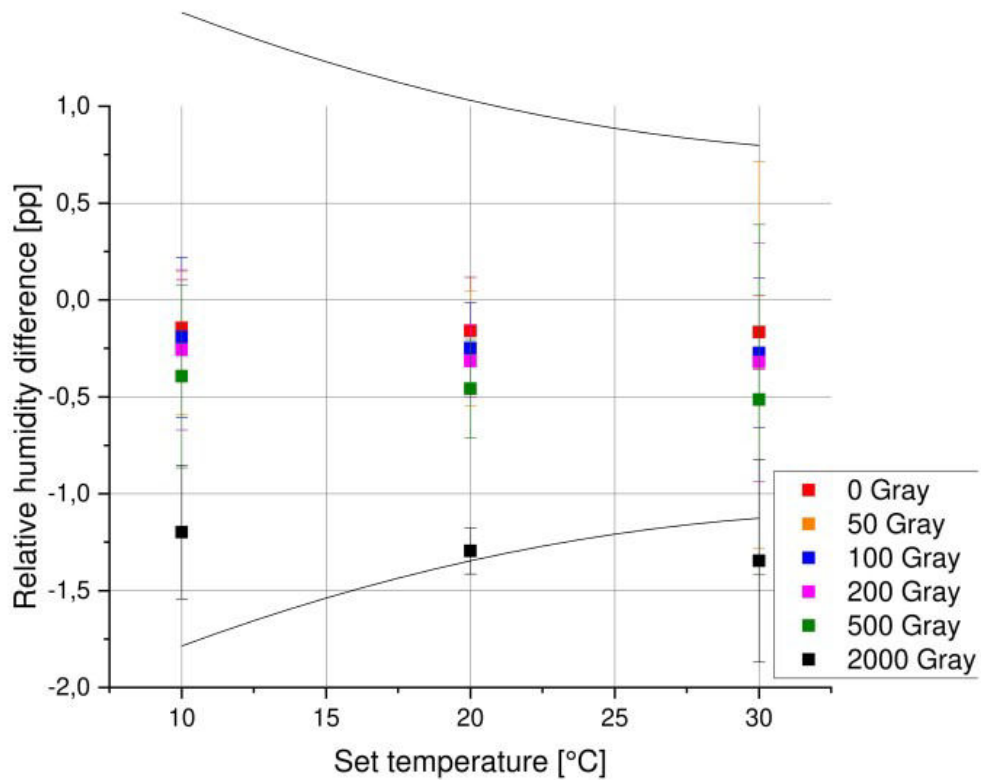


Figure 6.30: Relative humidity difference between reference sensor and test sensor (SHT21, channel 2) for $H = 40\%$; full irradiation plan (see table 5.3).

Due to the error bars of the differences, every difference is located within the boundaries of fluctuation. However, the absolute difference tends to increase with an increasing dose. In general, this behavior is verified by measurements at different humidities and test sensors.

It cannot be generalized that any difference of relative humidity is outside the limits of the tube. This is because the fluctuations of the entire system are very large. Afterwards the BME280 was examined with respect to the relative humidity.

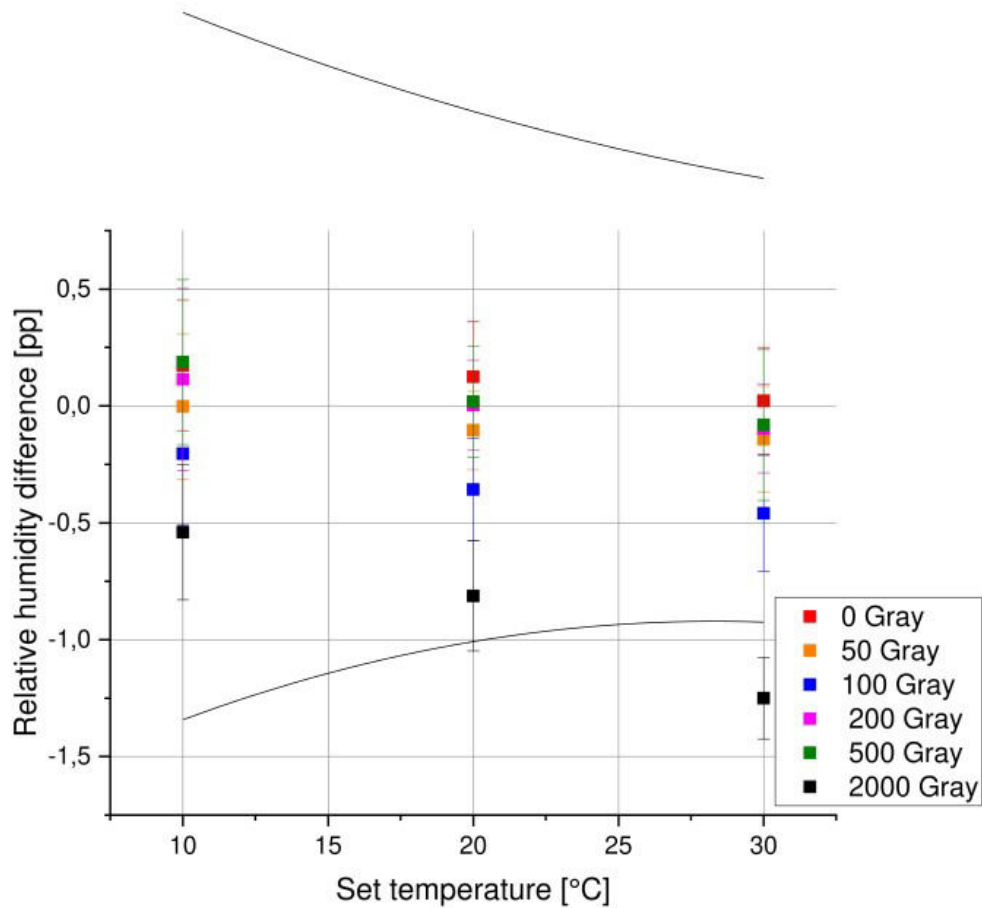


Figure 6.31: Relative humidity difference between reference sensor and test sensor (BME280, channel 3) for $H = 50\%$; full irradiation plan (see table 5.3).

Initially it looks as if the sensor shows a change with respect to relative humidity after irradiation with an accumulated dose of $D = 2000$ Gy. But that is not the case. For other relative humidities, it can be noted that the distribution of the differences is arbitrary. Illustrative this is shown in figure 6.32 for a relative humidity of $H = 45\%$.

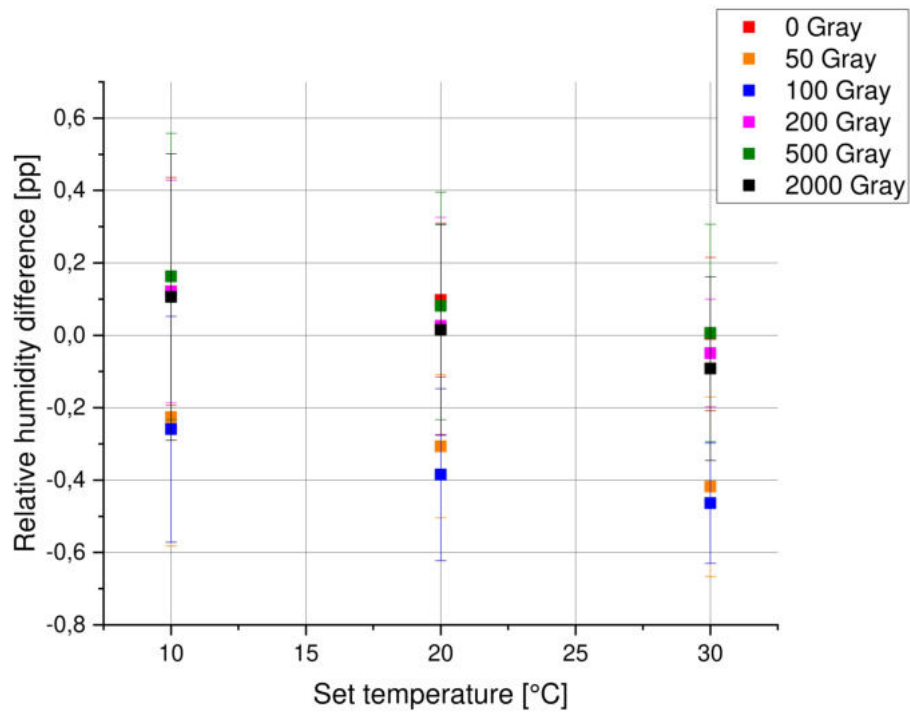


Figure 6.32: Relative humidity difference between reference sensor and test sensor (BME280, channel 3) for $H = 45\%$; full irradiation plan (see table 5.3); without boundary.

The described behavior is verified by other BME280 test sensors and different relative humidities.

Therefore the BME280 does not show a reaction to the irradiation with gamma-rays with respect to relative humidity.

7. Conclusion and Outlook

In the scope of this bachelor thesis, the radiation hardness of the environmental sensors of type SHT21 and BME280 was examined. Several test sensors of both types were irradiated and then tested in a climate chamber under fixed conditions with regard to temperature and relative humidity. A reference sensor of each type was located in the cabinet so that the change in the difference with respect to the measured temperature and moisture, between a reference sensor and a test sensor could be observed. For this procedure, the climate chamber was examined with respect to the achievement and the reproducibility of the set temperature and humidity.

Afterwards, all test sensors were irradiated with the same absorbed dose and were examined for different temperatures and relative humidities in the climate chamber. This was repeated for different doses.

Within the accuracies of the sensors, the set temperatures in the climate chamber were reached in good approximation. Due to missing accuracies of the relative humidity with respect to the climate chamber and the sensors, it is not possible to make a statement about the achievement of the values. The behavior of reproducibility with respect to the temperature was very good. The maximum distribution of the entire system was determined to ± 0.17 K for the SHT21 and ± 0.28 K for the BME280. For the relative humidity, it was observed that the reproducibility became worse with decreasing temperature. Among other things, this is because of the non-existent dew point which is necessary to reach the set humidity. The max. moisture distribution was determined to ± 1.64 % for the SHT21 and ± 1.52 % for the BME280.

During the measurements it could be observed that one of the BME280 sensors went into a non-responding state. It only reacts after a hard reset. After an operating time of 500 hours, the sensor failed completely. Furthermore, it was generally noticed that the moisture- and pressure measurement of the BME280 sensors at a temperature of $T = 0$ °C temporarily failed.

The SHT21 and the BME280 show a similar radiation hardness with respect to temperature measurement. From an accumulated dose of 500 Gy a tendency can be observed that both sensor types show a reaction to the irradiation. For 2000 Gy, a reaction can be determined with certainty. Moreover, it was observed that one of the SHT21 sensors reacts to irradiation at a temperature of -30 °C at an accumulated dose of 200 Gy. However, the other test sensors did not verify this behavior.

With respect to the relative humidity, a reaction can be seen from 2000 Gy for the SHT21. The BME280, shows no reaction at all to the irradiation with respect to the moisture measurement. In general, the behavior of both sensor types is verified by the test sensors of each type (except of one SHT21 at -30 °C.). In comparison, the PANDA barrel receives an annual dose of ≈ 30 Gy. Behind the crystals, almost no more photons should be available. Due to this, within the experimental lifetime of the experiment, the sensors will not receive the radiation dose, which is needed to seriously damage the

sensors.

It can be concluded that the BME280 and the SHT21 shows a good behavior in radiation hardness of the temperature and humidity measurement. Even for relative humidity, the BME280 shows no reaction at all.

With regard to the complete outage of the BME280, this sensor types should be checked before usage to ensure their functionality. Furthermore, the investigation to radiation hardness with respect to the relative humidity should be repeated with a better dew point so that the values will be reached better and the fluctuation of the entire system decrease.

At least, it is necessary to investigate the sensors with respect to charged particles, or neutrons because these particles are not stopped in the electromagnetic calorimeter.

8. Appendix

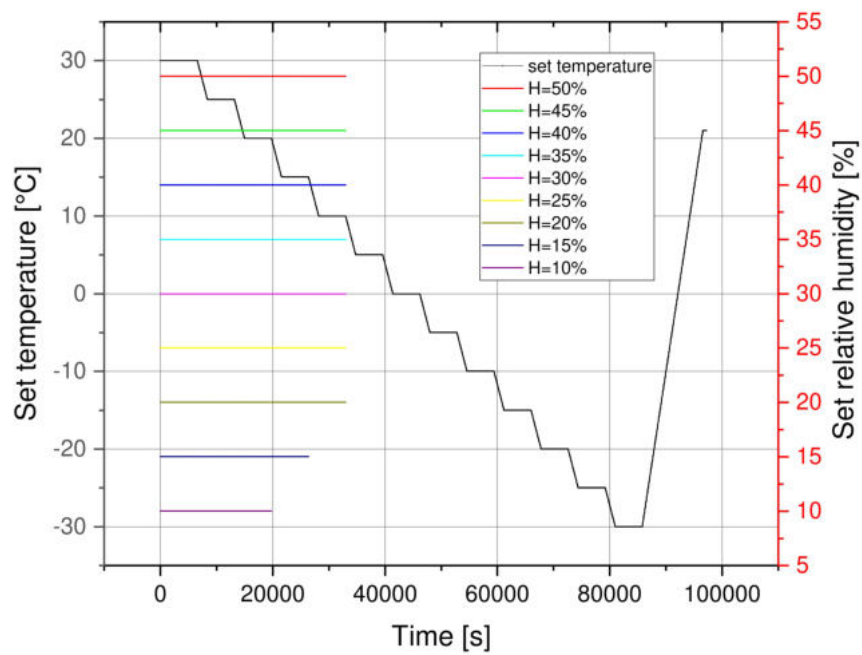


Figure 8.1: Overview of the different programs with constant relative humidity.

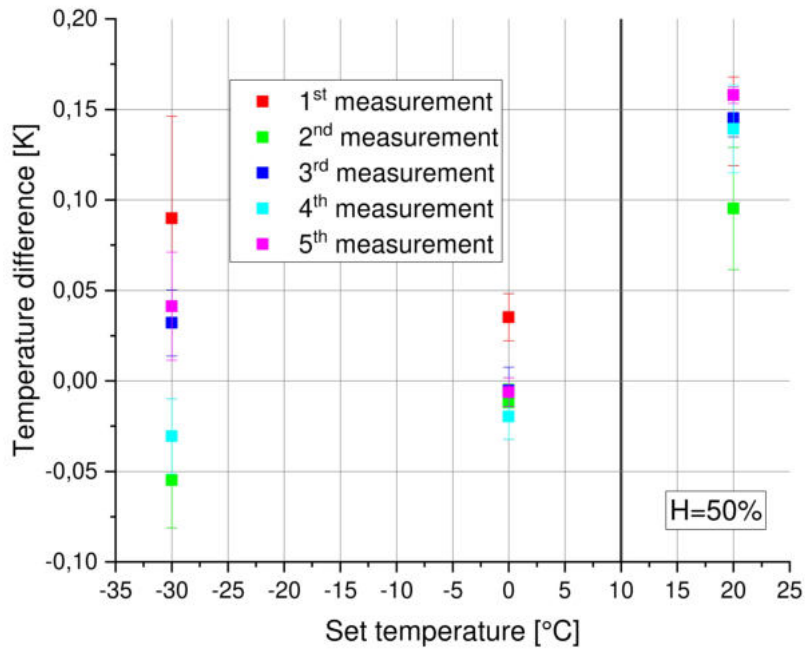


Figure 8.2: Temperature difference at $H = 50\%$ for SHT21. Vertical line: edge of area 2 in the climate state diagram 5.6.

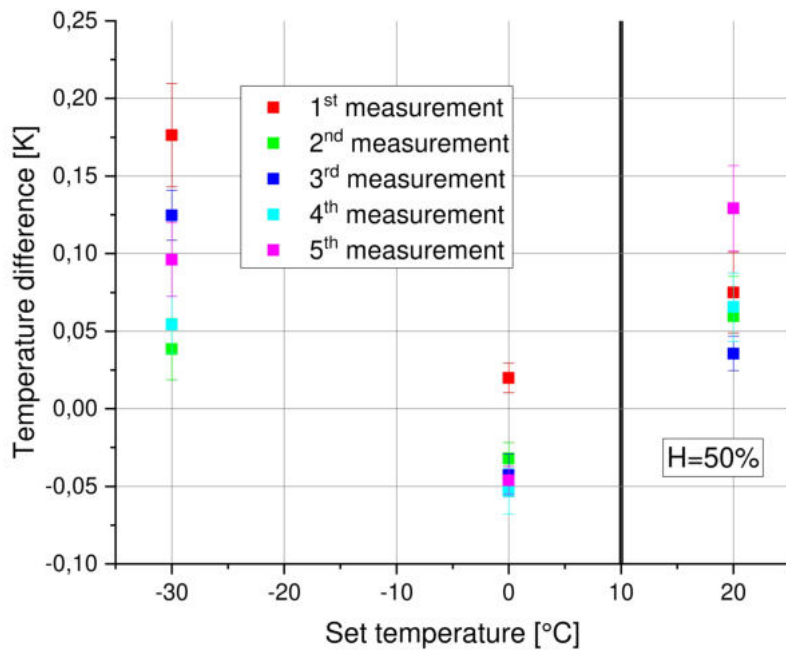


Figure 8.3: Temperature difference at $H = 50\%$ for BME280. Vertical line: edge of area 2 in the climate state diagram 5.6.

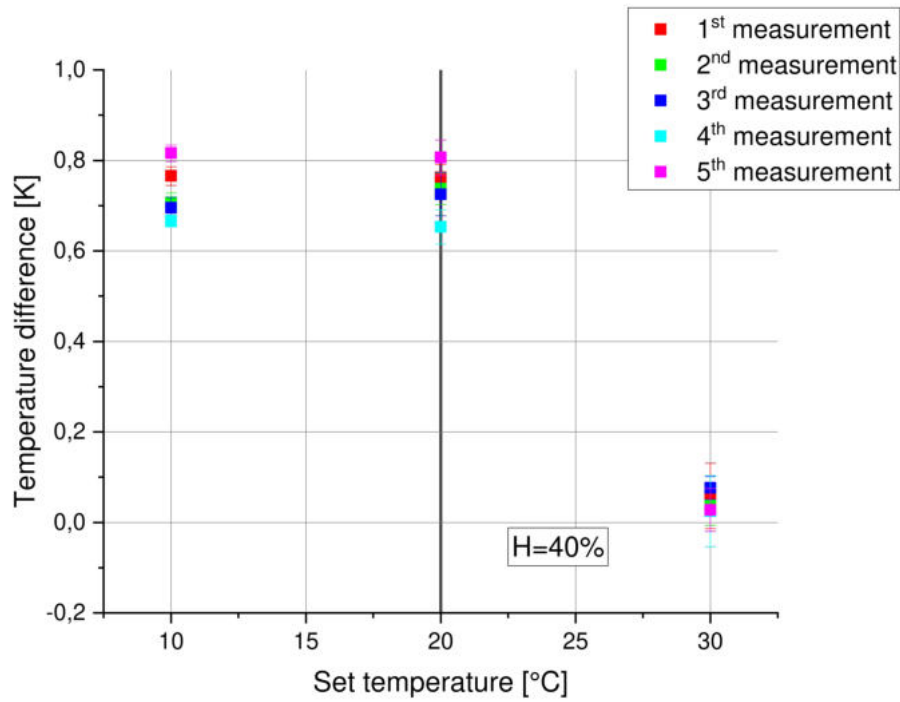


Figure 8.4: Temperature difference at $H = 40\%$ for SHT21. Vertical line: edge of area 2 in the climate state diagram 5.6.

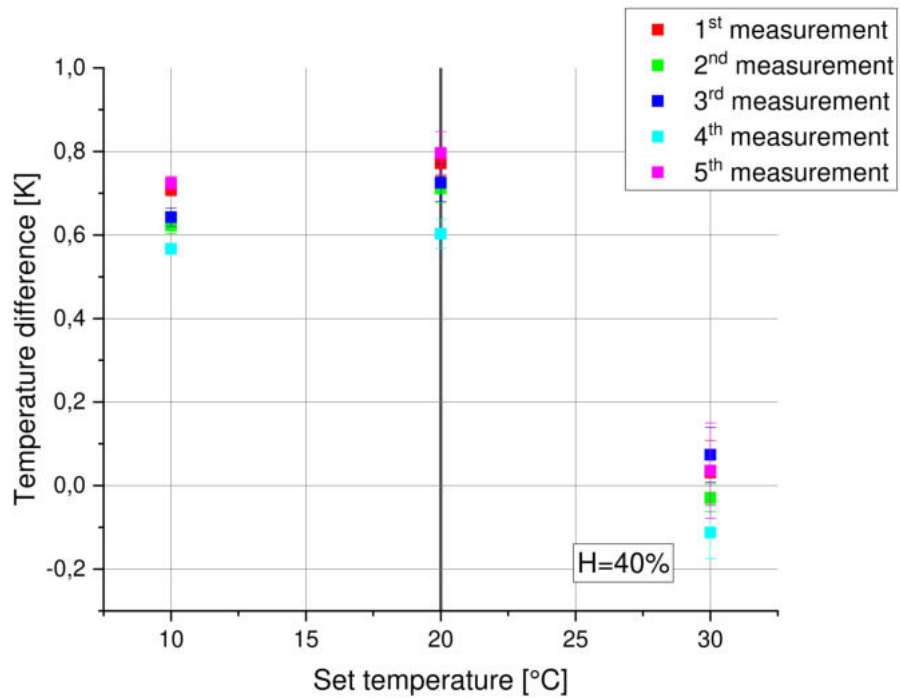


Figure 8.5: Temperature difference at $H = 40\%$ for BME280. Vertical line: edge of area 2 in the climate state diagram 5.6.

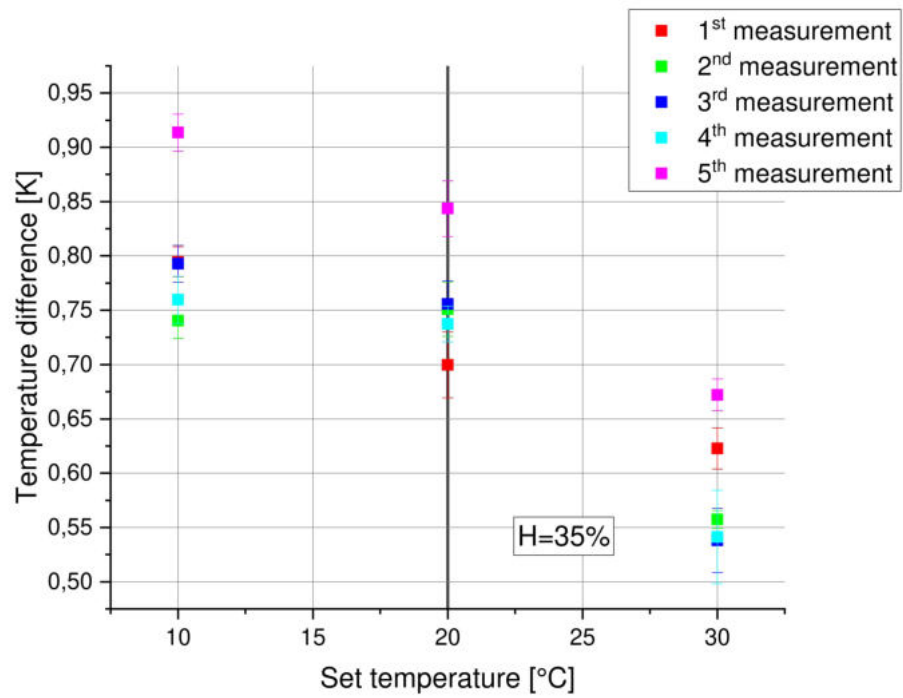


Figure 8.6: Temperature difference at $H = 35\%$ for SHT21. Vertical line: edge of area 2 in the climate state diagram 5.6.

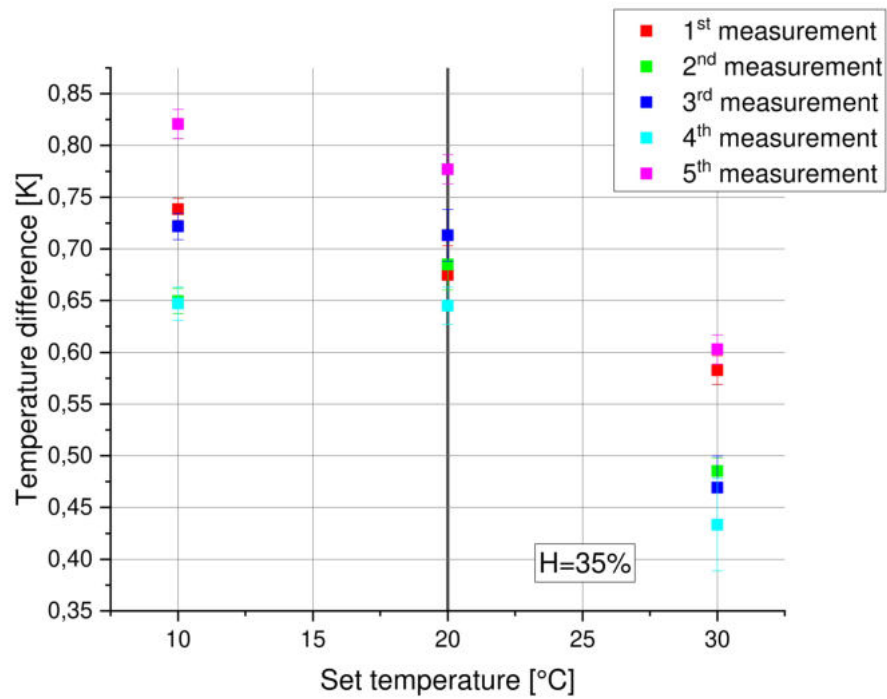


Figure 8.7: Temperature difference at $H = 35\%$ for BME280. Vertical line: edge of area 2 in the climate state diagram 5.6.

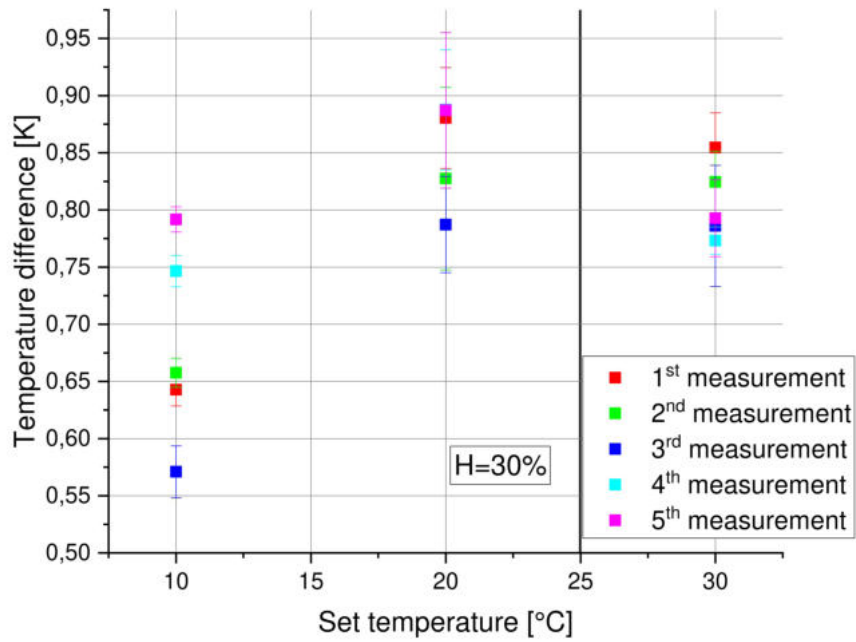


Figure 8.8: Temperature difference at $H = 30\%$ for SHT21. Vertical line: edge of area 2 in the climate state diagram 5.6.

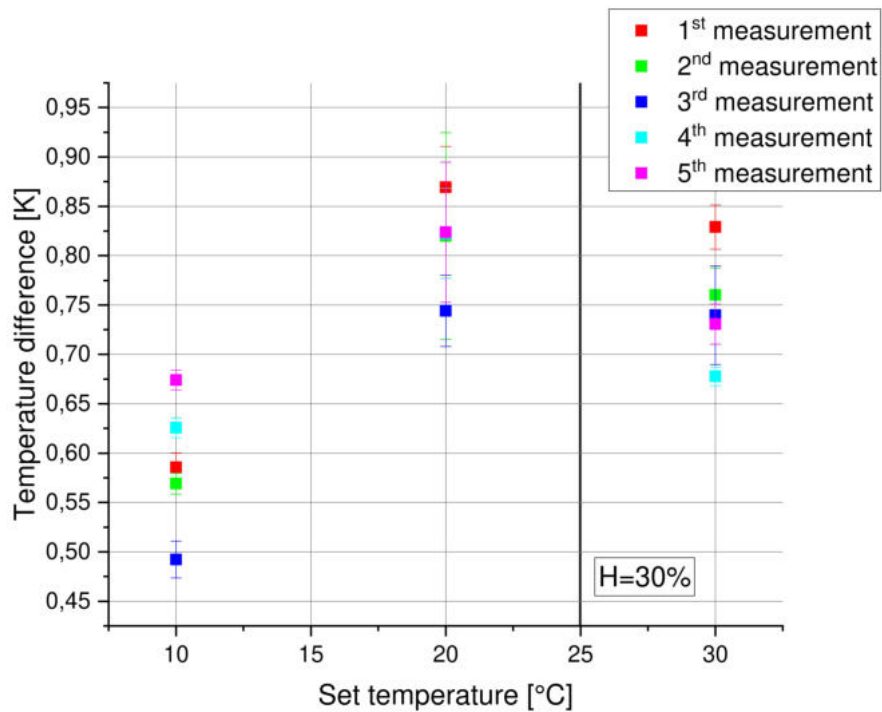


Figure 8.9: Temperature difference at $H = 30\%$ for BME280. Vertical line: edge of area 2 in the climate state diagram 5.6.

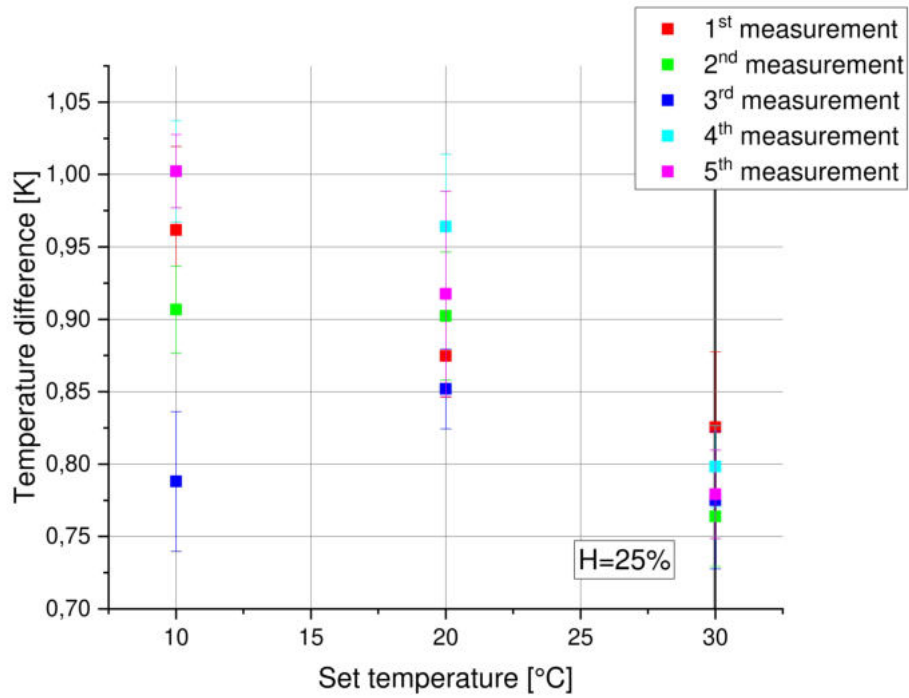


Figure 8.10: Temperature difference at $H = 25\%$ for SHT21. Vertical line: edge of area 2 in the climate state diagram 5.6.

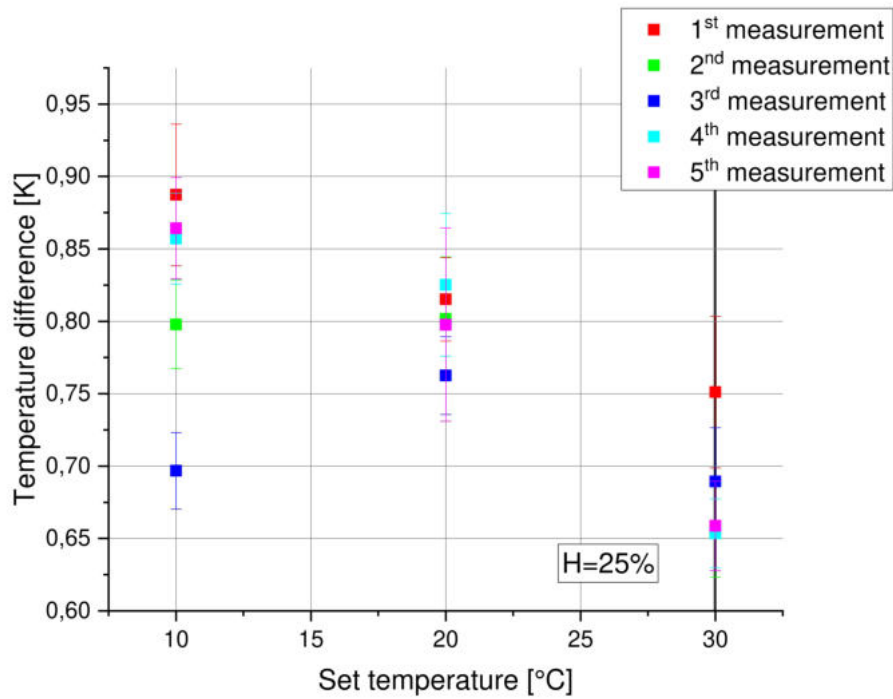


Figure 8.11: Temperature difference at $H = 25\%$ for BME280. Vertical line: edge of area 2 in the climate state diagram 5.6.

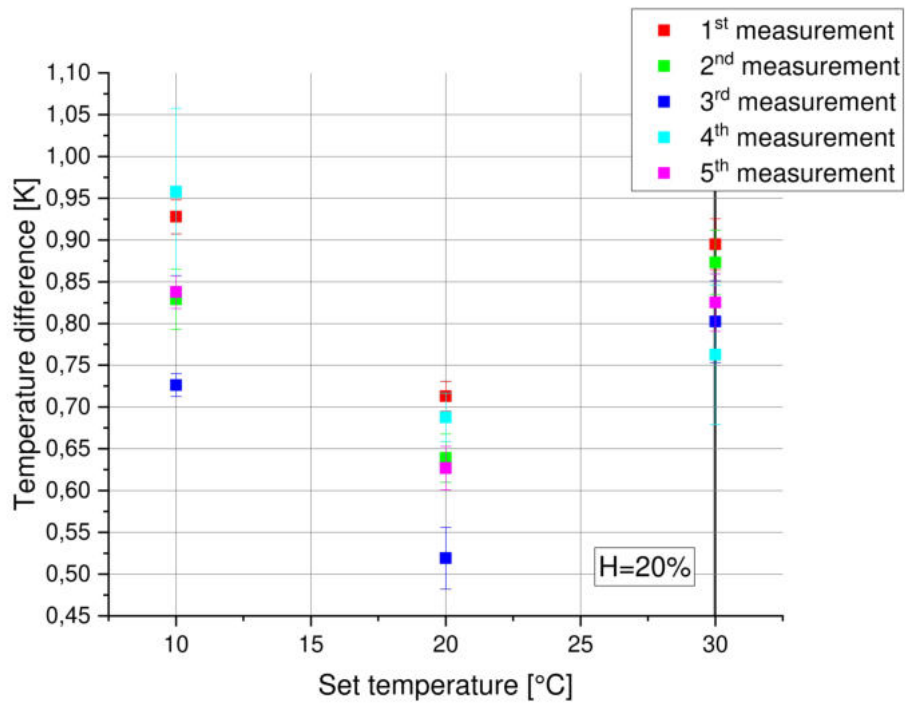


Figure 8.12: Temperature difference at $H = 20\%$ for SHT21. Vertical line: edge of area 2 in the climate state diagram 5.6.

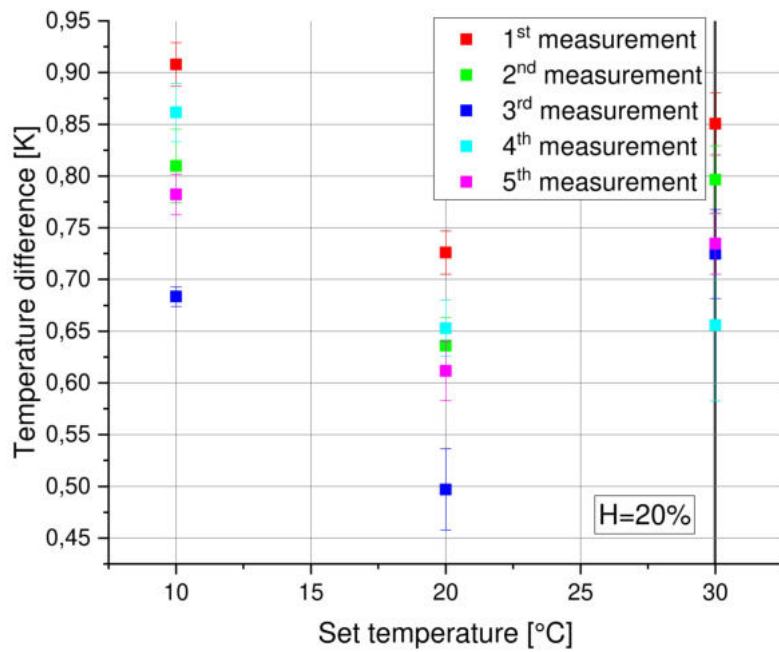


Figure 8.13: Temperature difference at $H = 20\%$ for BME280. Vertical line: edge of area 2 in the climate state diagram 5.6.

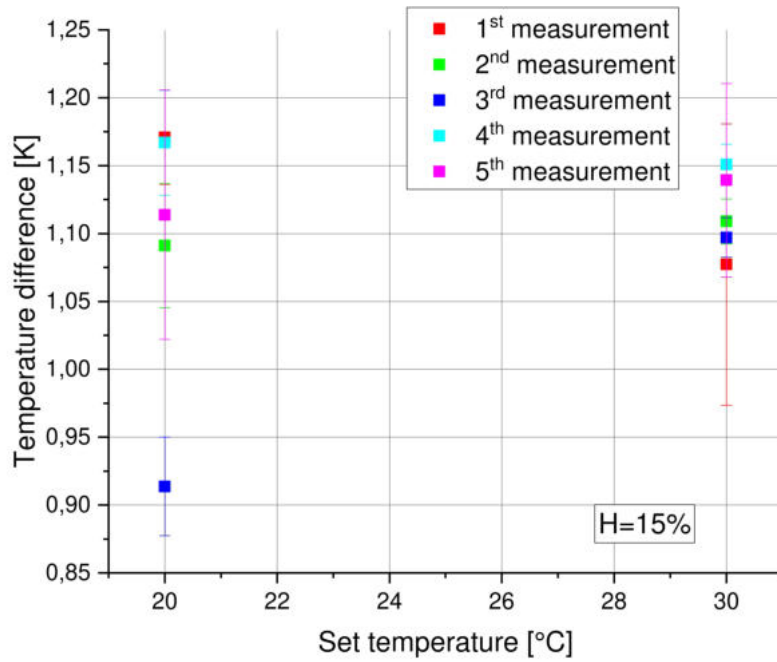


Figure 8.14: Temperature difference at $H = 15\%$ for SHT21.

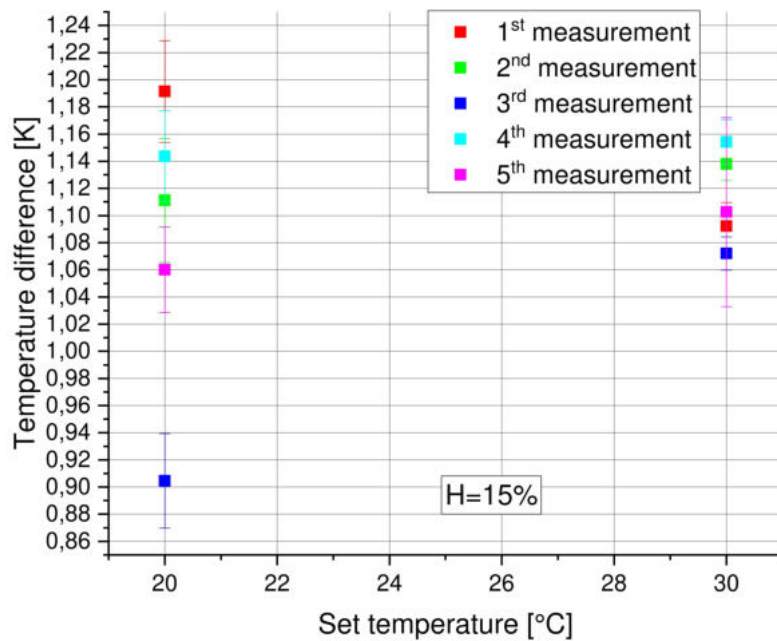


Figure 8.15: Temperature difference at $H = 15\%$ for BME280.

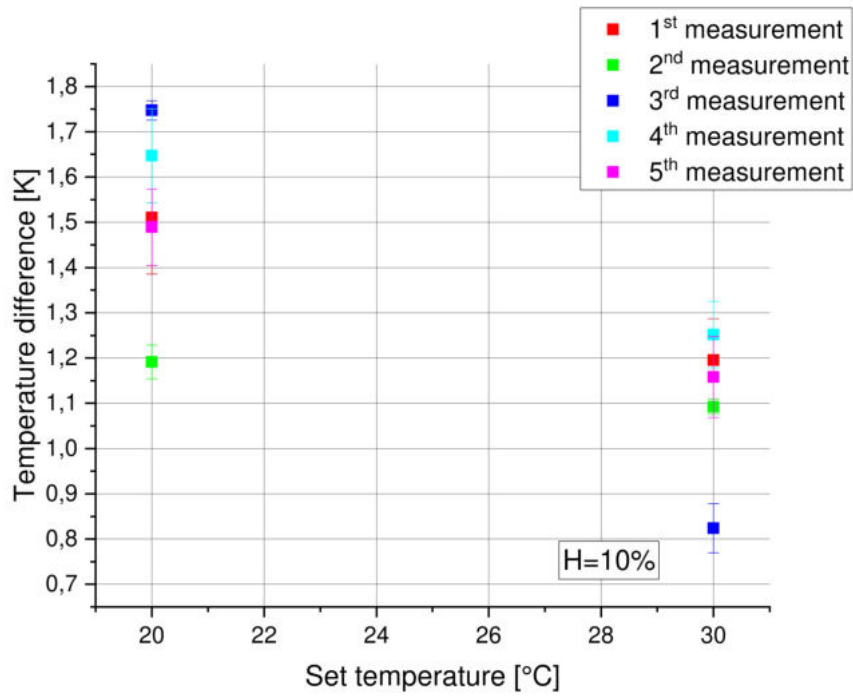


Figure 8.16: Temperature difference at $H = 10\%$ for BME280..

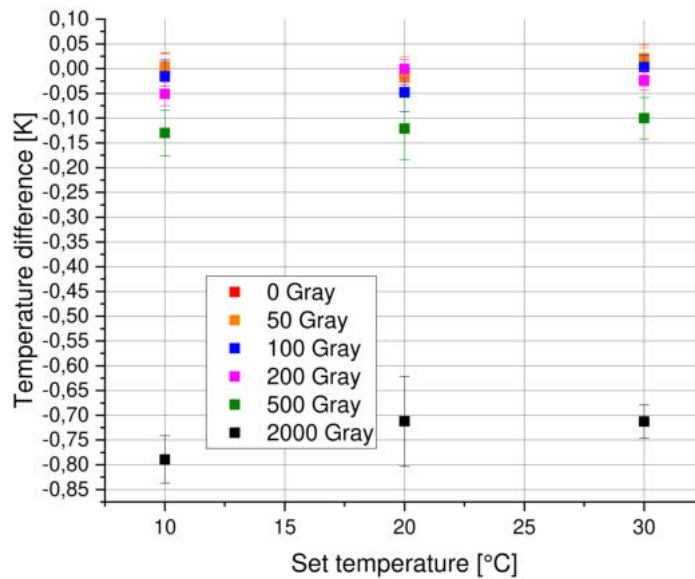


Figure 8.17: Temperature difference between reference sensor and test sensor (SHT21, channel 2) for $H = 45\%$; full irradiation plan (see table 5.3).

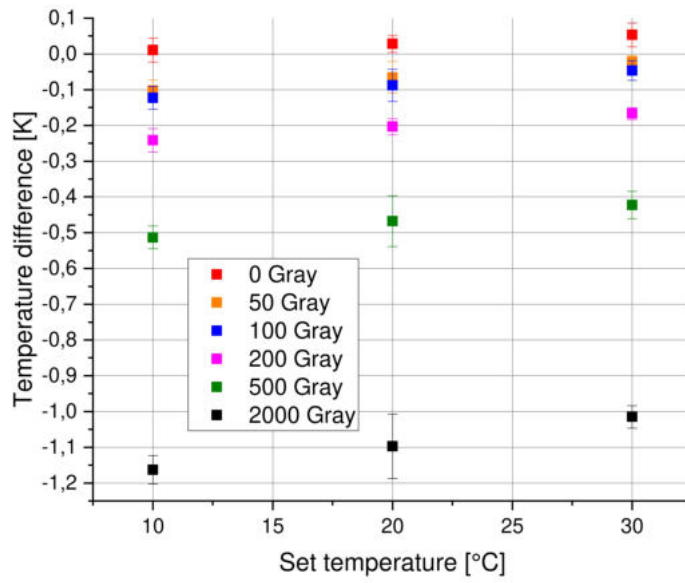


Figure 8.18: Temperature difference between reference sensor and test sensor (BME280, channel 3) for $H = 45\%$; full irradiation plan (see table 5.3).

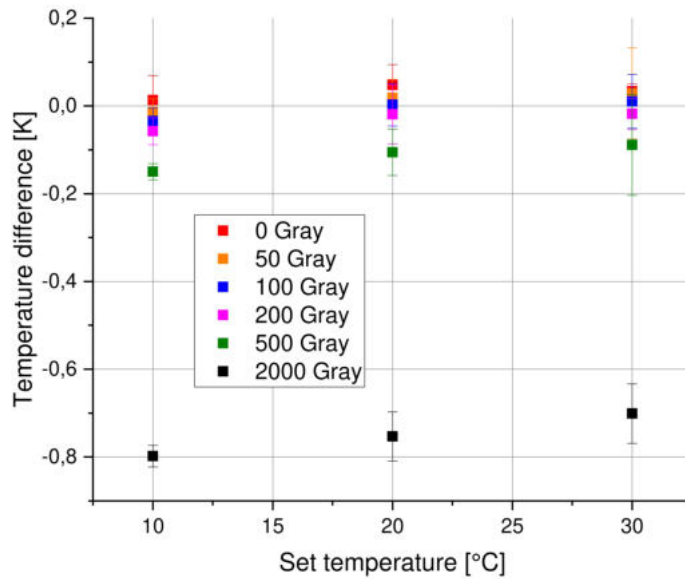


Figure 8.19: Temperature difference between reference sensor and test sensor (SHT21, channel 2) for $H = 40\%$; full irradiation plan (see table 5.3).

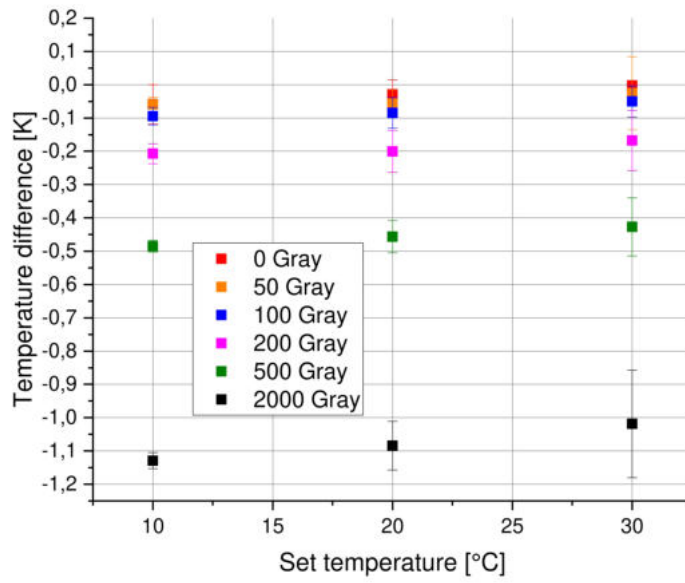


Figure 8.20: Temperature difference between reference sensor and test sensor (BME280, channel 3) for $H = 40\%$; full irradiation plan (see table 5.3).

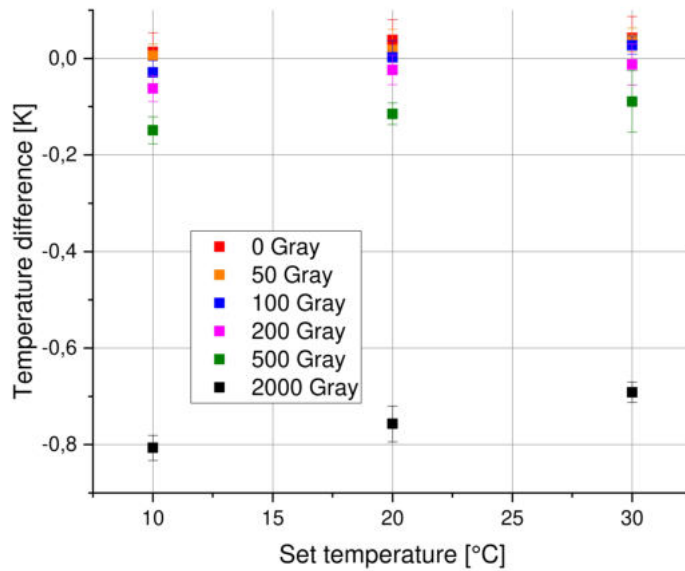


Figure 8.21: Temperature difference between reference sensor and test sensor (SHT21, channel 2) for $H = 35\%$; full irradiation plan (see table 5.3).

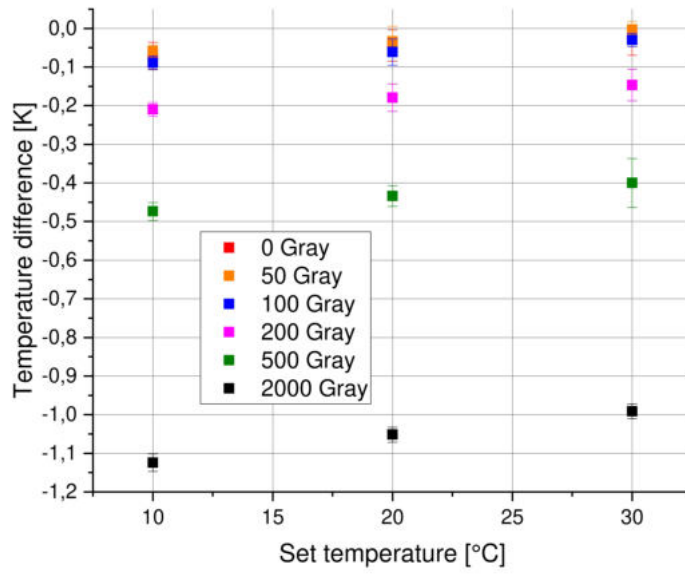


Figure 8.22: Temperature difference between reference sensor and test sensor (BME280, channel 3) for $H = 35\%$; full irradiation plan (see table 5.3).

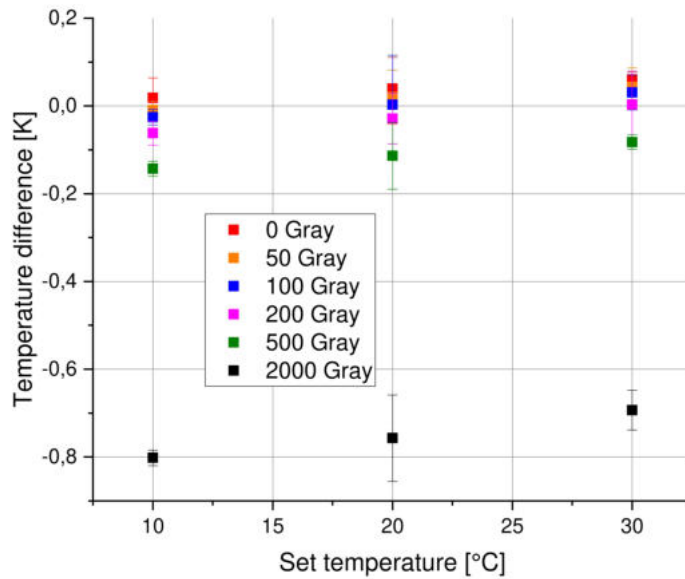


Figure 8.23: Temperature difference between reference sensor and test sensor (SHT21, channel 2) for $H = 30\%$; full irradiation plan (see table 5.3).

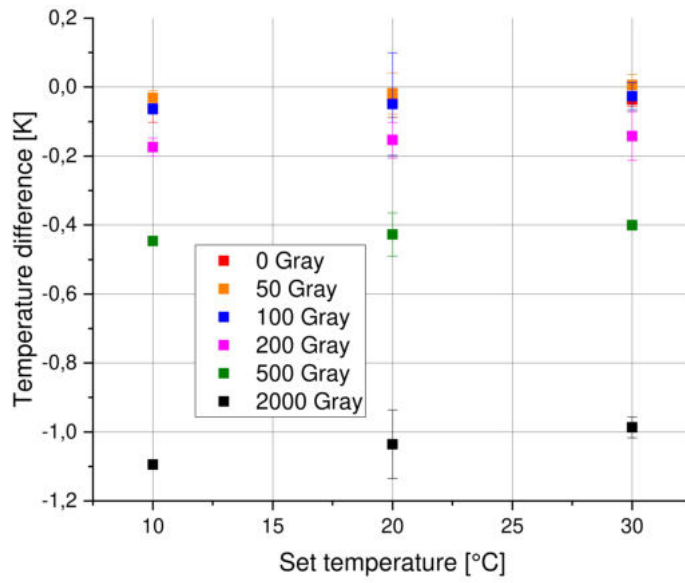


Figure 8.24: Temperature difference between reference sensor and test sensor (BME280, channel 3) for $H = 30\%$; full irradiation plan (see table 5.3).

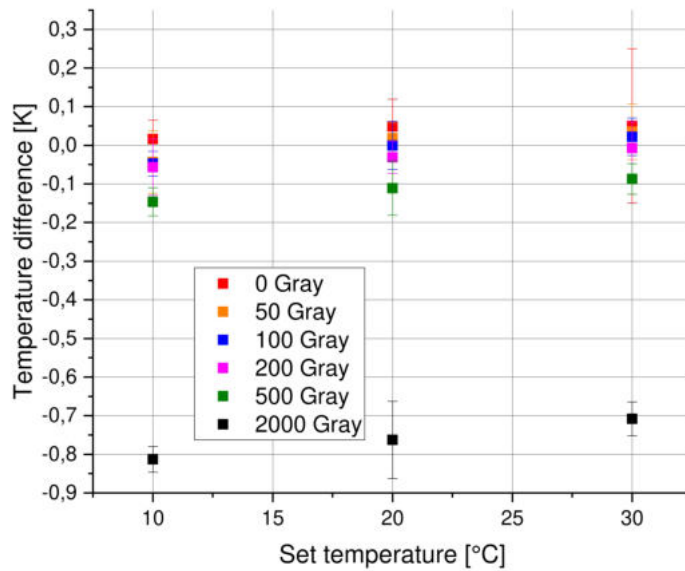


Figure 8.25: Temperature difference between reference sensor and test sensor (SHT21, channel 2) for $H = 25\%$; full irradiation plan (see table 5.3).

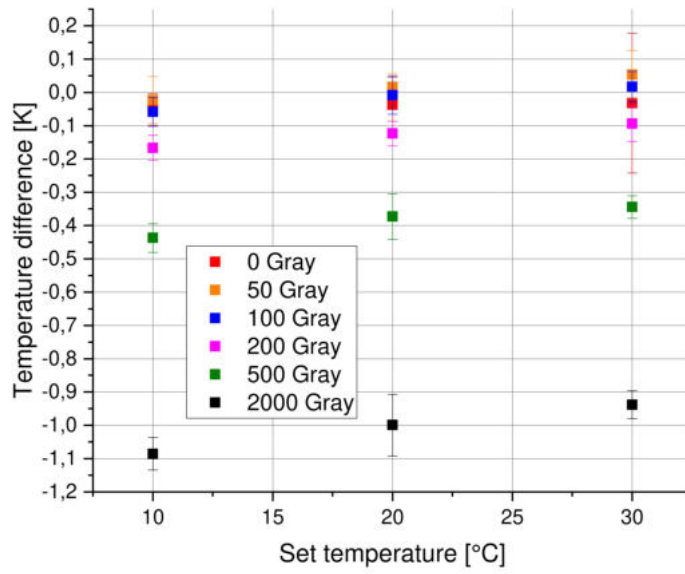


Figure 8.26: Temperature difference between reference sensor and test sensor (BME280, channel 3) for $H = 25\%$; full irradiation plan (see table 5.3).

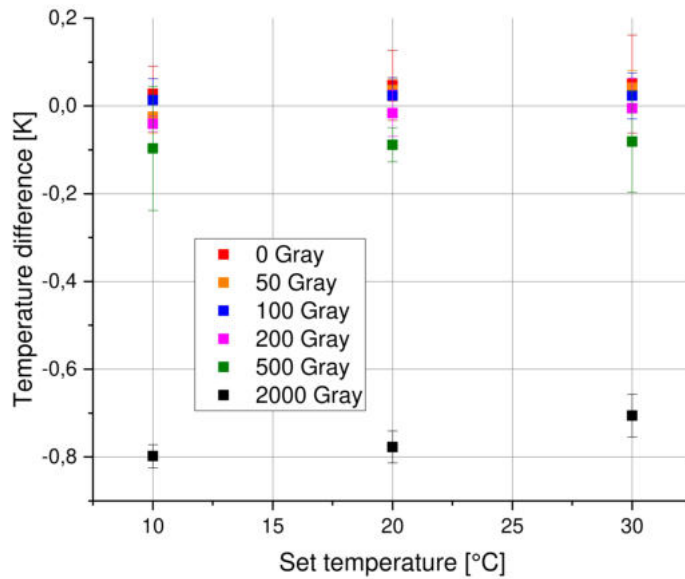


Figure 8.27: Temperature difference between reference sensor and test sensor (SHT21, channel 2) for $H = 20\%$; full irradiation plan (see table 5.3).

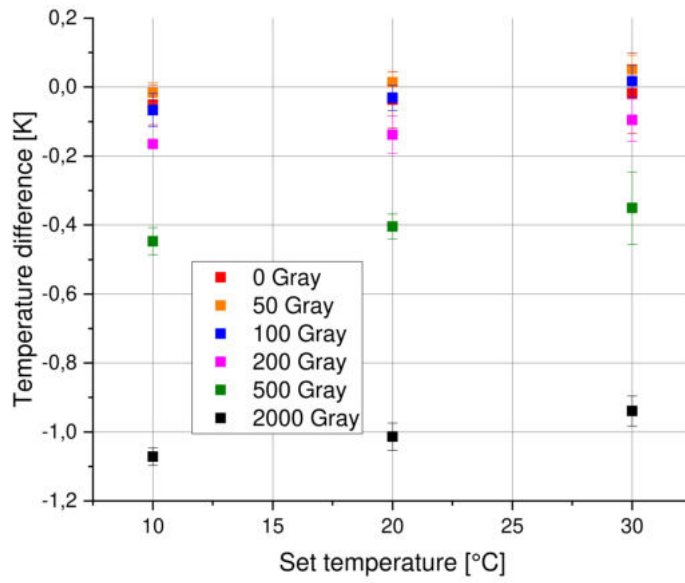


Figure 8.28: Temperature difference between reference sensor and test sensor (BME280, channel 3) for $H = 20\%$; full irradiation plan (see table 5.3).

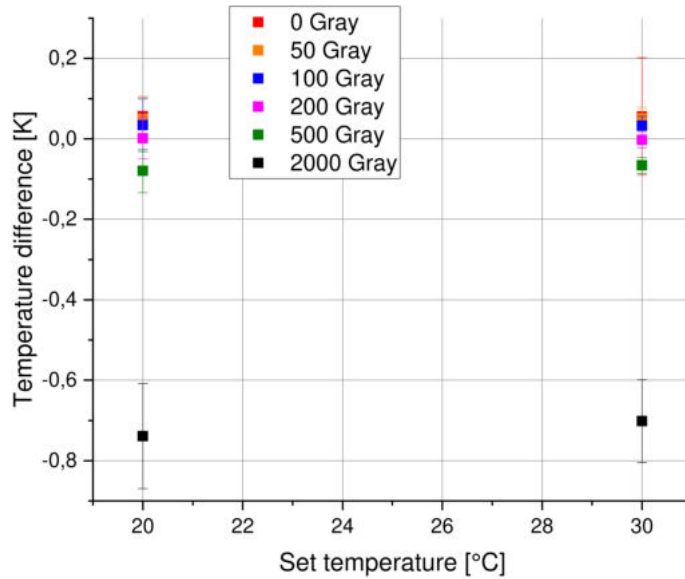


Figure 8.29: Temperature difference between reference sensor and test sensor (SHT21, channel 2) for $H = 15\%$; full irradiation plan (see table 5.3).

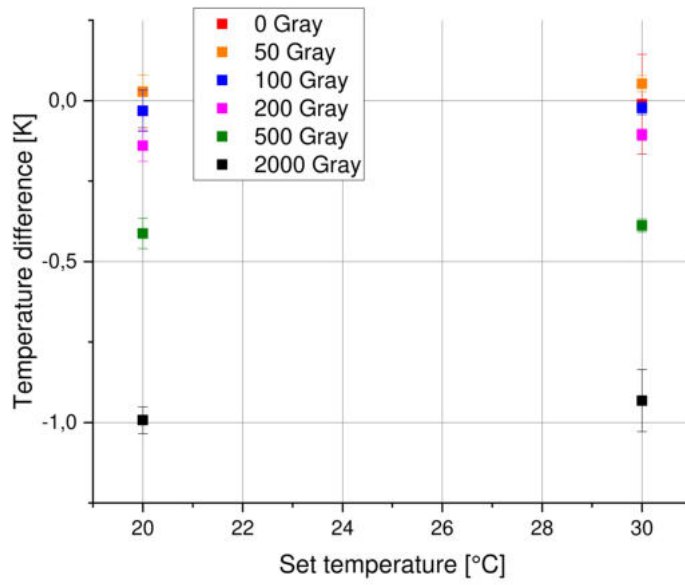


Figure 8.30: Temperature difference between reference sensor and test sensor (BME280, channel 3) for $H = 15\%$; full irradiation plan (see table 5.3).

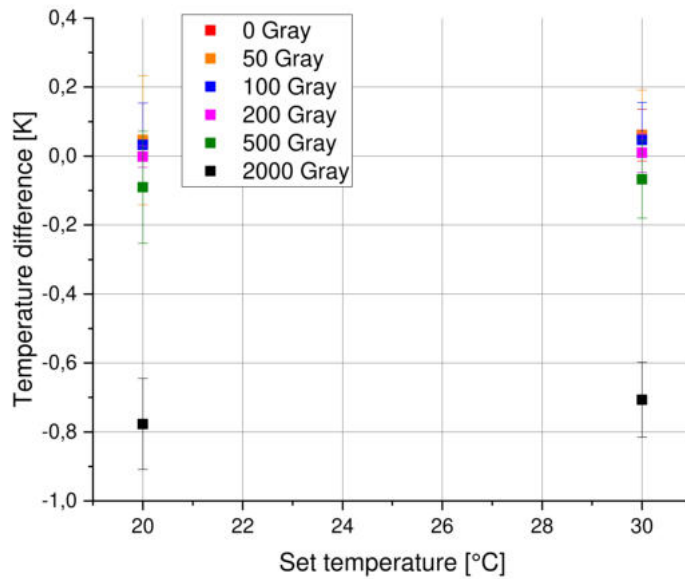


Figure 8.31: Temperature difference between reference sensor and test sensor (SHT21, channel 2) for $H = 10\%$; full irradiation plan (see table 5.3).

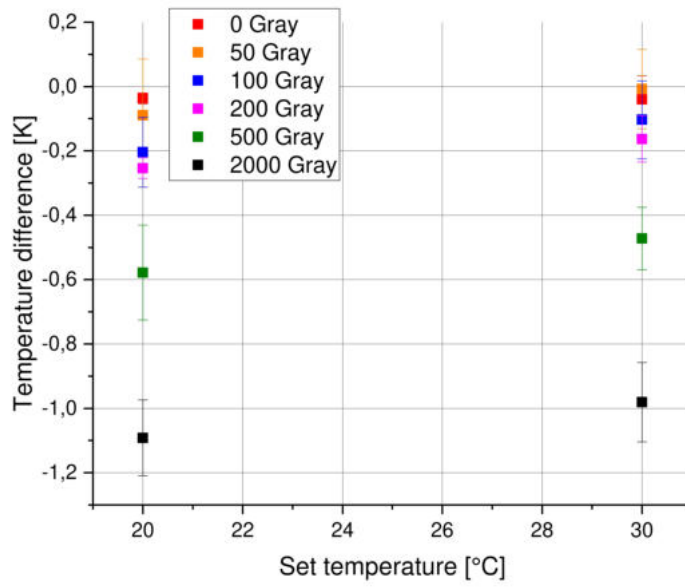


Figure 8.32: Temperature difference between reference sensor and test sensor (BME280, channel 3) for $H = 10\%$; full irradiation plan (see table 5.3).

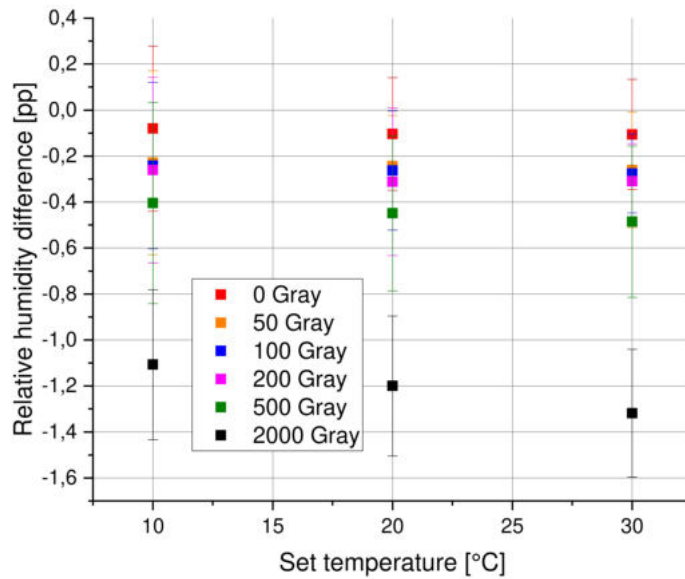


Figure 8.33: Relative humidity difference between reference sensor and test sensor (SHT21, channel 2) for $H = 45\%$; full irradiation plan (see table 5.3).

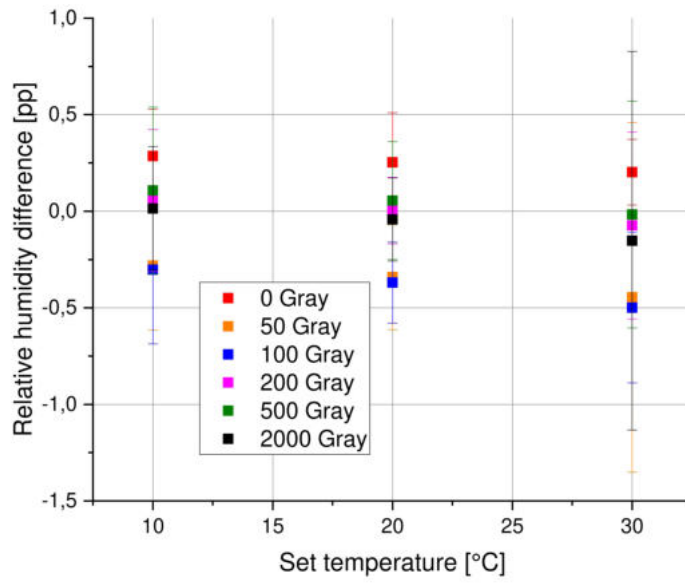


Figure 8.34: Relative humidity difference between reference sensor and test sensor (BME280, channel 3) for $H = 40\%$; full irradiation plan (see table 5.3).

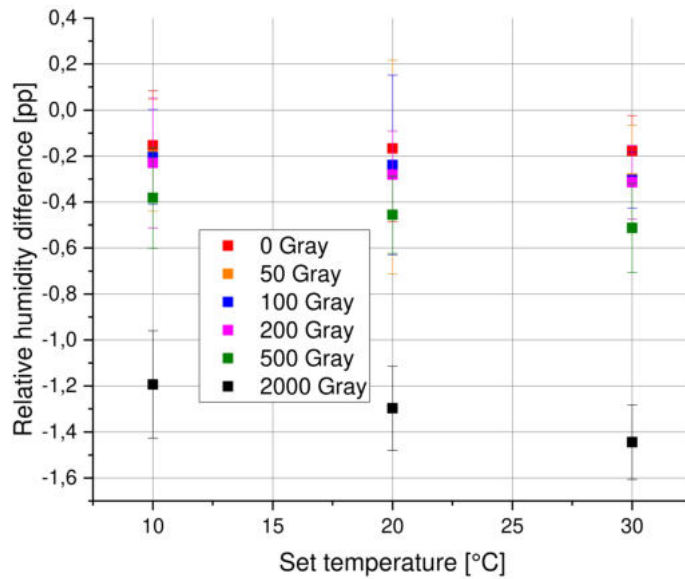


Figure 8.35: Relative humidity difference between reference sensor and test sensor (SHT21, channel 2) for $H = 35\%$; full irradiation plan (see table 5.3).

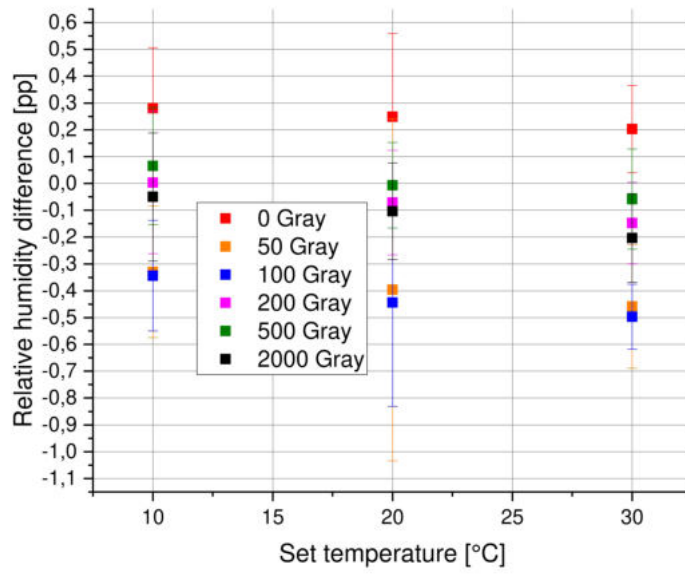


Figure 8.36: Relative humidity difference between reference sensor and test sensor (BME280, channel 3) for $H = 35\%$; full irradiation plan (see table 5.3).

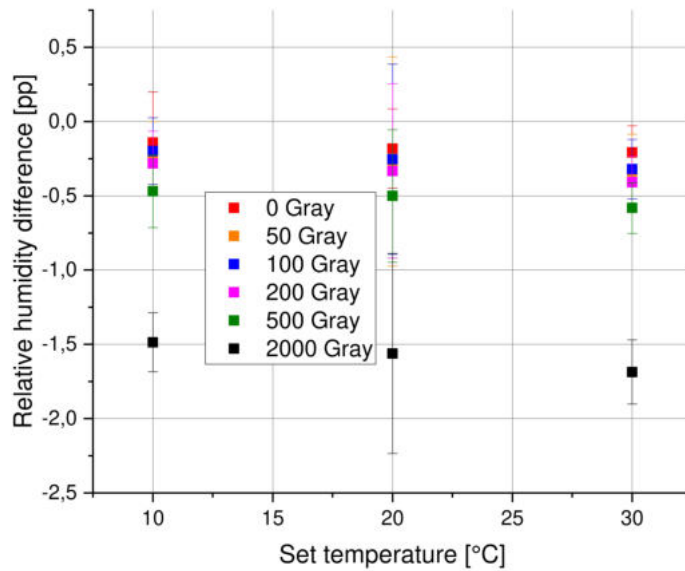


Figure 8.37: Relative humidity difference between reference sensor and test sensor (SHT21, channel 2) for $H = 30\%$; full irradiation plan (see table 5.3).

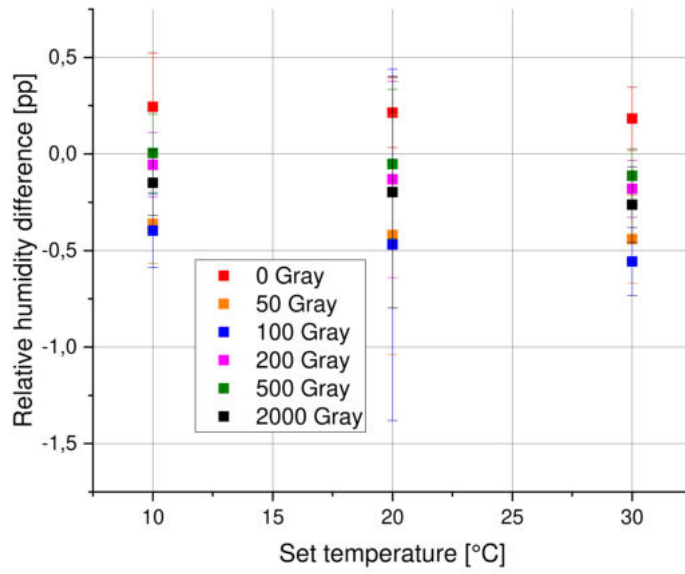


Figure 8.38: Relative humidity difference between reference sensor and test sensor (BME280, channel 3) for $H = 30\%$; full irradiation plan (see table 5.3).

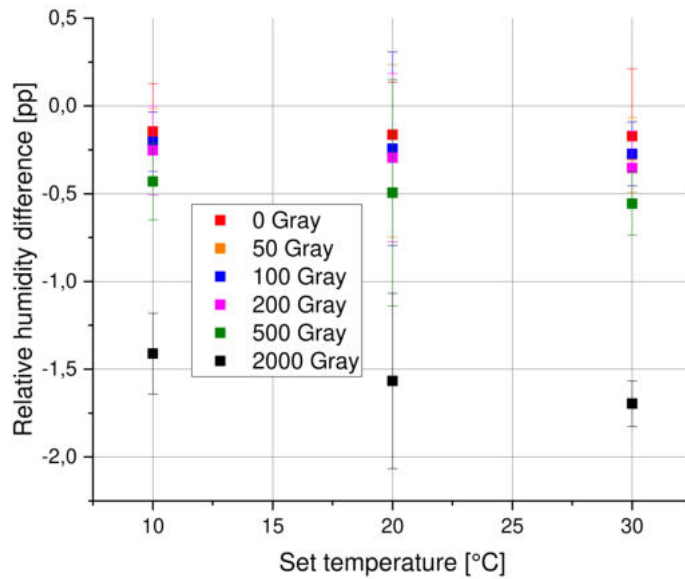


Figure 8.39: Relative humidity difference between reference sensor and test sensor (SHT21, channel 2) for $H = 25\%$; full irradiation plan (see table 5.3).

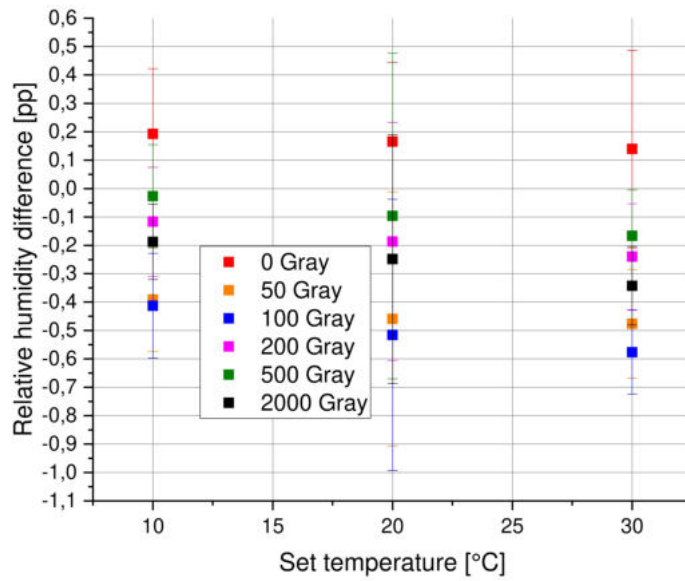


Figure 8.40: Relative humidity difference between reference sensor and test sensor (BME280, channel 3) for $H = 25\%$; full irradiation plan (see table 5.3).

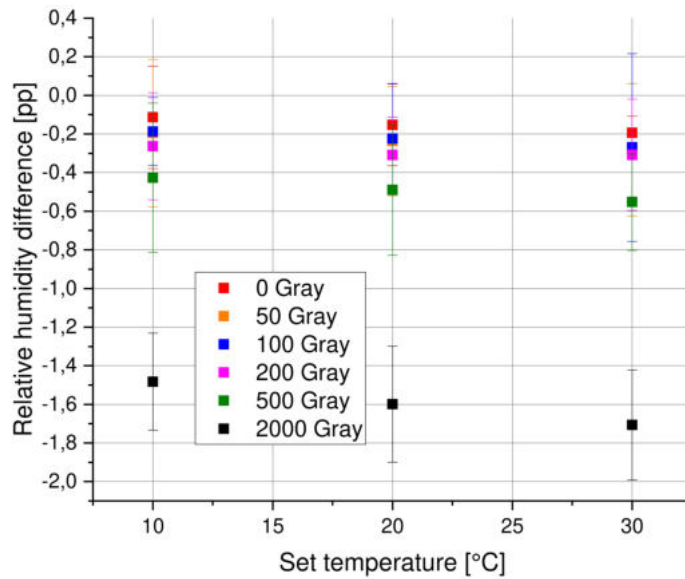


Figure 8.41: Relative humidity difference between reference sensor and test sensor (SHT21, channel 2) for $H = 20\%$; full irradiation plan (see table 5.3).

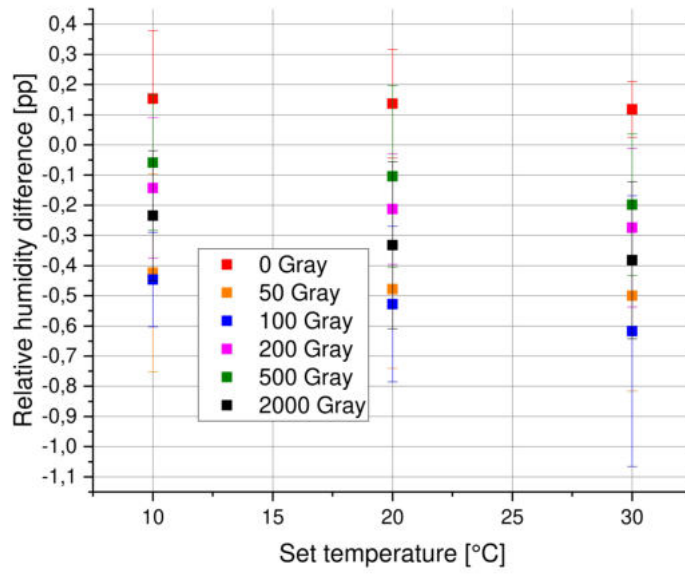


Figure 8.42: Relative humidity difference between reference sensor and test sensor (BME280, channel 3) for $H = 20\%$; full irradiation plan (see table 5.3).

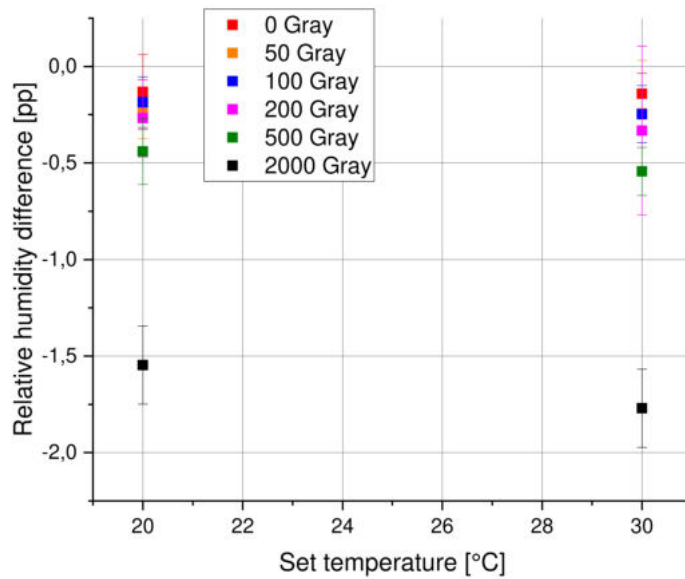


Figure 8.43: Relative humidity difference between reference sensor and test sensor (SHT21, channel 2) for $H = 15\%$; full irradiation plan (see table 5.3).

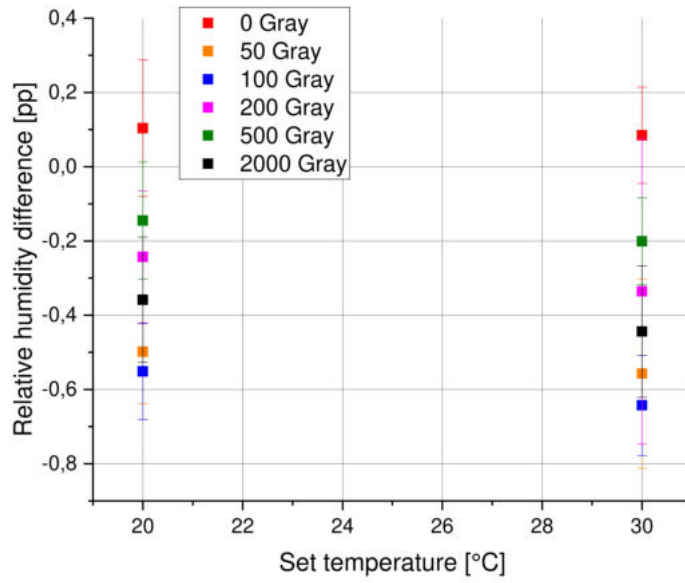


Figure 8.44: Relative humidity difference between reference sensor and test sensor (BME280, channel 3) for $H = 15\%$; full irradiation plan (see table 5.3).

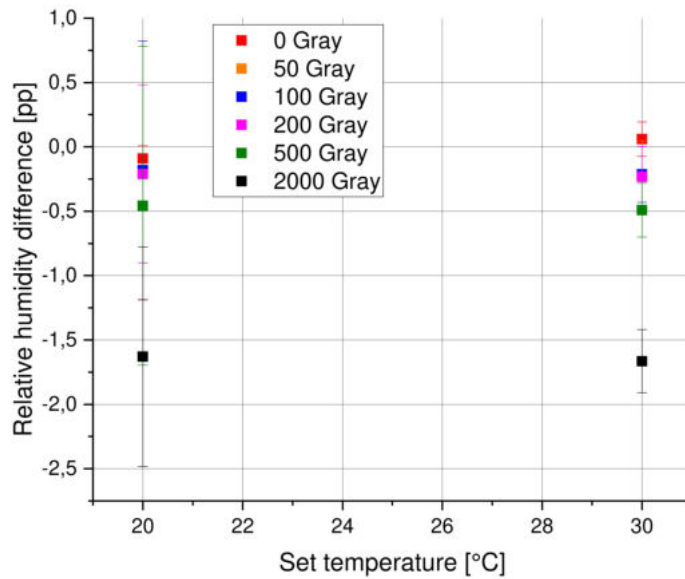


Figure 8.45: Relative humidity difference between reference sensor and test sensor (SHT21, channel 2) for $H = 10\%$; full irradiation plan (see table 5.3).

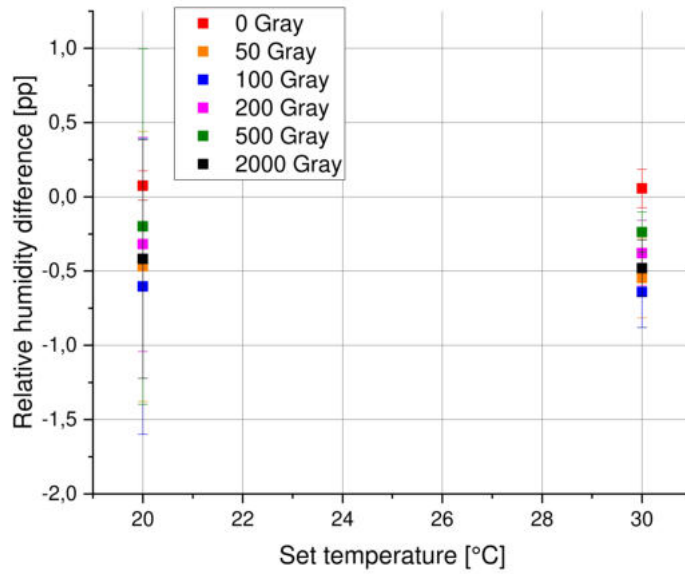


Figure 8.46: Relative humidity difference between reference sensor and test sensor (BME280, channel 3) for $H = 10\%$; full irradiation plan (see table 5.3).

Number	1	2	3	4	5
Name	3V3	5V	SDA	5V	SCL
Number	6	7	8	9	10
Name	GND	GPIO4	UART0_TXD	GND	UART0_RXD
Number	11	12	13	14	15
Name	GPIO17	PCM_CLK	GPIO27	GND	GPIO22
Number	16	17	18	19	20
Name	GPIO23	3V3	GPIO24	SPI0_MOSI	GND
Number	21	22	23	24	25
Name	SPI0_MISO	GPIO25	SPI0_SCLK	SPI0_CE0_N	GND
Number	26	27	28	29	30
Name	SPI0_CE1_N	ID_SD	ID_SC	GPIO5	GND
Number	31	32	33	34	35
Name	GPIO6	GPIO12	GPIO13	GND	GPIO19
Number	36	37	38	39	40
Name	GPIO16	GPIO26	GPIO20	GND	GPIO21

Table 8.1: Pinout of the Raspberry Pi 3B.

Number	1	2	3	4	5
Name	SCL	SDA	VCC	A0	A1
Number	6	7	8	9	10
Name	A2	GND	SDA1	SCL1	SDA2
Number	11	12	13	14	15
Name	SCL2	SDA3	SCL3	SDA4	SCL4

Table 8.2: Pinout of the Multiplexer (TCA9546A).

Number	1	2	3	4
Name	VCC	SDA	SCL	GND

Table 8.3: Pinout of the SHT21 and BME280

Bibliography

- [1] Sensirion. *Datasheet SHT21 - Humidity and Temperature Sensor IC*, 5 2014. Version 4.
- [2] Bosch Sensortec. *BME280 - Combined humidity and pressure sensor*, 9 2018. Document revision: 1.6.
- [3] Wolfgang Demtröder. *Experimentalphysik 3 - Atome, Moleküle und Festkörper*. Springer-Verlag, Berlin Heidelberg New York, 5. Aufl. edition, 2016.
- [4] Elektronik Kurs - MOSFET-MOS-Feldeffekttransistor. <http://elektronik-kurs.net/elektronik/mosfet-mos-feldeffekttransistor/>.
- [5] Wencke Hansen. Ausarbeitung des Vortrags: Strahlenschäden und Strahlenhärte von Halbleiterdetektoren. https://web.physik.rwth-aachen.de/~hebbeker/lectures/sem0607/hansen_ausarbeitung.pdf, 2006/2007.
- [6] Saure (Wikipedia-author). Grundaufbau der Wheatstone-Brücke, umgezeichnet. <https://de.wikipedia.org/w/index.php?oldid=176207594>, 06.09.2019.
- [7] Biezl (Wikipedia-author). Circuit of a Brokaw bandgap reference. <https://de.wikipedia.org/w/index.php?oldid=185351689>, 21.09.2019.
- [8] en:user:Cburnett (Wikipedia-author). I²C-Bus mit einem Master und drei Slaves. <https://de.wikipedia.org/w/index.php?oldid=188177927#/media/Datei:I2C.svg>, 12.09.2019.
- [9] WEISS TECHNIK. *Betriebsanleitung - Temperatur- und Klimaprüfschränke Produktlinie WT3 und WK3*, 2 2014. Originalbetriebsanleitung.
- [10] Inductiveload (Wikipedia-author). Zerfallsschema von ⁶⁰Co. https://upload.wikimedia.org/wikipedia/commons/e/e0/Cobalt-60_Decay_Scheme.svg, 07.10.2013.

Selbstständigkeitserklärung

Hiermit versichere ich, die vorgelegte Thesis selbstständig und ohne unerlaubte fremde Hilfe und nur mit den Hilfen angefertigt zu haben, die ich in der Thesis angegeben habe. Alle Textstellen, die wörtlich oder sinngemäß aus veröffentlichten Schriften entnommen sind, und alle Angaben die auf mündlichen Auskünften beruhen, sind als solche kenntlich gemacht. Bei den von mir durchgeführten und in der Thesis erwähnten Untersuchungen habe ich die Grundsätze guter wissenschaftlicher Praxis, wie sie in der ‚Satzung der Justus-Liebig-Universität zur Sicherung guter wissenschaftlicher Praxis‘ niedergelegt sind, eingehalten. Gemäß § 25 Abs. 6 der Allgemeinen Bestimmungen für modularisierte Studiengänge dulde ich eine Überprüfung der Thesis mittels Anti-Plagiatssoftware.

Datum

Unterschrift